Università degli Studi di Palermo

Dipartimento di Scienze della Terra e del Mare (DiSTeM)

XIII ciclo dottorato di ricerca in geochimica

A TWO-COMPONENT MANTLE EXTENDING FROM MT ETNA TO HYBLEAN PLATEAU (EASTERN SICILY) AS INFERRED BY AN INTEGRATED APPROACH WITH NOBLE GASES, TRACE ELEMENTS AND ISOTOPE GEOCHEMISTRY

PhD thesis by :
Alessandra Correale

Coordinator:
Prof. F.Parello

Tutor:
Prof. S.Rotolo

Co-Tutor:
Dott. A.Paonita

Index

1. Introduction

2. Geological setting and magmatism

2.1 Geological context

Hyblean area

Etna

2.2 Magmatism

Hyblean area

Etna

2.3 *Samplings and analysis*

3. Petrography and mineral chemistry

3.1 Hyblean mantle xenoliths

Peridotites

Pyroxenites

Composite nodules

3.2 Etna

3.2.1 Lavas

La Montagnola center

Mt De Fiore center

Mt Spagnolo center

Mt Maletto center

3.2.2 Mafic tephra

FS

S11

3.2.3 Crystal-liquid equilibria

4. Whole rock geochemistry

4.1 Major elements composition

4.1.1 Hyblean area

4.1.2 Etna

4.2 Trace elements

4.2.1 Hyblean area

4.2.2 Etna

Melting and crystallization processes

4.3 Sr-Nd isotopes

4.3.1 Hyblean area

4.3.2 Etna

5.Noble gas from fluid inclusions

5.1 Hyblean area

5.1.1Chemical and isotopic composition of fluid inclusions

5.1.2Noble gases as geochemical tracers of mantle processes

Post-eruptive processes

Mantle processes

5.1.3 Evidences of mantle metasomatism by coupling noble gases and trace elements data

5.1.4 Inferences from the heterogeneity of the Hyblean mantle

5.2 Etna

5.2.1Chemical and isotopical composition of fluid inclusions

5.2.2Olivine-pyroxene disequilibria

5.2.3 He isotope variation in olivine phenocrysts

Post-eruptive processes

Pre-eruptive processes

5.2.4 Influence of a metasomatic component in the Etnean lava genesis highlighted from noble gases and trace elements geochemistry

6. Conclusions

Appendix

1. Introduction

The eastern sector of the Sicily was characterized by a mafic volcanism that occurred in two areas: the Mount Etna and the Hyblean Plateau, this latter located 50 km southward of Etna. While the onset of magmatism in the Hyblean region dates lower Trias and lasted until early Pleistocene (Patacca et al., 1979; Longaretti and Rocchi, 1990), Mt Etna volcanism is younger than 600 ka. The spatial and temporal vicinity of the two volcanic provinces led many authors to compare the two areas, in fact petrological, geochemical and isotopic investigations of the products erupted in the two volcanic provinces indicated that their sources have similar characteristics (Carter and Civetta, 1977; Carter et al, 1978; Cadoux et al., 2007; Trua et al., 1998).

Volcanism in Hyblean Plateau, fissure-related, was produced during three main phases : 1) Cretaceous alkali basalts (Amore et al. 1988), 2) Miocene alkali-basaltic lavas and tuff-breccia pipes (Bianchini et al., 1998) and 3) Plio-Pleistocene lava flows (Beccaluva et al., 1998); an even older (Triassic) volcanism is documented in deep wells, drilled within the carbonate cover. Erupted magmas cover a compositional range from basalts to basanites to less abundant nephelinites, with tholeitic to alkaline serial affinity (Beccaluva et al., 1998; Trua et al., 1998). In particular, alkaline lavas brought to the surface a large number of mantle-derived xenoliths, mainly spinel-facies peridotites and subordinate pyroxenites (Sapienza and Scribano, 2000 and references therein). These products were thoroughly investigated by many authors (Bianchini et al., 2010; Tonarini et al., 1996; Perinelli et al., 2008; Sapienza and Scribano, 2000; Sapienza et al., 2005) who highlighted the occurrence of metasomatic events affecting the local mantle.

Sr and Nd isotopic data of Hyblean peridotites ($^{87}Sr/^{86}Sr$ from 0.70288 to 0.70309; $^{143}Nd/^{144}Nd$ from 0.512850 to 0.512915) revealed the presence of a HIMU-like component, while pyroxenites have compositions slightly distinct ($^{87}Sr/^{86}Sr$ from 0.70297 to 0.70326; $^{143}Nd/^{144}Nd$ from 0.512906 to 0.512989), overlapping the alkaline lavas ($^{87}Sr/^{86}Sr$ from 0.70287 to 0.70328; $^{143}Nd/^{144}Nd$ from 0.51302 to 0.51291 Tonarini et al., 1996; Bianchini et al, 1999), implying that a pyroxenitic mantle strongly contributed to genesis of the Hyblean magmas (Bianchini et al, 2010). In addition, an HIMU mantle source was suggested by lead isotopic ratios ($^{206}Pb/^{204}Pb$ 19.25-20.00) for alkaline lavas (Bianchini et al., 1999).

Geochemical investigation of CO_2-rich fluid inclusions hosted in olivines and pyroxenes of mantle xenoliths (Sapienza et al., 2005), particularly microthermometric analyses and isochore calculation, showed entrapment pressures of fluid inclusions in the range 0.75–0.95 GPa, corresponding to a depth of 27–35 km (assuming a density of lithosphere of 2.85 g/cm^3), in the stability field of spinel peridotites. Furthermore, helium isotopic measurements of the fluid

inclusions hosted in peridotite minerals (both olivine and pyroxenes) showed values of 7.3 ± 0.3Ra (Sapienza et al., 2005), similar to the isotopic signature of Pantelleria Island (Martelli et al, 2008; Parello et al, 2000).

The eruptive history of Mt Etna, one among the most studied and monitored active volcanoes worldwide, is strictly connected with that Hyblean as its activity started just after the end of the Hyblean Pleistocenic magmatism.

The present edifice of Mt Etna volcano is the result of many eruptions of mantle-derived magmas which have undergone a different level of fractionation.

The Mount Etna activity began about 0.6 Ma BP with submarine eruptions of tholeitic mafic lavas which were followed by subaerial transitional lavas (200 ka BP) and later by alkaline basalts (200 ka to present-day activity), the each with well characterized and distinct trace elements and Sr-Nd-B isotope signatures (Armienti et al., 2004; Corsaro and Pompilio, 2004; Tanguy et al., 1997). In order to explain this geochemical variability, different processes were proposed: (1) mantle source metasomatism, responsabile for incompatible trace element enrichment, coupled to a depletion of some trace elements due to the continuous, though variable, melt production (Kamenetsky and Clocchiatti, 1996; Viccaro and Cristofolini, 2008), (2) Asthenospheric flows generated by the rollback of the subducting Ionian lithosphere (Doglioni et al., 2001; Gvirtzman and Nur, 1999) that provides a pathway for subduction-related fluids, responsabile for fluid mobile elements (FME) enrichment and variations in Sr-Nd-B isotopes (Schiano et al., 2001, Tonarini et al., 2001 and Armienti et al., 2004) in the mantle wedge beneath Mt. Etna and related mafic products (3) Contamination in the shallow-level crustal feeding system by country rock assimilation, magma-fluid interaction and magma mixing, resulting in magma geochemical signatures closer to those typical of the crust (Tonarini et al., 2001 and Armienti et al., 2004), (4) Mixing between different mantle sources producing intermediate geochemical characteristics between two different end-members (Armienti et al., 1988 and Armienti et al., 1989).

Marty et al. (1994), through the investigation of noble gases trapped in fluid inclusions from lavas encompassing Etna magma variability, suggested a single mantle source feeding Etnean magmas, given the almost constant values measured in the $^{3}He/^{4}He$ ratio (6.7±0.4 Ra). Similarly, the recent study of Nuccio et al., (2008) on fluid inclusions from some Etnean recent lavas (2001-2005 eruptions) confirmed the constancy of the helium isotopic marker, supporting the hypothesis of a homogeneous mantle source .

The aim of this study is to investigate and compare the characteristics of the Hyblean and Etnean mantle sources, in order to raise similarity in their geochemical signatures and/or processes that have acted in both the mantles. In doing this, we focused on the geochemical and petrological characteristics of selected primitive lavas and tephra of Etna (FS, Maletto, Spagnolo, De Fiore, Montagnola, S11 eruptions) and mantle-derived xenoliths from alkaline lavas of Hyblean region, performing a multi-isotopic study of noble gases (He, Ar, Ne), released from olivine/pyroxene-hosted fluid inclusions (FI) integrated by whole-rock geochemistry (major, and trace elements, Sr-Nd isotopic systematics). A careful petrographic study, including mineral chemistry, was preliminarly performed in order to select and characterize the most promising samples.

2. Geological setting and magmatism

2.1Geological context

Mt Etna and Hyblean Plateau (Sicily) are located in a zone characterized by a complex geodynamic setting resulting from the collision between the European and African plates (Barberi et al., 1974, Bousquet and Lanzafame 2004).

Lentini et al. (1996) distinguished in the above region three different domains:1) the foreland, formed by the Hyblean-Pelagian-Apulian block representing the undeformed area, 2) the Ionian basin floored by Mesozoic oceanic crust, 3) the sicilian-maghrebide chain, constituted by the corrugated collision zone between the European and African plates, which is extended from North Africa to Apennine-Maghrebian chain and including also the more advanced sector corresponding to the foredeep area (**Fig 2.1**).

The most important fault of this area have been named “Aeolian-Maltese fault system” by Lanzafame and Bousquet (1997). This system extends from the Malta escarpment, along the south-eastern coast of Sicily, to the eastern base of Etna (Timpe faults; Platania (1905)). Further north, the tectonic system continues less regularly across north-eastern Sicily, before reaching the Tyrrhenian Sea, where the faults control the volcanism of the Volcano-Lipari-Salina alignment (Lanzafame and Bousquet, 1997).

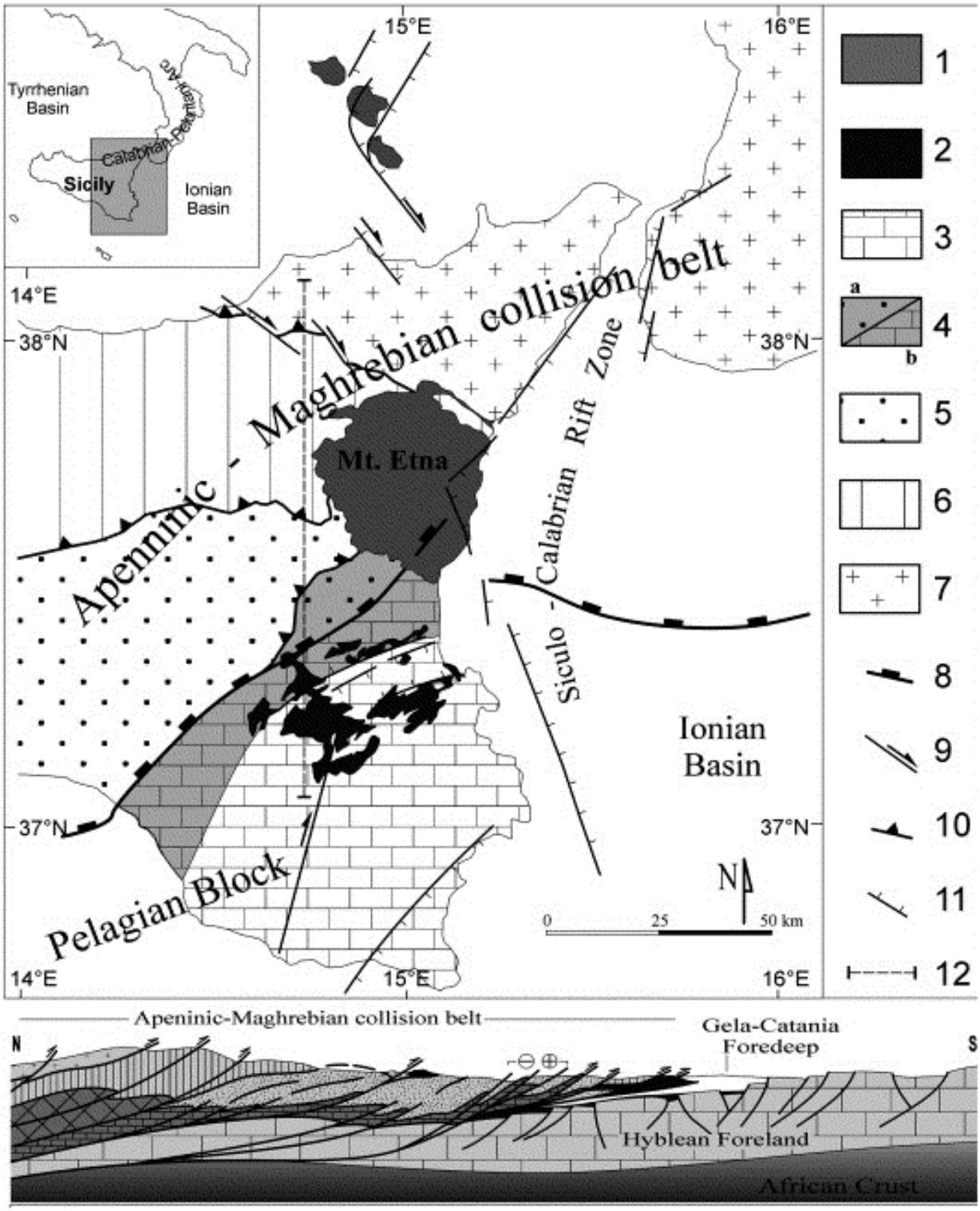

Fig. 2.1 Tectonic and geological sketch map of eastern Sicily. (1) Late Quaternary volcanics (Mt Etna and Aeolian Island); (2) Plio-Pleistocene volcanics (Hyblean Plateau); (3) Hyblean Plateau sequences; (4) Gela-Catania foredeep deposits: (a) Middle-Upper Pleistocene deposits on allochtonous units, (b) Quaternary deposits on the Hyblean sequences; (5) Neogene-Quaternary accretionary wedge units; (6) Maghrebian Thrust Belt units; (7) Calabrian arc units; (8) Front of allochtonous units; (9) Main strike-slipe faults; (10) Main thrust; (11) Main Quaternary normal faults; (12) trace of the N-S regional cross-section (from Catalano et al., 2004).

Hyblean area

The Hyblean sector is located in the south of the Sicily, that represents the undeformed northern section of the Pelagian Block (Burollet et al., 1978), in continuity with the African crust. Next to the Gela-Catania foredeep, the Hyblean Plateau is intersected by south-verging faults of the Appenine-Maghrebian chain, while is separated from the Ionian basin by the deeply rooted faults of the Hyblean-Maltese escarpment (Continisio et al., 1997 and references therein).

Although the Hyblean Plateau belongs to an undeformed lithospheric portion, it was influenced by the tectonism related to the building of the Sicilian-Maghrebian chain, generating an important fault system which facilitated the rising of mantle-derived magmas (Ben Avraham & Grasso, 1990). Magmatism was triggered by Mesozoic extensional tectonics which affected the whole, African continental margin (Finetti et al., 1996), while during Late Miocene-Pleistocene Hyblean volcanic activity was strictly connected with a NE-SW extensional tectonic accommodating the dextral (NNE-SSW striking) Scicli Line (Ben Avraham and Grasso, 1990). According to Continisio et al. (1997), the Hyblean volcanism stopped when the Scicli fault slowed down its motion, during late Pleistocene.

Mt Etna

Mount Etna volcano is located close to the eastern coast of Sicily, between the northern chain and the Hyblean foreland (Doglioni et al., 2001).

Structural and seismic data indicate that the regional deformation in the Etnean area is characterized by N-S compression (Cocina et al., 1997, 1998: Lanzafame et al., 1997) coexisting on the eastern side of the volcano with a roughly E-W extension or right-lateral transtension concentrated along the Malta fault system (Torelli et al., 1998; Azzaro, 1999).

Among the different hypothesis about the origin of Etnean volcanism we include:

(i) a hot spot origin (Tanguy et al., 1997; Clocchiatti et al., 1998), (ii) an asymmetric rifting process (Continisio et al., 1997) and (iii) the intersection of three major lithospheric faults beneath the Etnean area (Lanzafame et al., 1997; McGuire et al., 1997).

In order to explain the development of the volcanic Etnean center, Doglioni et al. (2001) proposed the existence of a lithospheric ‘window’ allowing magma ascent, due to differential rollback among the Ionian oceanic domain and the Sicilian continental one resulting in mantle decompression and partial melting along a vertical window in the slab. The idea of the differential rollback was already dealt with Gvirtzman and Nur (1999) but using a different approach, based

mainly on gravity reconstructions and not on the evolution and dip of the foreland monocline as in Doglioni et al. (2001).

2.2 Magmatism

Hyblean area

Discontinuous volcanic activity characterized the Hyblean Plateau since Triassic to Quaternary times, alternating subaerial to submarine activity.

The oldest volcanic rocks in the Hyblean Plateau are Triassic and Jurassic in age and have been recovered by drilling (Rocchi et al., 1995), while the oldest outcropping are Cretaceous alkali basalts and are located in the eastern part of the area (Capo Passero, Siracusa, and Augusta; Carveni et al., 1991a,b). After the Cretaceous activity, the volcanism ceased for about 50 Ma and then restarted during the Miocene with alkaline affinity lavas located in the central-northern area of the Hyblean Plateau and ranging from alkali basalts to basanites and ankaratrites (e.g., Bianchini et al., 1998).

The last eruptive episode, during Plio-Pleistocene, was characterized by the eruption of tholeiite and alkaline basalts and subordinate nephelinites (Beccaluva at al., 1998; Trua et al., 1998). Some diatreme-related deposits of Miocene age and some Quaternary basanitic and nephelinitic lavas sampled a part of lithospheric portion, carrying a large amount of ultramafic xenoliths to the surface (Sapienza and Scribano, 2000). Among these, the Miocene Valle Guffari diatreme is characterized by the greatest variety and quantity of deep xenoliths, and is also the area where most of the investigated samples in this study were collected (**Fig. 2.2**).

Etna

Latest eruptive events in the Hyblean Plateau were followed by the more recent magmatism of Mt Etna, the largest composite volcano in Europe which is located around 50 km north of the Hyblean Plateau and is characterized by a diameter of ~ 40 km and an height of 3340 m.

Lavas erupted over the volcano history belong to two magmatic series with different affinities: the oldest is subalkaline, the youngest is a mildly alkaline, mainly sodic. A progressive shift of the erupted rocks toward a potassic affinity has been observed in recent years (Schiano et al., 2001; Tonarini et al., 2001).

Branca et al., 2004 subdivided the evolution of Etnean volcanism into four phases:

- Tholeiitic (600-200 ka), characterized by the emission of tholeiitic basalts during submarine fissure-type eruption. The first volcanic products crop out near the village of Acicastello, on the

Ionian coast and consist of pillow lavas and hyaloclastitic breccias (Corsaro and Cristofolini, 1997; 2000). Tholeiites were also erupted as sub-aerial lava flows, in proximity of Simeto river (Chester and Duncan, 1979; Tanguy, 1978).

- Timpe (250-100 ka), interpreted as the results of a fissure activity fed by volcanic centers located near Acireale town, next to Timpe faults (Corsaro et al., 2002). After the end of fissural activity (~200 ka), the erupted products gradually evolved their composition to transitional and finally to Na-alkaline.

-The Valle del Bove centres (80-40 ka), characterized by a westward shifting of the Etnean feeding system and marked by the beginning of the construction of small central edifices whose remnants crop out in the Valle del Bove area. The products of this activity are essentially lava flows and volcaniclastic rocks.

-The Stratovolcano, characterized by construction of two main volcanic edifices: 1) the Ellittico and 2) the Mongibello. Both volcanic events displayed a wide range of eruptive styles from effusive and middly strombolian to plinian (Del Carlo et al., 2004) and ended their activity with caldera collapses: the *Ellittico caldera* (14 ka BP) followed the eruption of Biancavilla ignimbrites (De Rita et al, 1991) and the *Piano caldera* (122 BC) after a Plinian eruption (Coltelli et a., 1998). The gravitative sector collapse of Valle del Bove occurred instead around 6 ka BP (Calvari et al., 2004).

Mount Etna volcano produced both summit and flank eruptions principally controlled by magma ascent from a central conduit (Rittmann, 1965; Wadge, 1980; Chester et al., 1985; Allard et al., 2006). Summit eruptions take place at the open exit (summit craters) or subterminal branching of these central conduits and are much more common than flank eruptions (Branca and Del Carlo, 2004; Allard et al., 2006). However, the relatively high frequency of the latter is attested by the presence of 338 monogenic cones of varying age on the volcano slopes (Armienti et al., 2004), preferentially concentrated along the main volcano-tectonic structures of regional direction that have controlled the volcano build up. The flank eruptions are characterized by lava flows of low to medium volume and show petrographic features similar to lavas erupted from the summit craters (e.g. high porphyricity and abundance of plagioclase phenocrysts). A sub-group consists of rare flank eruptions that does not belong to the above criteria: being characterized by (i) moderately to highly explosive activity and also (ii) by the eruptions of a nearly aphyric plagioclase-free magma.

This magma suffered minor water degassing and was fed by deep dykes tapping the deep intrusions. Such eruption were termed “eccentric” (Rittmann, 1965) or “peripheral” (Acocella and Neri, 2003). Between the eccentric eruptions known in historical times we selected only some volcanic events, in particular:

-the 1974 (Mt De Fiore, Bottari et al., 1975; Tanguy and Kieffer, 1977; Corsaro et al., 2009)

-the 1763 (Montagnola, Sturiale 1970; Miraglia, 2002)

-after 14 ka (Mt Maletto and Mt Spagnolo, Armienti et al., 1988; Kamenetsky and Clocchiatti, 1996).

2.3 Samplings and analysis

As concern the Hyblean area, the studied samples consist of three peridotites (XIH-1, XIH-2 and XIH-3) four pyroxenites (XIP-4, XIP-28, XIP-14) and one composite peridotite-pyroxenite (XIC-26), found into some Miocene diatremes of the Hyblean area, in particular the Valle Guffari diatreme and Cozzo Molino pipe (**Fig 2.2**). The samples were selected on the basis of their size (~5 cm for the peridotites and ~10 cm for the pyroxenites) and freshness.

The studied samples on Mt Etna consist in basaltic lavas (Mt Spagnolo, Mt Maletto, Mt DeFiore, Montagnola) collected from subaphiric eccentric edifices, erupted during the last 15 ka, and Mg-rich tephra (the fall stratified basalt FS and the tepra layer S11), erupted 3-4 ka BP (**Fig 2.2**).

Major- and trace-element analyses were performed on (i) whole rock samples and (ii) on selected olivine and pyroxene grains. Separated of olivine and pyroxene phenocrysts were analysed for isotopic compositions of Sr, Nd and noble gases (He, Ne, Ar). All details on the analytical procedures are given in Appendix.

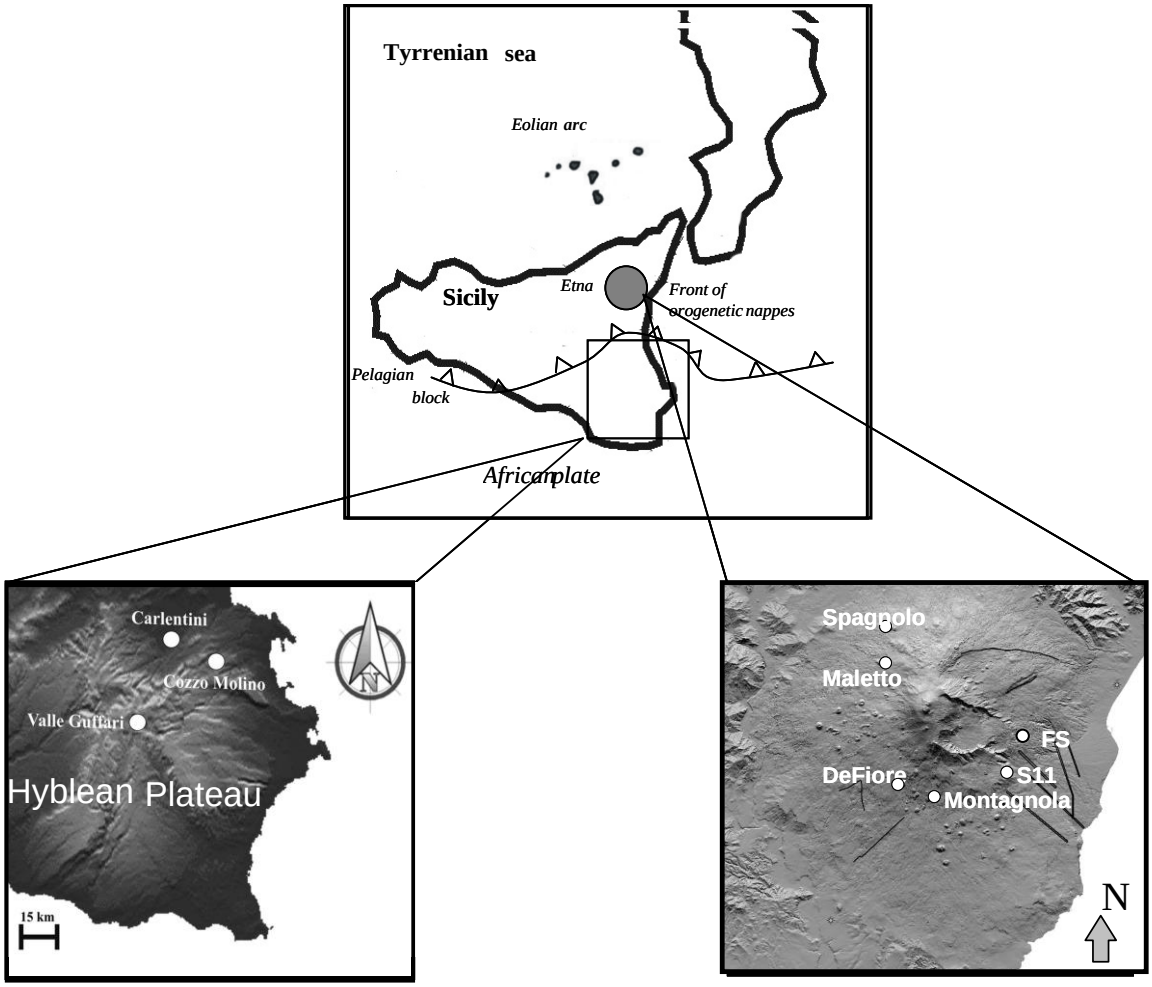

Fig 2.2 - Sketch map showing sampling sites of Hyblean and Etnean regions, respectively.

3 Petrography and mineral chemistry

3.1 Hyblean mantle xenoliths

Peridotites

On the basis of their mineralogical modal composition peridotites can be classified (see **Fig. 3.1** and **Table 1**) as: i) anhydrous spinel-facies harzburgites, XIH-1 (Ol 89%; Opx 8% vol, Cpx 1%) and XIH-2 (Ol 71%; Opx 28%, Cpx 1%) samples; ii) anhydrous spinel-facies lherzolite, XIH-3 (Ol 72%; Opx 16%, Cpx 12%) sample (see **Table 1**).

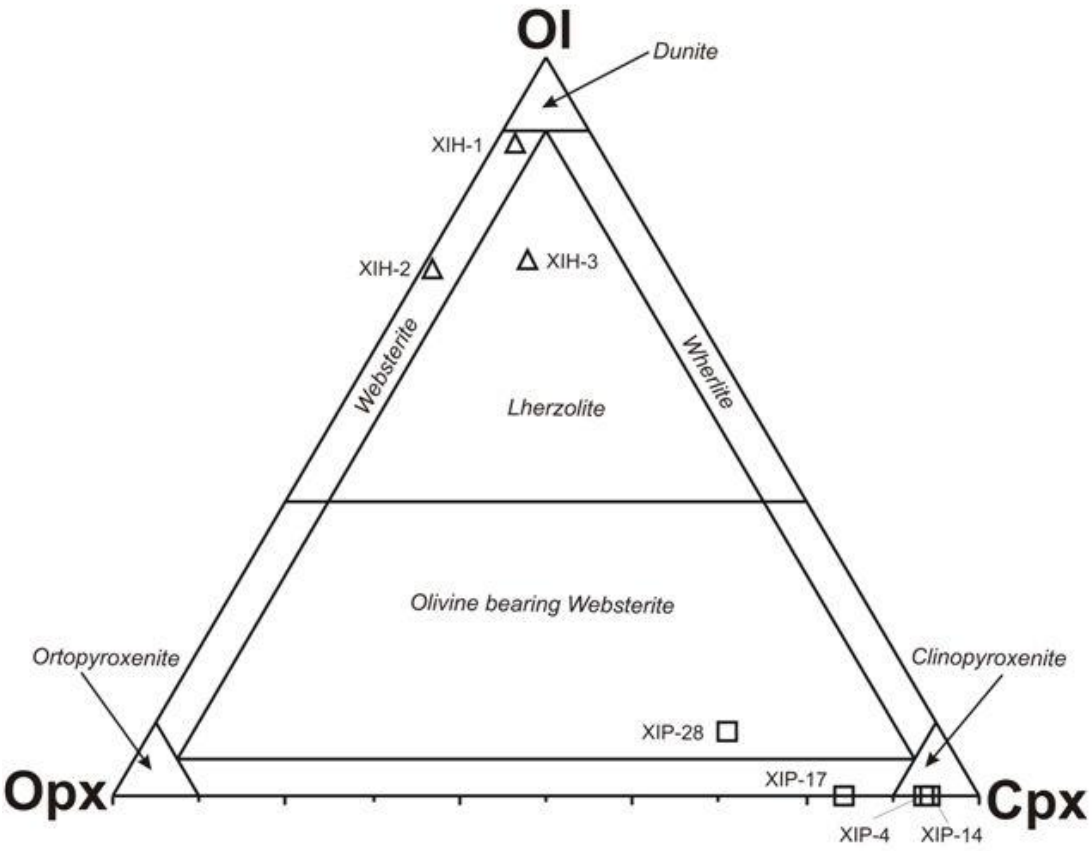

Fig 3.1 - Modal composition of investigated xenoliths.

The XIH-1 and XIH-3 samples are characterized by porphyroclastic texture, while the XIH-2 (**Fig 3.2a**) have a protogranular texture (see **Table 1**). Data on the major elements of the single minerals are reported in **Table 5**.

Olivine composition range between Fo_{89-90}; orthopyroxenes is Fs_{9-11}, Wo_{1-3}, and En_{86-90}, whereas the clinopyroxenes (Cr-diopsides) comprised Fs_{4-7}, Wo_{43-49}, and En_{46-50}.

The peridotitic samples were essentially fresh, but sometimes it was possible to observe a slight degree of serpentinization along the cracks within olivines or along grain boundaries.

Cr-Al spinel was also present both as interstitial grains and as vermiform intergrowths with the pyroxene.

Kink banding is ubiquitous in olivine crystals (**Fig 3.2b**). Some samples are characterized by localised increased abundance of pyroxenes, alternatively are clearly evident cm-sized websterite veins cross-cutting the peridotite sample.

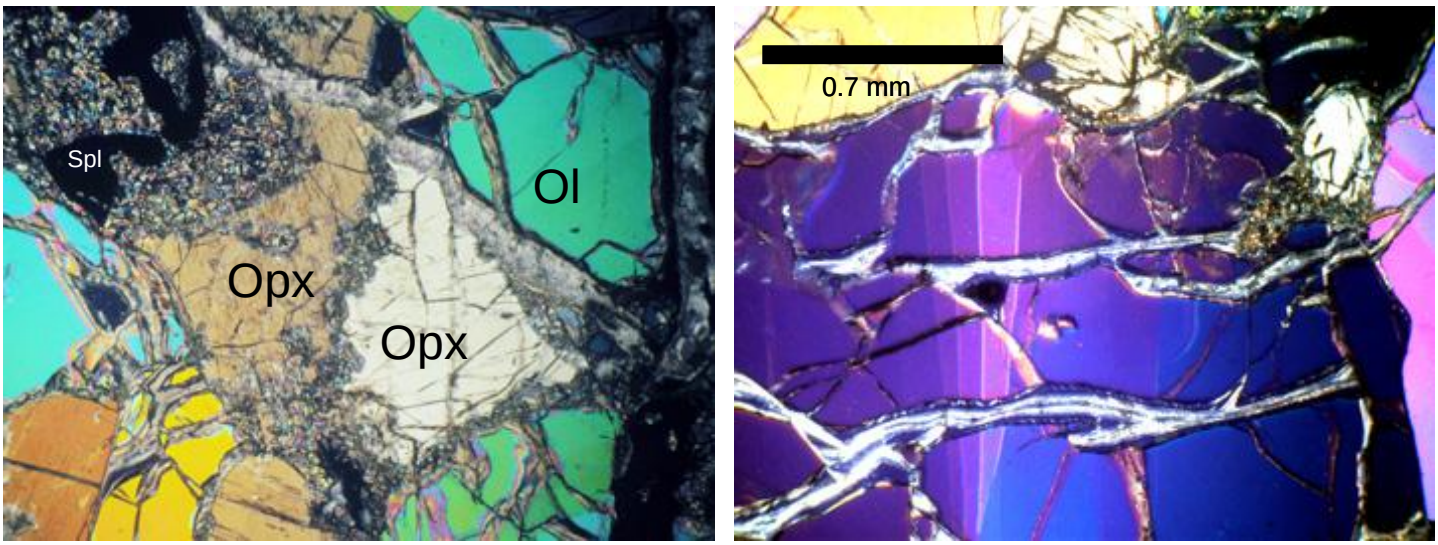

a)

Fig 3.2 – **a)** Protogranular texture in the peridotitic sample XIH-2. Orthopyroxene breakdown due to interaction with a silicate melt undersaturated in silica, **b)** Kink-banding in olivine furrowed by serpentine veins.

Pyroxenites

Four samples are pyroxenites on the basis of their olivine, orthopyroxene, and clinopyroxene percentages (**Fig 3.1**). In particular, samples XIP-4 and XIP-14 (Cpx 94%, Opx 6%) are clinopyroxenites while samples XIP-28 (Cpx 62%, Opx 23%, Ol 8%) and XIP-17 (Cpx 84%, Opx 16%) are websterite. The texture together with the modal composition of pyroxenitic nodules are resumed in **Table 1**.

Clinopyroxene from samples XIP-14, XIP-4, and XIP-17 is an Al-diopside (Al_2O_3 = 6.8–9.5 wt%; see **Table 5**) characterized by several exsolution lamellae of Ca-poor pyroxene and Al-spinel. On the other hand, clinopyroxene from XIP-28 and XIC-26 is a Cr-diopside (Cr = 0.75 and 1.14 wt%, respectively; **Table 5**). The orthopyroxene composition varied in the range $Fs_{9\text{-}20}$, $Wo_{1\text{-}3}$, and

En_{77-90}. Sample XIP-28 contains ~8 % Fo_{90} olivine. Most of the pyroxenite samples contained variable amounts of Al-Cr spinel, which was particularly abundant in sample XIP-4. However, it must be noted that the distribution of the spinel in these xenoliths is strongly irregular.

Due to their coarse grain size, the small dimension of recovered xenoliths, might not precisely be representative of the mineral proportions in the orginal mantle domain. In fact, the averaged modal compositions of pyroxenites from literature studies is: 85 vol % clinopyroxene, 5 vol % orthopyroxene, and Al-spinel 10 vol % (Punturo and Scribano, 1997). Noteworthy, spinel is sometimes rimmed by a garnet rim (keliphytized), as for instance in sample XIP-17 (Table 5).

Composite nodules

Also, the sample XIC-26 is a composite xenolith consisting of a harzburgitic peridotite frame cross-cut by two irregular 0.5-cm-wide clinopyroxenite veins.

Observations of both peridotites and pyroxenites under the optical microscope identified trails of pseudo-secondary FI in olivine and pyroxene crystals (**Fig 3.3**). FI are not uniformly distributed among the different mineral phases, in accordance with previous observations in peridotitic paragenesis by Sapienza et al. (2005). The clinopyroxenes are systematically richer in FI relative to coexisting olivines and orthopyroxenes, as observed frequently in mantle xenoliths from different areas (eg. Porcelli et al., 1986).

Fig 3.3 – Pseudo-secondary fluid inclusions trails in an orthopyroxene phenocryst from a pyroxenitic nodule
.

Sample	Location	Xenolith size (L x W, cm)	Texture	Modal composition (%vol)	Type
XIH-1	Cozzo Molino, near Melilli	~5 x 4	Porphyroclastic	Ol 75; Opx 8; Spl 2 ;Serp 5;Carb 10	Harzburgite
XIH-2	Head of Valle Guffari	~6 x 4	Protogranular	Ol 65; Opx 25; Spl 1; Cpx 1;Serp +Carb 8	Harzburgite
XIH-3	Cozzo Molino, near Melilli	~5 x 4	Porphyroclastic	Ol 50; Opx 11; Spl 3; Cpx 8; Serp 17; Carb 10	Lherzolite
XIC-26	Near Carlentini	~12 x 9	Porphyroclastic	Ol 28; Opx 5;Spl 3;Cpx 60; Serp + Carb 4	Composite Pyrox./Perid.
XIP-4	Head of Valle Guffari	~6 x 3	Coarse equant	Cpx 75; Opx 5; Spl 20	Clinoyroxenite
XIP-17	Valle Guffari	~15 x 10	Coarse equant	Cpx 70; Opx 13;Spl 8; Gar/Kel 5; Carb 4	Grt-bearing Al-Di Websterite
XIP-28	Valle Guffari	~8 x 5	Inequigranular	Cpx 62; Opx 23; Spl 2; Ol 8; Clay + Carb 5	Ol-bearing Cr-Di Websterite
XIP-14	Valle Guffari	~10 x 12	Inequigranular	Cpx 84; Opx 5;Grt 3; Spl 5; Clay + Carb 3	Grt-Opx-bearing Al-Di- Clinopyroxenite

Table 1- Schematic table summarizing the main characteristics of the studied Hyblean xenoliths. All species in wt%.

3.2 Etna

3.2.1 Lavas

La Montagnola Center

Basalts erupted from La Montagnola center are crystal-poor (crystallinity ≤ 10% vol) with phenocrysts of clinopyroxene in a minor amount with respect to olivine (**Fig 3.4**). The latter, in terms of composition, ranges from Fo_{74-77} (core) to Fo_{76-78} (rim) and is usually euhedral to subhedral (up to 2 mm in lenght). Clinopyroxene (diopside) is almost unzoned (core=Wo_{47-48} En_{33-36} Fs_{6}, rim=Wo_{46-47} $En_{29-35}Fs_{6-7}$), reaching up to 3 mm in length. Both olivine and clinopyroxene crystals enclose Fe-Ti oxides (Ti-magnetite).

The groundmass is microcrystalline, with microlites of plagioclase (An_{68-75} Ab_{25-29}), clinopyroxenes (Wo_{43-45} En_{30-37} Fs_{6-12}), olivine (Fo_{62-70}) and opaques, present in decreasing order of abundance respectively.

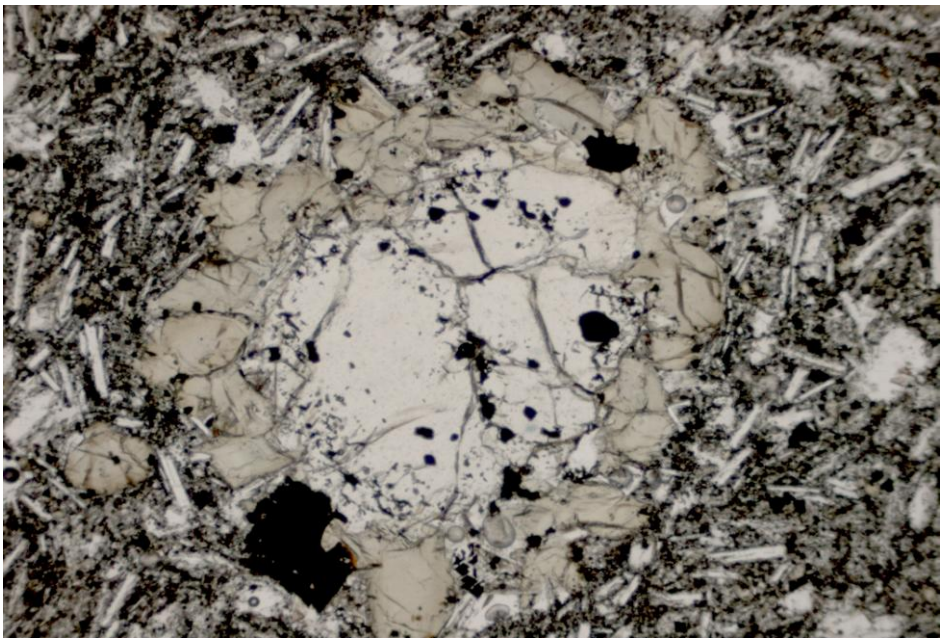

Fig 3.4 – Lava from the Montagnola center. Olivine phenocryst is jacketed by a clinopyroxene overgrowth corona . Parallel polars, magnification 40X.

Mt De Fiore center

Lavas erupted from De Fiore center are crystal-poor (crystallinity ≤ 10% vol) with phenocrysts of olivine up to 1 mm in length, directly zoned (core = Fo_{79-80} , rim= Fo_{75-79}). They are in major amount with respect to clinopyroxene which are up to 2 mm in length and slightly zoned (core=Wo_{46-47} En_{33-36} Fs_{5-7}, rim=Wo_{46} En_{35} Fs_{7-8}). Olivine is usually euhedral to subhedral and encloses Fe-Ti oxides (Ti-magnetite).

The groundmass is microcrystalline, with microlites of clinopyroxene (Wo_{47-48} En_{30-35} Fs_{1-10}) plagioclases (An_{66-74} Ab_{24-32}), olivine (Fo_{64-73}) and opaques in decreasing order of abundance respectively.

Mt Spagnolo

Mt Spagnolo is a composite eruptive center made of crystal-rich and crystal-poor basaltic lava flows. From these latter were selected our samples consisting of phenocrysts (< 15 vol %) of clinopyroxene (core Wo_{45-46} En_{38-42} Fs_{6-7}; rim Wo_{44-45} En_{36-38} Fs_{6-7}) much more abundant than olivines, which are usually euhedral to subhedral and up to 2 mm in lenght (core = Fo_{84-85}, rim= Fo_{85}).

At least three type of clinopyroxene phenocrysts occur: 1) a strongly zoned, with a thick rim and a lobated core; 2) slightly zoned with a thin rim; 3) characterized by a cribose structure.

Clinopyroxene microphenocrysts (core=Wo_{43-44} En_{38-43} Fs_{6-7} rim= Wo_{42-45} En_{34-41} Fs_{6-9}) are more abundant than olivines.

The groundmass is microcrystalline, with microlites of plagioclase (An_{59-65} Ab_{34-38}) much more abundant than clinopyroxene (Wo_{42-43} $En_{34-38}Fs_{8-10}$) and olivine (Fo_{61-62}) .

Mt Maletto

Basalts erupted form Mt Maletto center are characterized by crystallinity ≈15 vol. % with phenocrysts of olivine (**Fig 3.5**) usually euhedral to subhedral and up to 1 mm in length, directly zoned (core = Fo_{82-83}, rim= Fo_{73-83}) and in major amount if compared to clinopyroxene (diopide), that are up to 0.5 mm in lenght and slightly zoned (core=Wo_{45-49} En_{34-42} Fs_{5-7}, rim=Wo_{46-47} $En_{32-35}Fs_{5-7}$).

The groundmass is microcrystalline, with microlites of plagioclase (An_{64-73} Ab_{25-33}) major than clinopyroxene (Wo_{43} En_{33-35} Fs_{11-16}) and olivine (Fo_{66-67}).

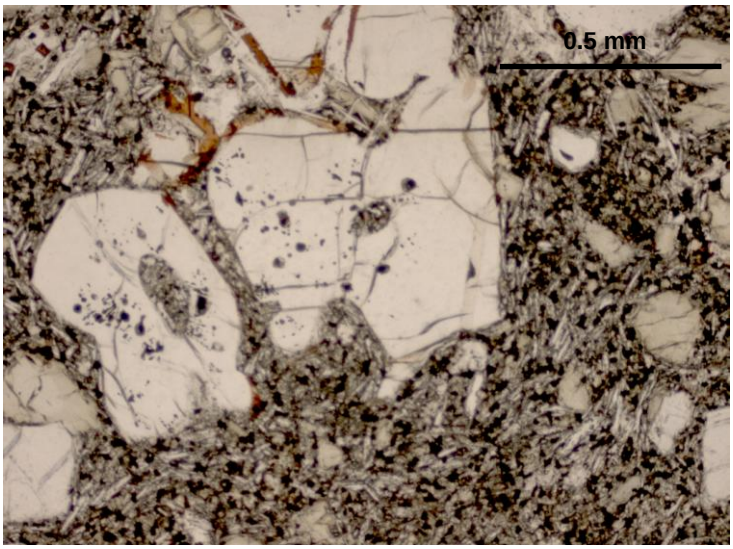

Fig 3.5– Maletto center. Microphoto showing a lobated olivine phenocryst. Parallel polars, magnification 40X.

3.2.2 Mafic tephra

FS tephra

The samples from FS eruption are highly vesicular (≈60%) and crystal-poor (crystallinity ≤ 5% vol) with phenocrysts of olivine (core = Fo_{89-91}, rim= Fo_{88-91}, see Fig 3.6) usually euhedral to subhedral, up to 2 mm in lenght and in higher amount than clinopyroxene (diopside) (core=Wo_{37} En_{46} Fs_3, rim=$Wo_{36}En_{46}Fs_6$), usually ≤ 0.5 mm in lenght .

There are two different types of groundmass: one black and microlite-poor and the other light-coloured and microlite-rich. The microlites of clinopyroxene (Wo_{41-47} En_{34-46} Fs_{3-10}), olivine (Fo_{85-89}) and plagioclase (An_{62-73} Ab_{25-37}) are present in decreasing order of abundance respectively (**Fig 3.6**).

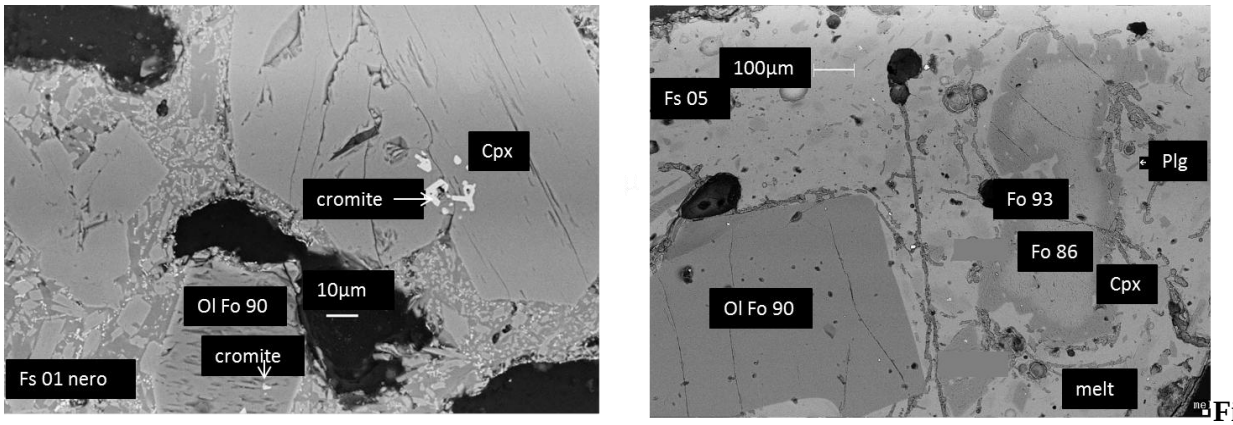

Fig 3.6– FS tephra. Back-scattered electron images showing olivine phenocrysts Fo (90-93%) hosting chromite and melt inclusions.

S11 tephra

The S11 tephra are highly vesicular (>50%) and crystal-poor (crystallinity ≤ 10% vol), with phenocrysts of olivine (**Fig 3.7 a**) up to 2 mm in length, directly and reversed zoned (core = Fo_{73-87}, rim= Fo_{77-85}) and in major quantity than plagioclase (**Fig 3.7 b**) (core=An_{51-56} Ab_{41-45}, rim= An_{53-66} Ab_{31-40}) and clinopyroxene (diopside) that are up to 3 mm in length (core=Wo_{45} En_{33} Fs_{9}, rim=$Wo_{46}En_{32}Fs_{6}$). Groundmass, slighly altered, occurs in two varieties: (i) a black and microlite-poor (plagioclase > olivine > clinopyroxenes), ii) the other light-coloured and microlite-rich (plagioclase > clinopyroxenes +olivine).

Olivine microlite is in the range Fo_{73-77} while clinopyroxene and plagioclase are Wo_{45-46} En_{31-32} Fs_{7-8} and An_{65-68} Ab_{31-34} respectively.

Modal and compositional characteristics of both Etnean lavas and tephra are summarized in **Tables 2** and **3**.

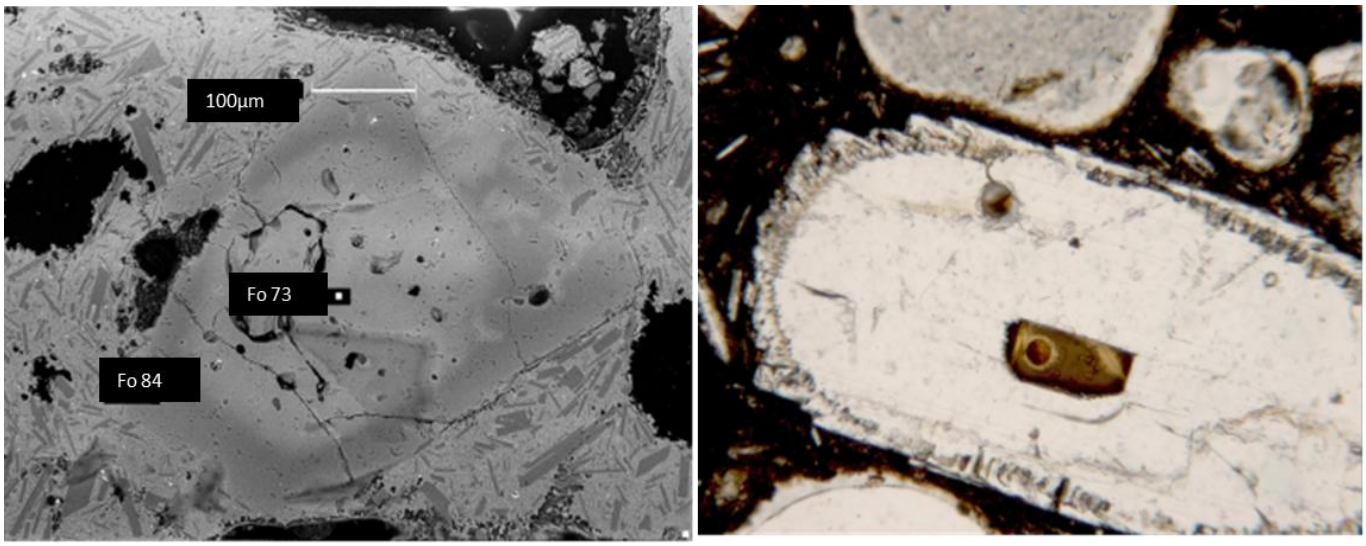

Fig 3.7– S11 tephra. **a)** Back-scattered electron image of a zoned olivine phenocryst, **b)** Microphoto showing a plagioclase phenocryst hosting a melt inclusion with shrinkage bubble and negative crystal shape due to overgrowth. Note also the resorption ovoidal shape and overgrowth rim. Parallel polars, magnification 100X.

Sample	P.I. (% vol)	Voids	Phenocryst abundances	Groundmass	Microlites
Montagnola	≤10%	<5%	oliv>cpx	microcrystalline	plg>cpx>ol
Mt DeFiore	≤10%	<5%	oliv>cpx	microcrystalline	cpx≥plg>ol
Mt Spagnolo	10-15%	<5%	cpx>>oliv	microcrystalline	plg>>cpx+ol
Mt.Maletto	≈15%	<5%	oliv≥cpx	microcrystalline	plg>>cpx+ol
FS	≤5%	60%	oliv>>cpx	glassy microlite-rich	cpx>ol>>plg
				glassy microlite-poor	cpx>ol>>plg
S11	≤10%	50%	oliv>cpx+plg	microlite-rich	plg>cpx+oliv
				microlite-poor	plg>oliv>cpx

Table 2- Schematic table summarizing the main petrographic features of investigated Etnean primitive products.

	Fo%					En%					Fs%					An%					usp%				
	Olivine					Clinopyroxene					Clinopyroxene					Plg					Spinel				
	phenocrysts		n.	microlite	n.	phenocrysts			microlite	n.	phenocrysts			microlite	n.	phenocrysts			microlite	n.	spl 1	n.	spl2	n.	
	core	rim				core	rim				core	rim				core	rim								
Montagnola	74-77	76-78	3	62-70	4	33-36	29-35	2	30-36	3	6	6-7	2	6-12	3				68-74	3	43	1		
Mt DeFiore	79-80	75-79	3	64-73	3	33-36	35	2	35-30	3	5-7	7-8	2	1-10	3				66-74	3	48	1	23	1
Mt Spagnolo	84-85	85	2	61-62	2	38-43	34-41	5	34-38	3	6-7	6-9	5	8-10	3				59-65	4	32	2		
Mt.Maletto	82-83	73-83	3	66-67	3	34-42	32-35	3	33-35	3	5-7	5-7	3	11-16	3				64-73	4	55	1	40	1
Fs	89-91	88-91	3	85-89	3	46	46	1	34-46	5	3	6	1	3-10	5				62-73	6				
S11	73-87	77-85	3	73-77	3	33	32	1	31-32	2	9	6	1	7-8	2	51-56	53-66	3	65-68	5	48	1		

n=number of analysed crystals

spl1= spl richer inTi and poorer in Al and Mg (TiO_2≥ 10%, MgO<6%, Al_2O_3<10%)

spl2= spl poorer inTi and richer in Al and Mg (TiO_2< 10%, MgO>6%, Al_2O_3>10%)

Table 3- Schematic table summarizing the main compositional features of olivines, clinopyroxenes and plagioclases from the investigated Etnean primitive products.

3.2.3 Crystal-liquid equilibria

Equilibrium among phenocrysts and the liquid (i.e. the whole rock composition) from all the the above rock samples has been calculated assuming all the FeO as FeO_{tot}.

K_D^{Fe-Mg} is considered to represent equilibrium between olivines and a basaltic melt if in the range 0.30 +/- 0.03 (FeO, Roeder & Emslie, 1970) or 0.26 +/- 0.04 (with FeO calculated as FeOtot, Di Carlo et al., 2006) and between cpx-liquid pairs if in the range 0.31 +/- 0.05 (Di Carlo et al., 2006).

The $K_D^{Fe-Mg}{}_{oliv-liq}$ range as follows (**Table 4**):

-0.21-0.35 (mean= 0.27+/- 0.04) and 0.40-0.60 for phenocrysts and microlites from De Fiore Unit respectively;

- 0.26-0.39 (mean= 0.33+/- 0.05) and 0.47-0.66 for phenocrysts and microlite from Montagnola Unit respectively;

-0.12-0.60 (mean= 0.25+/- 0.13) and 0.60-0.69 for phenocrysts and microlites from Maletto Unit respectively;

- 0.18-0.62 (mean = 0.30+/-0.13) and 0.89-0.92 for phenocrysts and microlites from Spagnolo Unit respectively;

-0.21-0.37 (mean value= 0.31+/-0.05) and 0.41-0.50 for phenocrysts and microlites from FS Unit respectively.

$K_D^{Fe-Mg}{}_{cpx-liq}$ are:

- 0.29-0.68 and 0.66-0.77 for phenocrysts and microlites from Maletto respectively;

- 0.25-0.45 and 0.44-0.53 for phenocrysts and microlites from Spagnolo;

-0.25-0.38 and 0.38-0.78 for phenocrysts and microlites from FS;

-0.34-0.40 and 0.40-0.57 for phenocrysts and microlites from DeFiore;

-0.32-0.60 and 0.39-0.57 for phenocrysts and microlites from Montagnola.

Both Kd for the olivine/pyroxene-liquid respectively are outside the range of equilibrium, with the phenocrysts generally being closer to equilibrium values than microlites.

.

Sample	$Kd_{oliv\text{-}melt}$	mean	std dev +/-	$Kd_{cpx\text{-}melt}$	mean	std dev +/-
De Fiore	0.21-0.35	0.27	0.04	0.34-0.40	0.36	0.03
Montagnola	0.26-0.39	0.33	0.05	0.32-0.60	0.42	0.12
Maletto	0.12-0.60	0.25	0.13	0.29-0.68	0.43	0.13
Spagnolo	0.18-0.62	0.30	0.13	0.25-0.45	0.34	0.08
FS	0.21-0.37	0.31	0.05	0.25-0.38	0.60	0.49

Table 4- $Kd^{Fe\text{-}Mg}_{oliv\text{-}melt}$ for Etnean study products (calculated assuming all the FeO as FeO_{tot}).

4 Whole rock geochemistry

4.1 Major elements composition

4.1.1 Hyblean area

Whole rock major elements analyses for of the eight study xenoliths are presented in **Table 5**. The data from the composite xenolith XIC-26 represent the average composition of this sample. The results of our analyses are in the range of literature data for Hyblean nodules, confirming a general homogeneity in the major chemistry of the investigated xenoliths (Atzori et al., 1999; Bianchini et al., 2010; Nimis, 1998; Perinelli et al., 2008;Tonarini et al., 1996).

In **figure 4.1** is shown the abundance of major elements respect to aluminium, this latter was chosen as representative and discriminating element given its great variability (Al_2O_3 = 0.77 - 23.81 %).

Peridotite (both lherzolites and harzburgites) major element distribution is characterized by high MgO, relatively low Al_2O_3, CaO, TiO_2 conform to their elevated abundances of modal Mg-olivine.

Alumina content in pyroxenitic samples shows generally a positive correlation with TiO_2 and CaO and negative correlation with MgO. The generally elevated CaO contents, shown by all the investigated pyroxenitic xenoliths, reflect the common dominance of calcic over Ca-poor pyroxenes. Sample XIP-4 has an exceptionally low silica content (SiO_2 = 25.4 wt%) and high alumina content (Al_2O_3 = 23.8 wt%) that could be explained by the high modal amount of Al-Cr spinel.

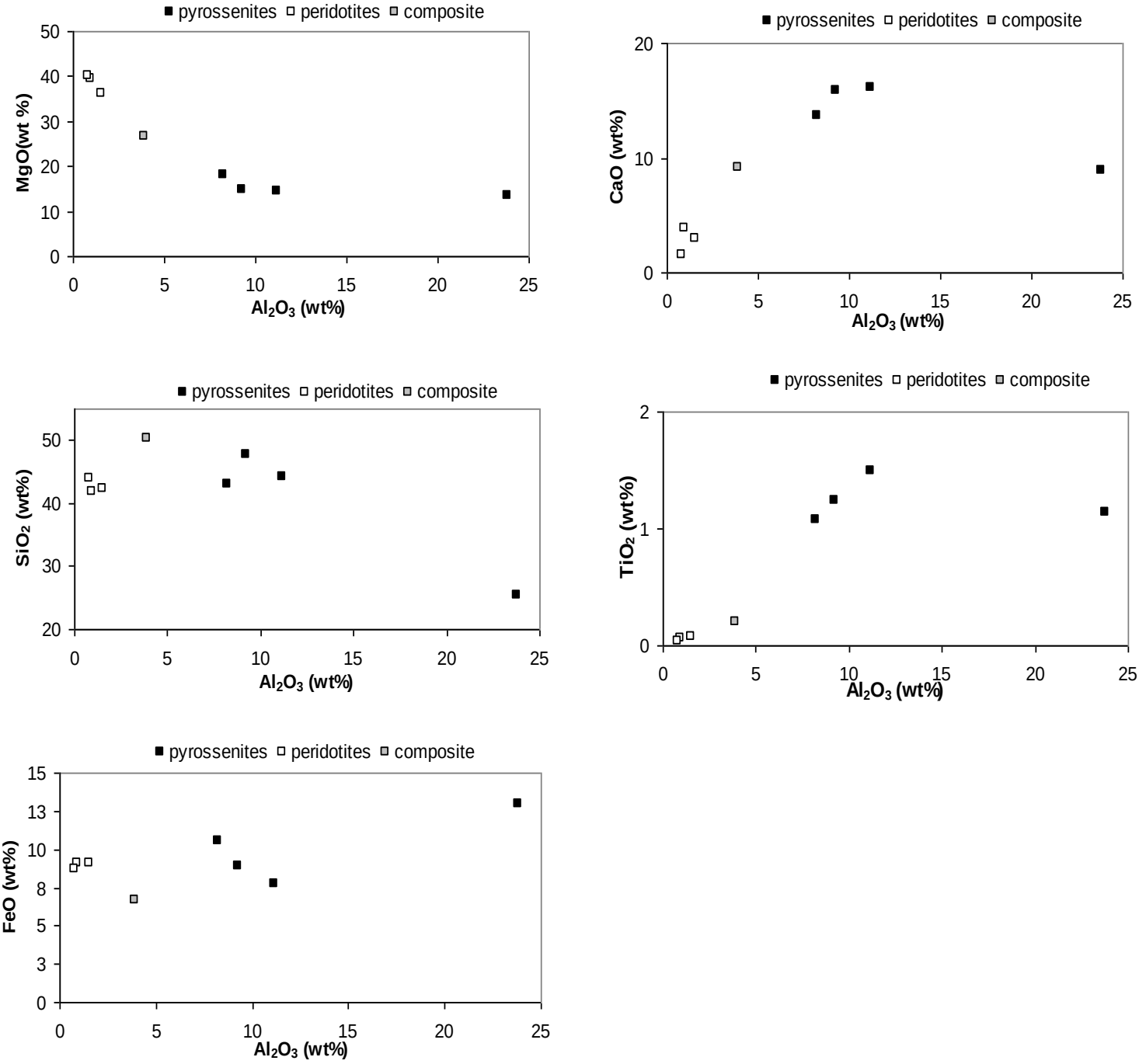

Fig 4.1 – Whole-rock major element variations of Hyblean xenoliths as a function of Al_2O_3

	sample	wt%	SiO_2	TiO_2	Al_2O_3	FeO	MnO	MgO	CaO	Na_2O	K_2O	P_2O_5	Cr_2O_3
PERIDOTITES	XIH-1	WR	41,93	0,06	0,93	9,11	0,11	39,46	3,85	0,04	0,02	0,06	0,05
		Opx	56,66	0,11	2,76	6,25	0,15	32,67	0,57	0,49	b.d.l	b.d.l	0,47
		Cpx	53,27	0,27	3,66	2,84	b.d.l	0,00	22,68	1,11	b.d.l	b.d.l	0,85
	XIH-2	WR	44,07	0,03	0,77	8,74	0,11	40,29	1,59	0,03	0,02	0,03	0,13
	XIH-3	WR	42,36	0,08	1,53	9,11	0,11	36,15	2,99	0,12	0,02	0,16	0,35
		Ol	41,00	b.d.l	0,03	10,39	0,26	47,58	0,12	0,70	0,01	b.d.l	0,08
		Opx	55,24	0,16	4,05	6,72	0,08	31,00	1,39	0,64	0,03	b.d.l	0,70
		Cpx	52,23	0,32	5,50	3,88	0,15	16,09	19,59	1,35	b.d.l	b.d.l	1,05
PYROXENITES	XIP-4	WR	25,46	1,13	23,81	12,92	0,11	13,55	8,89	0,73	0,02	0,03	0,08
		Cpx	48,33	1,73	9,53	7,43	0,14	12,63	18,59	1,74	b.d.l	b.d.l	0,05
	XIP-17	WR	44,18	1,50	11,17	7,75	0,11	14,41	16,07	0,76	0,09	0,11	0,02
		Opx	54,93	0,11	4,14	8,06	0,20	32,01	0,72	0,00	n.a	n.a	n.a.
		Cpx	50,03	1,19	6,25	3,95	0,11	15,32	21,29	0,79	n.a	n.a	n.a.
		Spl	n.a	0,45	65,14	11,72	0,09	22,14	n.a	n.a	n.a	n.a	0,52
		Grn	40,36	0,11	22,62	16,16	0,46	14,12	6,75	0,03	n.a	n.a	n.a.
	XIP-14	WR	47,63	1,24	9,24	8,88	0,15	14,77	15,87	1,20	0,07	0,08	0,03
		Opx	51,23	0,54	6,89	12,53	0,19	27,20	1,35	0,18	n.a	n.a	n.a.
		Cpx	48,48	1,59	9,52	4,26	0,10	13,54	17,81	1,41	n.a	n.a	n.a.
		Spl	0,09	0,56	59,78	20,35	0,11	18,02	n.a	n.a	n.a	n.a	0,11
		Grn	41,60	0,38	23,22	13,50	0,35	17,32	5,57	n.a	n.a	n.a	n.a.
	XIP-28	WR	42,95	1,07	8,21	10,57	0,13	17,95	13,66	0,80	b.d.l.	0,07	0,11
		Oliv	40,81	n.a	n.a	9,80	0,15	49,80	n.a	n.a	n.a	n.a	n.a.
		Opx	55,42	0,19	3,62	6,26	0,15	32,94	0,47	n.a	n.a	n.a	0,35
		Cpx	52,80	0,31	2,75	2,25	0,08	16,70	22,98	0,51	n.a	n.a	0,65
		Spl	n.a	0,11	55,80	11,61	0,09	20,80	n.a	n.a	n.a	n.a	11,40
	XIC-26	WR	50,40	0,20	3,90	6,70	0,10	26,70	9,20	0,30	b.d.l.	0,10	0,68
		Oliv	40,61	n.a	n.a	9,48	0,15	50,16	n.a	n.a	n.a	n.a	n.a.
		Opx	55,80	0,12	2,85	6,65	0,16	34,30	0,35	0,01	n.a	n.a	0,59
		Cpx	51,64	0,67	5,59	3,44	0,13	16,86	19,16	1,36	n.a	n.a	1,14
		Spl	n.a	0,42	33,10	19,60	0,20	16,15	n.a	n.a	n.a	n.a	29,15

Table 5- Major element composition of whole rock and mineral phases of studied peridotites and pyroxenites xenoliths

4.1.2 Etna

Data on major elements for the investigated Etnean lavas are presented in **Table 6**.

We also reported for comparison the data related to other Etnean primitive eccentric eruption occurred during 2001 and 2002-2003 (Clocchiatti et al., 2004; Corsaro et al., 2006; Viccaro et al., 2006). Throughout these last two eruptions, magma with different petrography and composition were erupted. We focused our attemption only on those products showing slightly more primitive features.

On the Total Alkali Silica Diagram Maletto (average values from this work, Tanguy et al., 1997 and Armienti et al., 1988), S11(this work) and FS (values from Coltelli et al., 2005) plot in the field of basalts. Conversely, samples from 2001 (average values from Viccaro et al., 2008; Viccaro et al., 2006, Corsaro et al., 2006; Clocchiatti et al., 2004), 2002-2003 (average values from Viccaro et al., 2008, Clocchiatti et al., 2004) and De Fiore (Corsaro et al., 2009; Armienti et al., 2004; Tanguy et al., 1997; Armienti et al., 1988) plot in that of trakybasalt. Finally Montagnola (average from Corsaro et al., 2009; Viccaro et al., 2008; Armienti et al., 1988,) and Spagnolo (average from this work, Tanguy et al., 1997 and Armienti et al., 1988) fall in an intermediate zone between the two fields (**Fig 4.2)**.

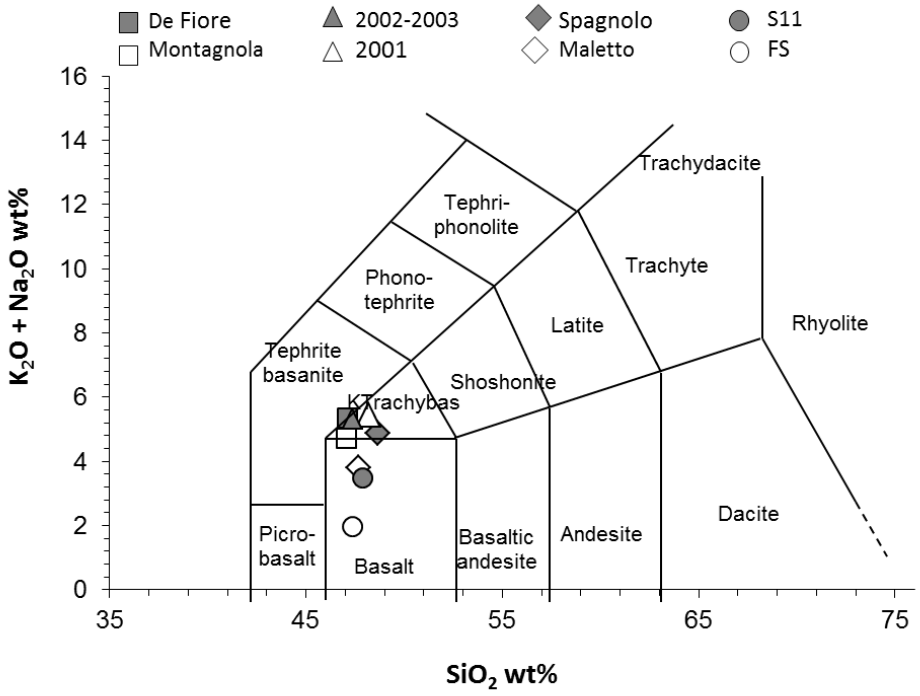

Fig 4.2 Total alkali-silica diagram (Le Bas et al., 1986) for Etnean products from primitive and eccentric eruptions.

Variation diagrams with MgO (**Fig. 4.3**) as differentiation index show that the analyzed lava follow simple trends of increasing Na_2O, K_2O, Al_2O_3, TiO_2 with decreasing Mg while CaO and MgO show direct correlation.

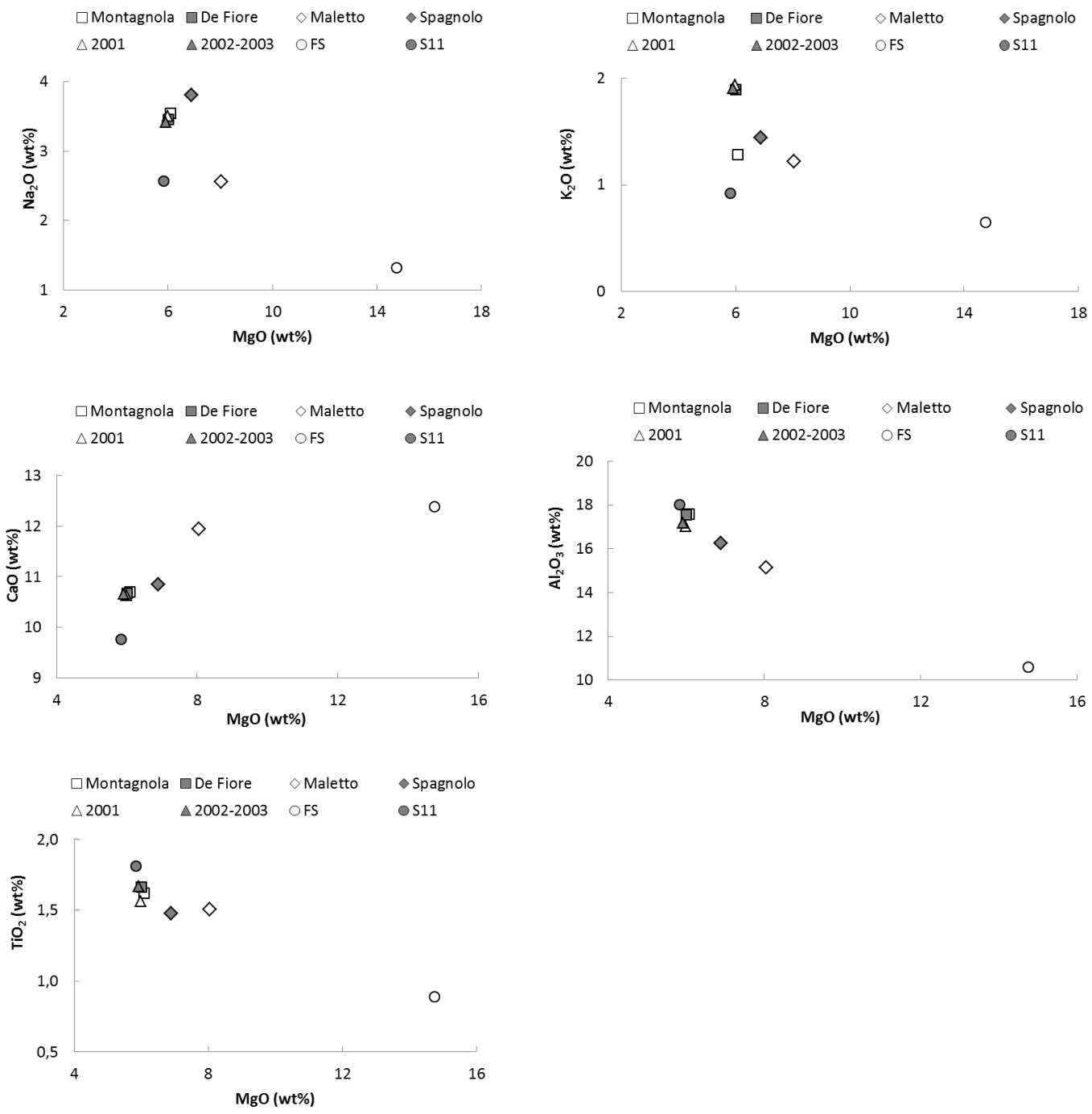

Fig 4.3 Whole rock major element variations for the investigated Etnean products as a function of MgO. Reported average values as in fig 4.2 (see text).

FS exhibits the most primitive characteristics among all the study sample, having the highest MgO (~15 wt %) and CaO (~12%) and the lowest Na_2O (~1.3%), K_2O (~0.6%) and Al_2O_3 (~10%) contents, whereas the most recent products (DeFiore, 2001, 2002-2003, Montagnola) are notably more evolved having the lowest MgO (~6%) and CaO (~11%) and the highest Na_2O (~3.5%) and Al_2O_2 (~17%) contents. A particular behaviour is assumed by S11 sample, being characterized by the least primitive CaO and Al_2O_3 values, near to those of recent lavas but by Na_2O and K_2O intermediate between those of the most evolved and primitive products.

As a whole, an inverse and a direct correlation exists between K_2O vs CaO/Al_2O_3 and $MgO/MgO+FeO_{tot}$ vs CaO/Al_2O_3 ratios respectively where the three investigated parameters are strictly connected with differentiation processes (**Fig 4.4 a-b**). In particular, $MgO/MgO+FeO_{tot}$ ratio decreases in the melt after mafic phases crystallization, and CaO/Al_2O_3 decreases during the pyroxene crystallization but increases after plagioclase.

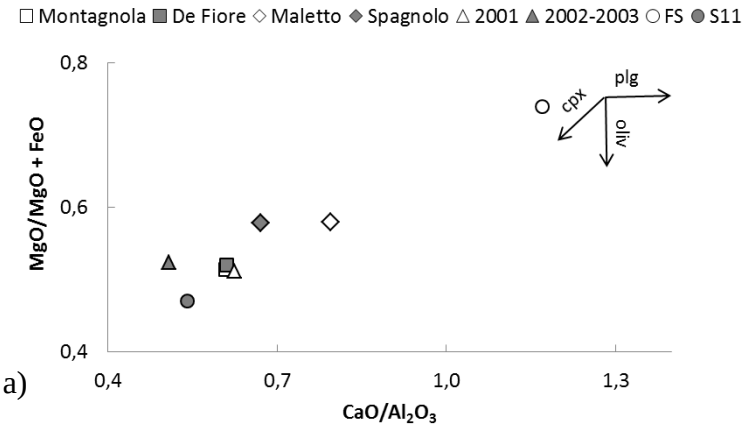

a)

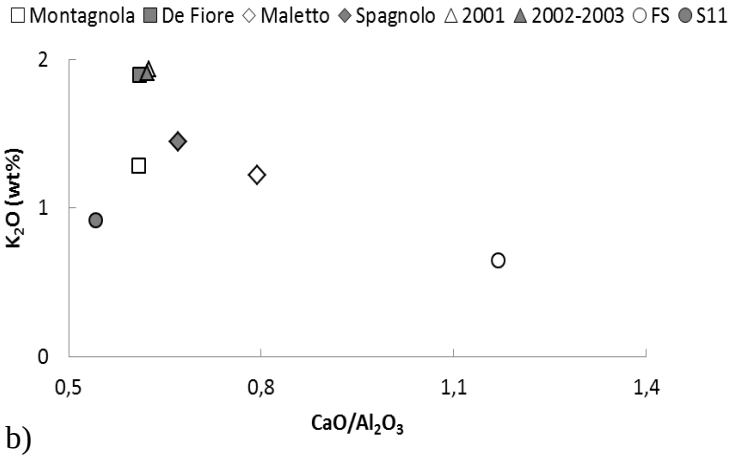

b)

Fig 4.4 Variation diagram of : a) CaO/Al_2O_3 vs $MgO/MgO + FeO_{tot}$ ratio; b) CaO/Al_2O_3 vs K_2O. The direction of variation of liquid composition during crystallization of different solid phases is represented by the black arrows in a). We reported the average value from different authors as in fig 4.2 (see text).

The different evolution between the investigated lavas is again highlighted by the positive trend in the CaO/Al_2O_3 vs Fo% content plot (**Fig 4.5**).

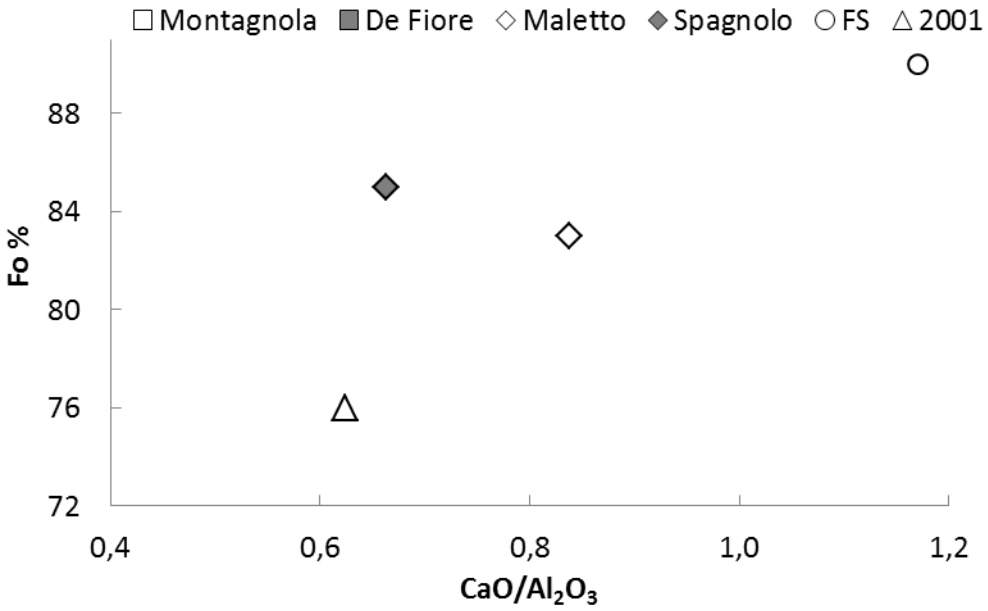

Fig 4.5 Variation diagram of CaO/Al_2O_3 vs Fo% in primitive Etnean products.

	Montagnola			De Fiore				Maletto			Spagnolo		
	(1)	(2)	(3)	(4)	(5)	(1)	(3)	(6)	(4)	(1)	(4)	(6)	(1)
n.	3	2	3				8	1		2	2	1	4
SiO_2(wt%)	47,08	46,97	47,26	47,14	47,79	47,56	46,75	47,47	48,30	47,33	49,37	48,46	48,68
TiO_2	1,62	1,63	1,62	1,68	1,61	1,62	1,75	1,51	1,47	1,53	1,41	1,52	1,51
Al_2O_3	18,13	17,98	16,68	16,46	18,53	18,49	16,72	14,71	14,10	16,59	16,24	15,15	17,43
Fe_2O_3	3,78	7,13	1,77	3,67	3,35	4,22	1,76	1,83	3,89	3,47	4,26	1,59	3,38
FeO	6,59	4,03	8,81	7,20	6,31	5,82	8,81	9,13	7,23	6,95	5,06	7,97	5,72
Fe_2O_3t	11,03	11,55	11,46	11,59	10,29	10,62	11,46	11,87	11,84	11,12	9,82	10,36	9,67
MnO	0,18	0,18	0,18	0,19	0,17	0,17	0,19	0,19	0,15	0,19	0,16	0,17	0,16
MgO	6,56	5,39	6,30	6,07	6,15	5,86	5,93	8,05	8,24	7,84	6,39	7,68	6,60
CaO	10,51	10,66	10,93	10,97	10,30	10,45	10,96	12,33	12,06	11,45	10,71	11,58	10,27
Na_2O	3,45	3,79	3,39	3,58	3,40	3,34	3,53	2,52	2,69	2,47	3,99	3,75	3,68
K_2O	1,23	1,28	1,34	1,99	1,83	1,87	1,89	1,18	1,24	1,25	1,54	1,39	1,40
P_2O_5	0,38	0,42	0,50	0,52	0,41	0,41	0,55	0,44	0,33	0,38	0,58	0,65	0,57
LOI	0,48	0,58	0,91	0,35	0,15	0,23	0,77	1,20	0,57	0,57	0,33	0,85	0,61
Total	99,99	100,00	99,68	99,82	100,00	100,04	99,60	100,56	100,27	100,00	100,02	100,74	100,00

(1) From Armienti et al.,1988
(2) From Viccaro et al., 2008
(3) From Corsaro et al., 2009
(4) From Tanguy et al., 1997
(5) From Armienti et al.,2004
(6) From this work
(7) From Clocchiatti et al., 2004
(8) From Viccaro et al., 2006
(9) From Corsaro et al., 2006
(10) From Coltelli et al., 2005
n= number of analyses

Table 6- Whole rock composition for the studied Etnean products.

	2001				2002-2003		FS	S11
	(7)	(8)	(2)	(9)	(7)	(2)	(10)	(6)
n.	3	5	4	7	4	2	6	1
$SiO_{2(wt\%)}$	47,62	49,79	47,94	47,34	47,05	47,72	46,69	47,89
TiO_2	1,63	1,50	1,50	1,63	1,68	1,66	0,89	1,81
Al_2O_3	16,84	16,86	17,80	16,64	16,49	17,91	10,59	18,02
Fe_2O_3			4,00	1,75		4,76		
FeO			5,89	8,77		5,69		
Fe_2O_3t	11,43	9,73	10,48	11,41	11,61	11,02	10,30	13,05
MnO	0,17	0,17	0,18	0,17	0,17	0,18	0,17	0,15
MgO	6,04	5,82	5,80	6,28	6,43	5,40	14,75	5,83
CaO	10,77	10,11	10,69	10,96	11,13	10,20	12,39	9,76
Na_2O	3,40	3,53	3,74	3,35	3,23	3,61	1,32	2,57
K_2O	1,90	1,99	1,98	1,87	1,93	1,89	0,65	0,92
P_2O_5	0,50	0,49	0,49	0,47	0,49	0,45	0,23	
LOI	-0,18		0,41	0,75	-0,23	0,54	1,90	
Total	100,12	100,00	100,40	99,98	99,98	100,00	99,87	100,00

(1) From Armienti et al.,1988
(2) From Viccaro et al., 2008
(3) From Corsaro et al., 2009
(4) From Tanguy et al., 1997
(5) From Armienti et al.,2004
(6) From this work
(7) From Clocchiatti et al., 2004
(8) From Viccaro et al., 2006
(9) From Corsaro et al., 2006
(10) From Coltelli et al., 2005

n= number of analyses

Table 6- Whole rock composition for the studied Etnean products. We also reported for comparation the analyses about two other Etnean eccentric eruptions (2001 and 2002-2003).

4.2 Trace elements

4.2.1 Hyblean area

Trace-element data for the peridotite and pyroxenite samples are listed in **Table 7**. **Fig 4.6** shows the chondrite-normalized REE distribution for both whole rock and clinopyroxenes of peridotites. The REE patterns are similar in **Fig 4.6 a** and **b**, although the clinopyroxenes show clear REE enrichments relative to whole rocks, which are due to the high affinity of REE for the pyroxene structure (Eggins et al., 1998).

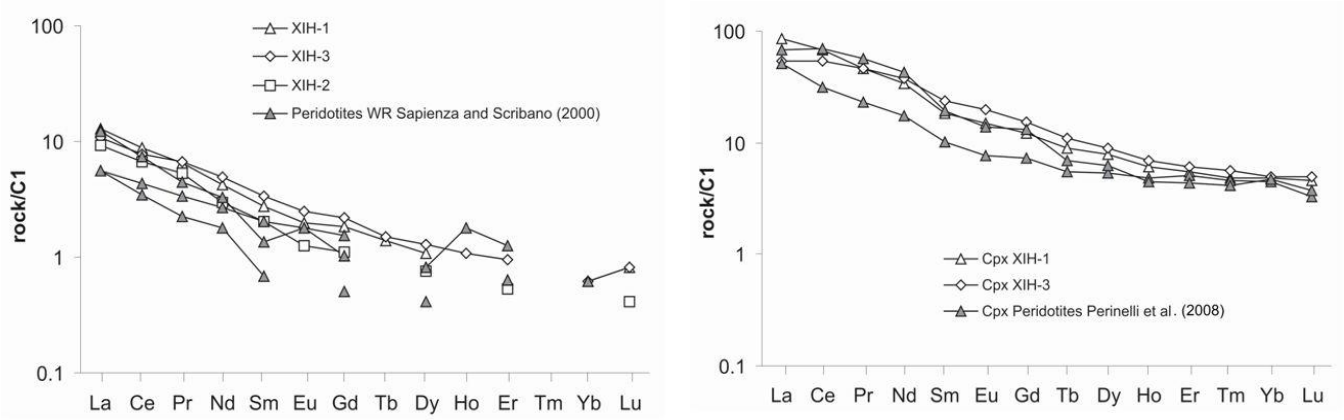

a) b)

Fig 4.6- C1-normalized REE patterns of a) whole rock (this work and Sapienza & Scribano, 2000) and b) cpx (this work and Perinelli et al., 2008) from peridotites. Normalization to C1 is after Anders and Grevesse (1989).

The plots show consistent patterns of both whole rocks and clinopyroxenes among different samples, suggesting a homogeneous source composition. Compared to chondrite, all samples showed evident LREE enrichment ($La_n/Yb_n \approx 20$) while HREE are similar or slightly depleted with respect to chondrite (**Fig 4.6a**). In previously published data of Hyblean peridotites, such LREE enrichments, were attributed to a pervasive or, more likely, cryptic metasomatism of a moderately depleted mantle (Perinelli et al., 2008; Sapienza and Scribano, 2000; Sapienza et al., 2005). The residual nature of the peridotites is also confirmed by the depletion observed in HFS elements relative to primordial mantle abundances (**Fig 4.7**), similarly to the one reported by Sapienza and Scribano (2000).

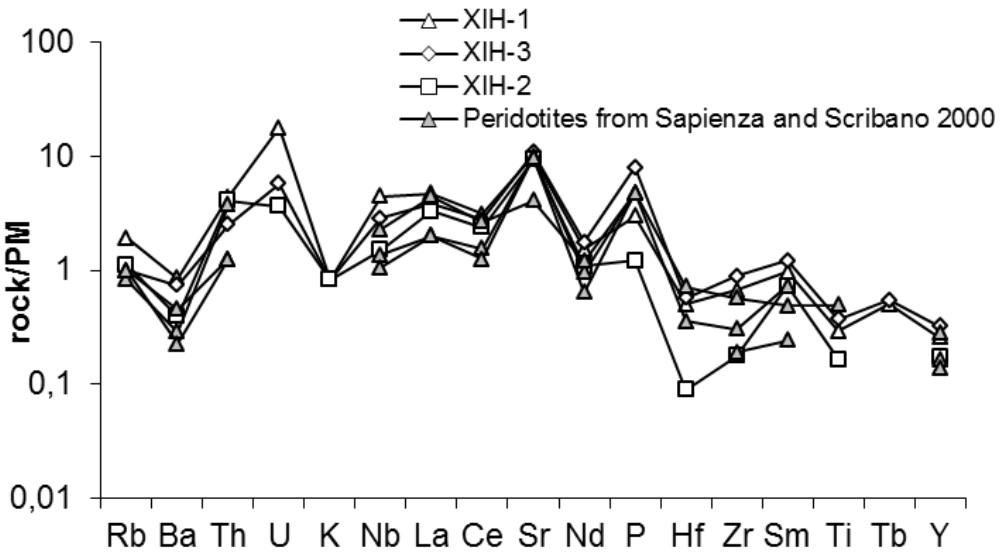

Fig 4.7 – Spider diagram of whole rock (this work and Sapienza & Scribano, 2000) from peridotites. Normalization to PM is after Sun & Mcdonough (1989).

The chondrite-normalized REE distribution of pyroxenites is displayed in **Fig 4.8**, both for whole rocks and clinopyroxenes.

The pyroxenitic samples show a REE upward-convex pattern, characterized by a less-pronounced enrichment of LREE and of HREE compared to MREE. Among the analyzed samples, only the composite peridotite-pyroxenite sample, XIC-26, shows a different pattern, due probably to its mineral abundance transitional between peridotites and pyroxenites. The enrichment of LREE in pyroxenites relatively to chondrites varied among the studied samples (La_n/Yb_n = 2.4–11.3), opposite to what was observed in peridotites (**Fig 4.8 a b**). We recall that pyroxenites are recovered as veins in peridotite matrix, thus they would represent the crystallization product of deep magmatic liquids that intruded the peridotites at different levels of the lithospheric mantle (Sapienza and Scribano, 2000). In this framework, the differences in LREE enrichments among pyroxenite samples could reflect varying degrees of metasomatism, depending on the extent to which the metasomatizing melts interacted with the surrounding peridotite.

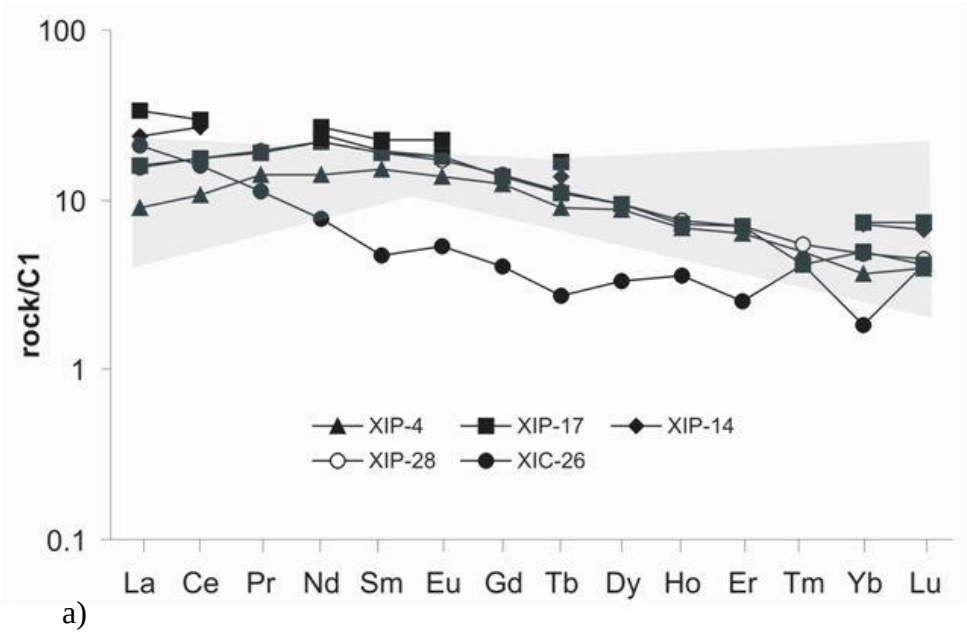

a)

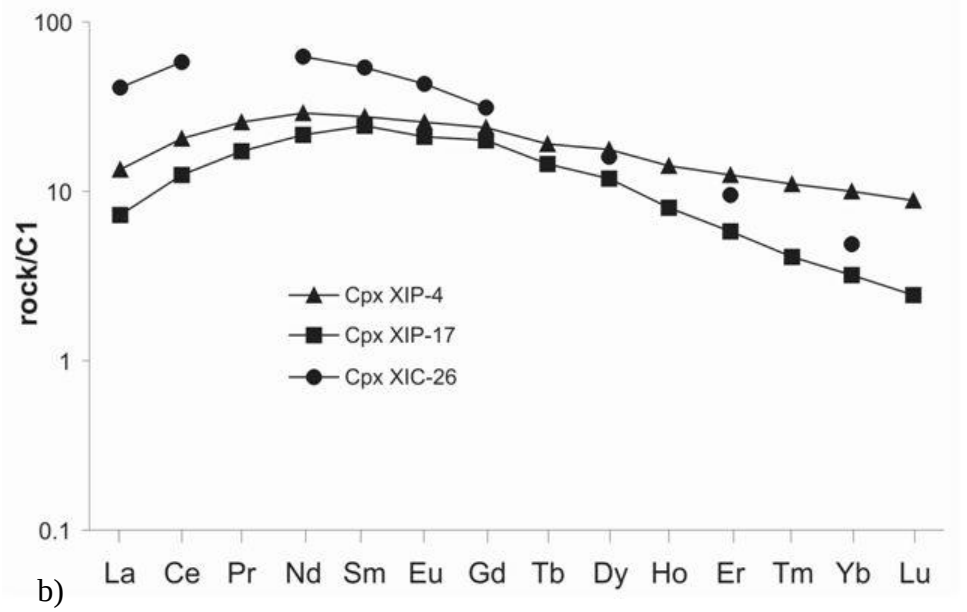

b)

Fig 4.8- C1-normalized REE patterns of **a)** whole rock pyroxenites from this work (symbols) and Sapienza & Scribano (2000) (shaded area) and **b)** cpx (this work) from pyroxenites. Normalization to C1 as in figure 4.6.

Fig 4.9 shows the relationships between Zr vs. the Zr/Nb ratios of the bulk rock samples. The complete data set, including our data and literature ones (Sapienza and Scribano, 2000), define two clearly distinguishable compositional fields for pyroxenites and peridotites: pyroxenites are characterized by Zr concentrations of 26–40 ppm and a Zr/Nb ratio of ~20, while peridotites exhibit a much lower Zr content of ~8 ppm and a Zr/Nb ratio of ~4. The lower Zr concentration of peridotites is related to their more refractory nature. A particularly notable behaviour was displayed by the XIC-26 pyroxenite sample, which showed Zr and Zr/Nb values of 3.5 ppm and 5.3, respectively, which are much more similar to those of peridotites. **Fig 4.9** also shows the compositions of erupted lavas having HIMU and DM signatures. The high incompatibility of Zr results in an obvious enrichment of Zr concentration in these latter with respect to peridotite xenoliths; nevertheless, being both Zr and Nb highly incompatible elements, the Zr/Nb ratio is almost unaffected by FC and partial melting processes, with the consequence that the Zr/Nb ratio in mantle-derived melts mirrors their abundance in the mantle source. On these bases we use the Zr/Nb ratio to compare lavas and xenoliths.

Pyroxenites exhibit the Zr/Nb ratio that is typical of DM, peridotites clearly plot in the HIMU range (**Fig 4.9**).

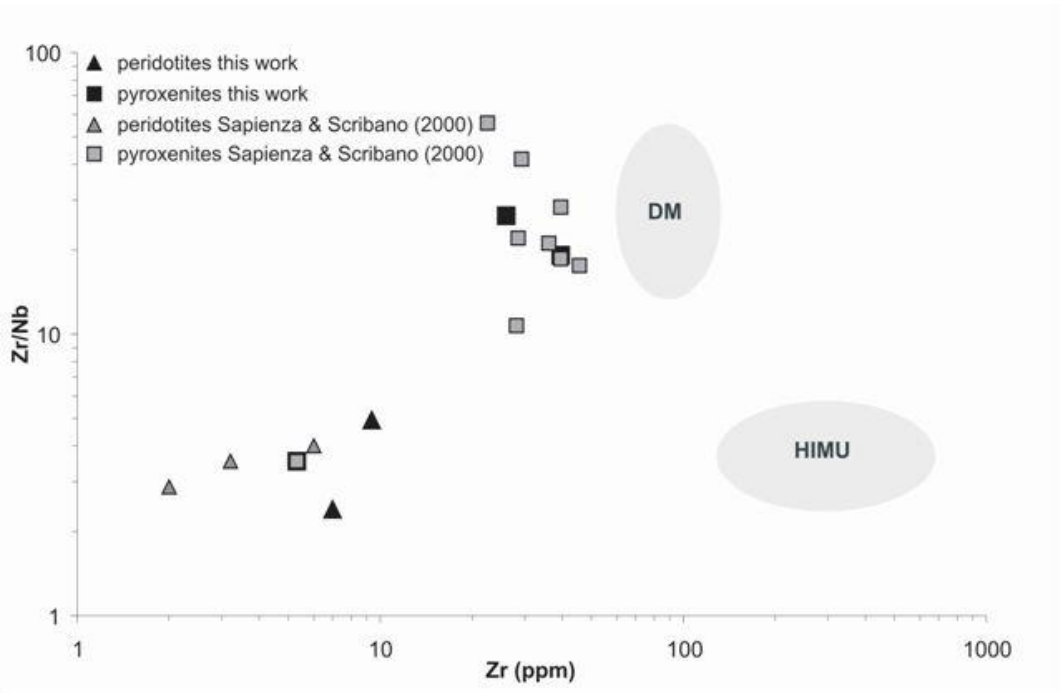

Fig 4.9 - Zr/Nb vs Zr diagram for whole rock from peridotites and pyroxenites. The Zr/Nb ratio of peridotites approach slightly those of a HIMU-type source whereas those of pyroxenites are more similar to a DM source. Reference fields: DM source from Sun & Mcdonough (1989), Hofmann (1988), Arevalo et al. (2010) while HIMU source from Chauvel et al. (1992).

	PERIDOTITES								PYROXENITES								
sample	XIH-1	XIH-1	XIH-1	XIH-2	XIH-3	XIH-3	XIH-3	XIH-3	XIP-4	XIP-4	XIP-17	XIP-17	XIP-14	XIP-28	XIP-28	XIC-26	XIC-26
	WR	OPX	CPX	WR	WR	OLIV	OPX	CPX	WR	CPX	WR	CPX	WR	WR	CPX	WR	CPX
ppm																	
Ba	5.65	0.24	0.43	2.60	4.90	0.02	0.07	0.59	17.90	0.44	181	1.51	26.00	3.20	1.38	2.60	0.40
Sc	6.35	18.41	94.86	8.45	8.75	3.20	21.22	58.45	23.90	55.70	42.20	57.87	37.70	n.a.	55.00	n.a.	n.a.
Sr	202	0.57	276	186	216	0.02	2.27	250	60.10	94.61	648	57.69	161	150	51.53	142	242
V	35.50	93.96	272.99	35.25	60.50	5.75	117	239	386	332	401	380	284	231	219	152	277
Ce	5.25	0.21	41.22	4.01	4.69	0.01	0.36	32.61	6.42	12.46	18.00	7.47	16.00	10.60	6.23	9.60	35.00
Co	129	58.91	25.57	121.50	123.50	134.45	71.49	29.58	100	41.82	n.a.	31.04	n.a.	n.a.	30.24	n.a.	n.a.
Cs	0.80	0.07	0.01	0.15	0.10	0.01	0.01	0.07	0.20	0.02	n.a.	0.02	n.a.	n.a.	0.01	n.a.	b.d.l.
Dy	0.26	0.12	1.91	0.19	0.31	0.01	0.19	2.17	2.13	4.27	n.a.	2.85	n.a.	2.28	0.97	0.80	3.90
Er	0.10	0.12	0.88	0.09	0.15	0.01	0.13	0.96	1.00	2.00	n.a.	0.93	n.a.	1.11	0.57	0.40	1.50
Eu	0.11	0.08	0.83	0.07	0.14	b.d.l.	0.05	1.11	0.77	1.43	1.26	1.18	1.00	0.96	0.22	0.30	2.40
Gd	0.36	0.08	2.40	0.22	0.43	b.d.l.	0.14	3.01	2.46	4.63	n.a.	3.90	n.a.	2.75	0.83	0.80	6.10
Hf	0.14	0.07	0.61	0.03	0.16	b.d.l.	0.09	0.80	0.90	2.28	1.90	2.11	1.30	1.54	0.16	0.20	n.a.
Ho	b.d.l.	0.05	0.34	b.d.l.	0.06	b.d.l.	0.04	0.38	0.38	0.78	n.a.	0.44	n.a.	0.42	0.20	0.20	n.a.
La	3.05	0.11	20.11	2.15	2.50	b.d.l.	0.09	12.71	2.10	3.18	7.80	1.71	5.60	3.67	6.07	4.90	9.70
Lu	0.02	0.05	0.11	0.01	0.02	b.d.l.	0.03	0.12	0.10	0.22	0.18	0.06	0.16	0.11	0.08	0.10	n.a.
Nb	2.95	0.18	1.97	1.00	1.90	0.01	0.24	1.85	1.00	0.59	n.a.	0.10	n.a.	2.06	5.03	1.50	1.90
Nd	1.90	0.14	15.35	1.35	2.20	0.01	0.34	17.14	6.30	13.00	12.00	9.79	11.00	10.00	1.98	3.50	28.00
Pb	0.70	0.09	0.93	b.d.l.	0.70	0.01	0.02	0.20	b.d.l.	0.06	n.a.	0.25	n.a.	n.a.	0.09	n.a.	n.a.
Pr	0.58	0.07	4.17	0.47	0.60	0.00	0.06	4.08	1.26	2.26	n.a.	1.52	n.a.	1.74	0.48	1.00	n.a.
Rb	1.15	0.09	0.04	0.68	0.60	0.02	0.03	0.15	0.45	0.08	9.00	0.12	9.00	0.99	0.02	0.40	1.40
Sm	0.40	0.10	2.73	0.30	0.50	0.01	0.11	3.52	2.20	4.11	3.29	3.58	2.87	2.79	0.60	0.70	7.90
Ta	0.07	0.04	0.22	0.60	0.05	b.d.l.	0.02	0.30	0.05	0.12	0.10	0.02	n.a.	0.18	0.27	b.d.l.	n.a.
Tb	0.05	n.a.	n.a.	b.d.l.	0.06	n.a.	n.a.	n.a.	0.33	n.a.	0.60	n.a.	0.50	0.41	n.a.	0.10	n.a.
Th	0.35	0.07	1.61	0.33	0.20		0.01	0.36	0.10	0.06	0.50	0.02	0.30	0.23	1.18	0.50	0.20
Tm	b.d.l.	0.05	0.12	b.d.l.	b.d.l.	b.d.l.	0.02	0.14	0.12	0.26	n.a.	0.10	n.a.	0.13	0.08	0.10	n.a.
U	0.36	0.08	0.34	0.07	0.12	0.01	0.01	0.16	0.08	0.02	0.20	0.01	0.10	0.08	0.33	b.d.l.	0.20
Y	1.10	0.57	8.88	0.75	1.40	0.05	1.10	9.51	8.00	18.93	18.00	10.14	17.00	11.70	5.13	3.90	18.40
Yb	0.10	0.18	0.79	b.d.l.	0.10	0.02	0.18	0.81	0.60	1.63	1.20	0.52	1.16	0.78	0.55	0.30	0.80
Zr	7.00	0.94	17.07	1.88	9.40	0.11	5.50	46.29	26.20	48.73	45.00	41.45	40.00	39.30	5.77	5.30	72.00
$^{87}Sr/^{86}Sr$	n.a.	n.a.	0.702956±5	n.a.	n.a.	n.a.	n.a.	0.703031±6	n.a.	0.703143±5	n.a.	0.702859±7	n.a.	n.a.	0.703063±7	n.a.	0.703022±5
$^{143}Nd/^{144}Nd$	n.a.	n.a.	0.512917±6	n.a.	n.a.	n.a.	n.a.	0.512919±7	n.a.	0.512947±8	n.a.	0.512994±6	n.a.	n.a.	0.512916±13	n.a.	0.512909±6

Table 7- Trace elements abundance of whole rock and mineral phases and Sr-Nd isotopic compositions of handpicked clinopyroxenes from studied Hyblean xenoliths.

4.2.2 Etna

Trace-element data for the studied Etnean samples are listed in **Table 8** and portrayed in **Fig 4.10** where are shown chondrite-normalized REE distributions for whole rock samples of the primitive Etnean lavas. Compared to chondrite, all the samples show a similar pattern characterized by a general stronger LREE enrichment with respect to HREE (La_n/Yb_n =11-26).

The differences in LREE concentrations among the samples, increasing from FS picritic basalt to Mt Spagnolo basalt, probably could be ascribed to a different degree of melting of a common mantle source, being the first melt more enriched in incompatible elements respect to the following ones. In **Fig 4.10** the REE patterns for the analyzed Hyblean peridotites and pyroxenites (shaded areas) are also reported.

Although the Etnean lavas result as a whole REE-richer with respect to chondrite than the Hyblean peridotites, as expected by a melt with respect to its mantle source, they show a similar REE pattern.

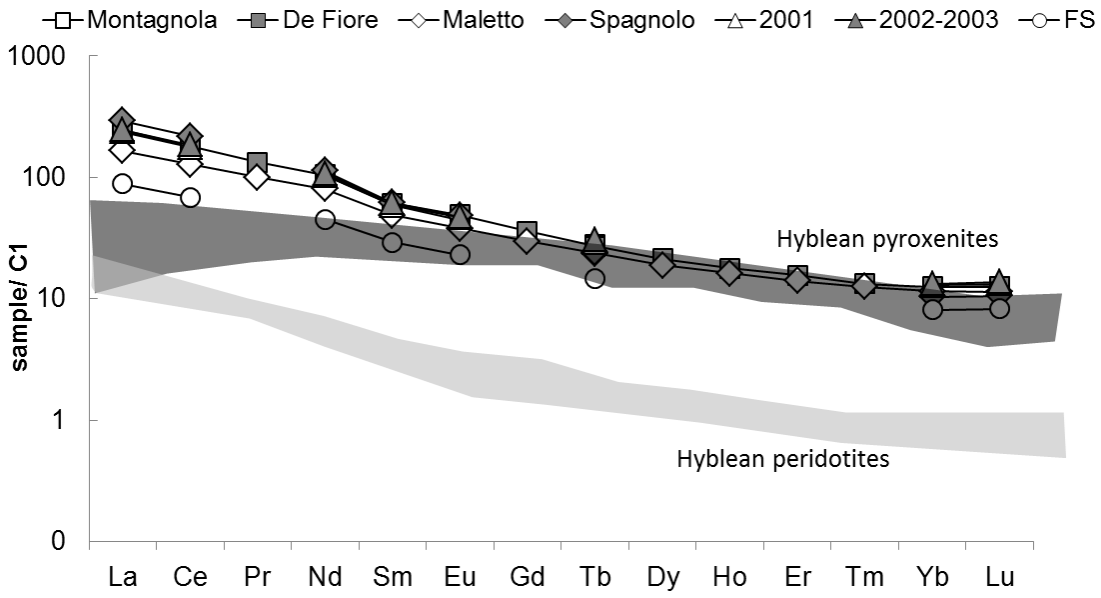

Fig 4.10- C1-normalized REE patterns of whole rock from eccentric and primitive Etnean lavas. The shaded gray and black areas are the REE pattern respectively from Hyblean peridotites and pyroxenites. Normalization to C1 is after McDonaugh & Sun (1989). Reported values of Etnean products: Maletto and Spagnolo are an average from this work, Tanguy et al., 1997 , Armienti et al., 1988 and Armienti et al., 2004; S11 is from this work; FS is from Coltelli et al., 2005; 2001 is an average from Clocchiatti et al., 2004, Viccaro et al., 2006, Corsaro et al., 2006, Viccaro et al., 2008; 2002-2003 is an average from Clocchiatti et al., 2004, Viccaro et al., 2008 ; De Fiore is from Corsaro et al., 2009, Armienti et al., 2004, Tanguy et al., 1997, Armienti et al., 1988; Montagnola is an average from Armienti et al., 1988, Corsaro et al., 2009, Viccaro et al., 2008.

Spiderdiagram (**Fig 4.11**) displays a similar general pattern (ie the slope) but with different total concentrations; LIL elements (K, Ba,Rb, etc) are generally higher than HFSE (ie. Zr, Nb, Hf etc). Due to the very higher solubility of LILE in supercritical aqueous fluids respect to HFSE, the characteristic pattern of this Etnean lavas highlights a possible relation with a metasomatizing fluid phase in the mantle.

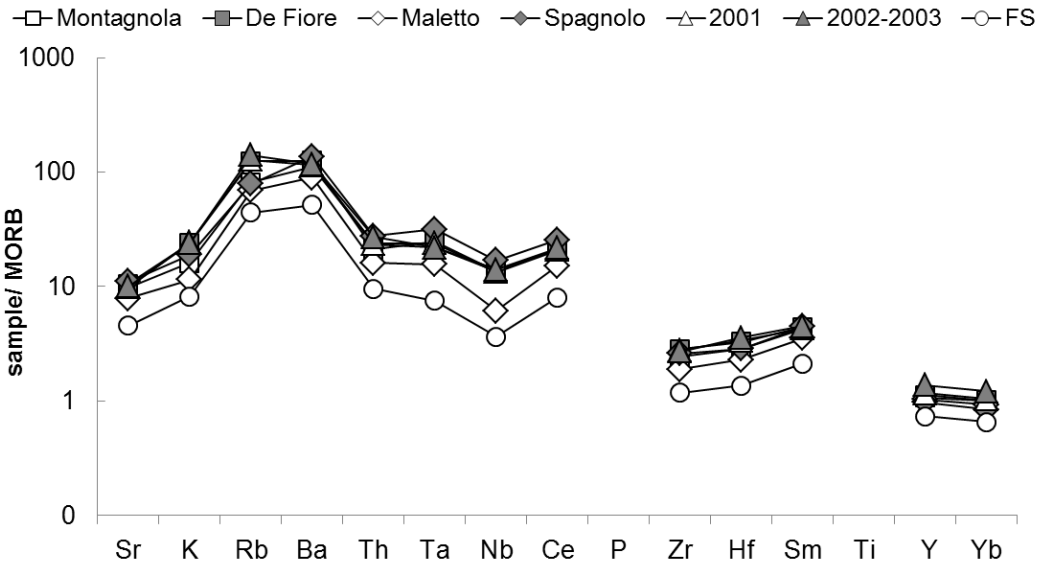

Fig 4.11- Spider diagram of whole rock from primitive Etnean lavas based on the element array of Pearce 1983. Normalization to MORB from Anderson 2007. Average values as in fig 4.10.

Fig 4.12 plots concentration ratios among some incompatible trace elements for the studied Etnean lavas and the Hyblean peridotites and pyroxenites (shaded areas). Etna samples, characterized by positive or negative trends, partially or totally plot in the area of Hyblean peridotites, suggesting a close similarity of their mantle source with the Hyblean mantle.

More in detail, Spagnolo is the highest in Th/Yb and Ta/Yb, suggesting that garnet was present in the mantle source (retaining Yb). The alternative possibility that some fluid-driven Th enrichment (Th is slightly fluid-mobile) could equally be viable given that Th concentration (in average ~8 ppm) is more than twice the OIB-HIMU value (3 ppm). The FS tephra are at the opposite end of this trend.

The observed variations trends could depict a mixing between two different mantle sources or, more simply, they could account for variable degrees of melting of the same mantle. In both the cases, the effects of fractional crystallization in lavas must be also quantified. These calculations will be dealt with the next section.

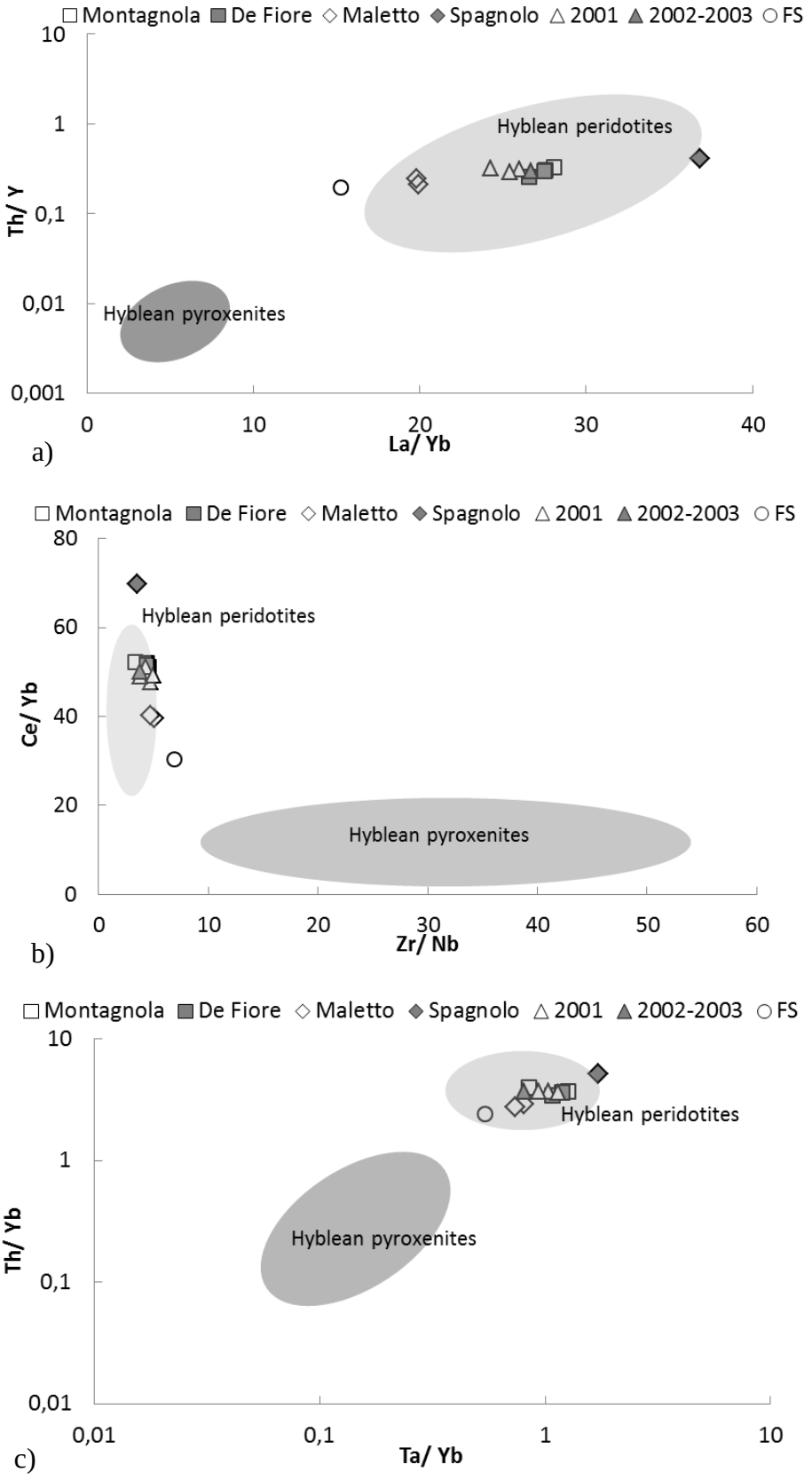

Fig 4.12 a) La/Yb vs Th/Y, **b)** Zr/Nb vs Ce/Yb, **c)** Ta/Yb vs Th/Yb plots of whole rock from Etnean lavas. Values of trace elements from different authors (see table 8).The shaded areas correspond to trace elements ratios in peridotitic and pyroxenitic nodules respectively from this work and Sapienza and Scribano (2000).

	Montagnola			De Fiore				Maletto			
	(1)	(2)	(3)	(4)	(5)	(1)	(3)	(6)	(4)	(1)	(5)
n.	3	2	3				8	1			
Rb	30,00	31,10	26,82	46,10	46,00	43,00	43,79	20,39	24,40	27,50	27,00
Cs		0,60	0,50	0,90	1,00		0,88	0,34	0,49		0,70
Sr	1053,67	1144,00	1064,00	1074,00	1203,00	1146,00	1206,75	836,90	890,00	848,50	896,00
Ba	539,00	579,50	553,33	612,00	640,00	600,00	657,75	444,10	448,00	439,00	468,00
Ta		1,95	2,43	2,56	2,28		2,58	1,58	1,67		1,44
Th		9,20	7,10	7,11	7,20		7,86	5,64	5,82		5,40
U		2,49	1,99	2,11	2,16		2,31	1,36	1,70		1,59
Zr	159,33	167,50	182,70	221,00	195,00	183,00	195,34	132,00	154,00	110,50	134,00
Hf		4,00	4,00	5,00	4,30		4,46	3,21	3,10		3,30
Nb	44,00	50,00	41,70		43,00	47,00	44,50	25,89		27,00	28,10
La	57,00	64,55	53,00	52,70	56,00	59,00	59,20	38,52	37,70	41,00	39,00
Ce	110,67	120,30	100,07	104,00	108,00	120,00	111,00	76,94	73,30	85,50	79,00
Pr					12,60						9,50
Nd		52,80	44,07		49,00		48,90	37,16			38,00
Sm		9,75	8,24		9,30		9,36	7,36			7,50
Eu		2,71	2,49	2,97	2,73		2,82	2,21	2,23		2,21
Gd					7,40						6,10
Tb		1,21	0,89	0,92	1,07		1,03	0,89	0,83		0,93
Dy					5,40						4,80
Ho					1,01						0,92
Er					2,58						2,32
Tm					0,34						0,32
Yb		2,30	1,92		2,11		2,15	1,95			1,96
Lu		0,35	0,29		0,32		0,32	0,29			0,29
Y	22,67	27,95	23,47		27,80	23,00	26,60	23,05		22,00	25,90
Ni	34,33	32,00	36,33	29,00	34,00	27,00	30,75	54,42	52,00	49,00	54,00
Cr	49,33	49,50	56,33	83,00	36,00	26,00	40,50	191,80	174,00	136,00	132,00
V	309,33	289,00	302,33		327,00	329,00	315,50	297,90		310,00	325,00
Co		44,95	41,67	43,00	42,00		40,25	43,48	45,10		46,00
Cu			125,33				142,25	118,30			

[1]From Armienti et al.,1988 [4]From Tanguy et al., 1997 [7] From Clocchiatti et al., 2004 [10] From Coltelli et al., 2005 n= number of analyses

[2]From Viccaro et al., 2008 [5] From Armienti et al.,2004 [8]From Viccaro et al., 2006

[3] From Corsaro et al., 2009 [6]From this work [9] From Corsaro et al., 2006

Table 8- Trace elements abundance of whole rock from studied Etnean samples.

	Spagnolo				2001				2002-2003		FS
	(6)	(4)	(5)	(1)	(7)	(8)	(2)	(9)	(7)	(2)	(10)
n.	2	2	4		3	5	4	7	1	2	6
Rb	26,45	28,05	27,00	30,50	45,80	47,13	46,83	44,89	46,1	54,85	16
Cs	0,54	0,72	0,70		0,93			0,93	0,88	1	0,427
Sr	1179,00	1228,50	896,00	1250,00	1055,00	1070,00	1130,00	1097,00	1023	1179	501
Ba	655,90	711,50	468,00	679,50	573,33	555,33	599,00	568,00	557	617	259
Ta	3,05	3,29	1,44		2,53	2,27	2,35	2,38	2,35	2,05	0,75
Th	9,07	10,25	5,40			8,07	9,30	7,53		9,45	3,34
U	2,55	2,74	1,59			2,07	2,69	2,19		2,565	1
Zr	185,10	191,00	134,00	168,50	196,67	191,33	194,25	196,14	185	194,5	83
Hf	3,96	4,09	3,30		4,52	5,00	5,00	4,39	5,05	5	1,92
Nb	52,84		28,10	58,75	46,03	40,33	51,25	38,96	41,3	51,5	12
La	65,18	69,05	39,00	72,75	53,00	53,40	65,00	52,57	49,3	68,05	21
Ce	123,40	132,00	79,00	143,00	103,00	105,00	122,75	102,00	98,2	127,85	42
Pr											
Nd	52,81		38,00		46,03	45,67	56,70	45,40	44,4	56,75	21
Sm	9,42		7,50		8,38	8,77	9,95	8,88	8,16	10,8	4,45
Eu	2,73	2,87	2,21		2,60	2,69	2,85	2,68	2,53	2,955	1,34
Gd											
Tb	0,91	0,90	0,93		0,98	1,12	1,32	0,97	0,94	1,36	0,55
Dy											
Ho											
Er											
Tm											
Yb	1,77		1,96		2,01	2,20	2,50	2,07	1.98	2,55	1,38
Lu	0,27		0,29		0,31		0,38	0,32	0.31	0,39	0,21
Y	22,37		25,90	22,50	26,80	25,27	30,03	25,77	26.1	31,6	17
Ni	65,17	49,55	54,00	53,00			33,75	31,14		34	225
Cr	214,50	163,50	132,00	152,75		37,67	39,00	61,00		46,5	1174
V	263,40		325,00	250,75		298,67	298,50	302,14		288,5	221
Co	39,32	34,70	46,00			38,13	36,65	42,29		43,8	55
Cu	105,90					133,00		133,14			85

[1] From Armienti et al.,1988
[2] From Viccaro et al., 2008
[3] From Corsaro et al., 2009
[4] From Tanguy et al., 1997
[5] From Armienti et al.,2004
[6] From this work
[7] From Clocchiatti et al., 2004
[8] From Viccaro et al., 2006
[9] From Corsaro et al., 2006
[10] From Coltelli et al., 2005
n= number of analyses

Table 8- Trace elements abundance of whole rock from studied Etnean samples. We reported also the composition of two other Etnean eccentric products (2001 and 2002-2003)

Melting and crystallization processes

Here we model melting and crystallization associated with the genesis of the investigated Etnean lavas and we calculate the effects of these processes on major and trace element geochemistry. Given the similarity found in the trace elements between the Etnean lavas and Hyblean peridotitic mantle (see **Figs 4.12 a,b,c**), we assumed the Hyblean lherzolite as a starting mantle source. In doing so, we check if an Hyblean-like peridotite is able to reproduce the whole compositional spectrum of major and trace elements of our samples.

Our approach is otlined as below:

1) In order to simulate a melting process, we started from major element compositions of the analysed Hyblean lherzolite XIH-3 and using the MELTS code we computed the chemical composition of the melts related with increasing melting percentages (see **Table 9a**). We simulated an isobaric batch melting at 1 GPa, increasing the temperatures from the anhydrous solidus (T~1300°C, table 9) to 13% of melting reached at 1400 C° and considering the system buffered for fO_2 at QFM. Attemps using a slightly more fertile Hyblean lherzolite from the literature (i.e 11% cpx instead of 8% from XIH-3 sample) produced negligible variations in the major element composition of the produced melts. In **Fig 4.13** we reported with the black arrows the variation in the composition of some major elements (Mg, Na, Al, Ca) connected with a isobaric melting process. Similar results was obteined simulating an isothermal melting process by decreasing the pressure from 0.7 to 0.2 GPa at 1250°C and considering the system buffered respect to QFM. In **Fig 4.14** we compared the NaO and CaO variations during an isobaric (black curve) and isothermal (gray curve) melting: the same melting percentage associated with the two different processes lead almost to the same melt composition. The complete tables of these modeled trials are reported in appendix.

2) Starting from the resulting major element compositions from the different melting percentages of the same mantle source, we simulated crystallization processes. In detail, we considered an isobaric crystallization processes at 0.4 GPa decreasing gradually the temperatures from ~ 1200 to 1050C° in a melt characterized by ~3% of H_2O (H_2O values typical of Etnean melt inclusions related to mildly or highly explosive events; Metrich et al., 2004, Spilliaert et al., 2006, Kamenetsky et al., 2007). In **Fig 4.13** we represent the crystallization model path (red arrows) for selected major elements (Mg, Na, Al, Ca). The complete results of the calculations are reported in appendix.

Comparison of the computed curves with the compositions of Etnean lavas in **Fig 4.13** shows that variable melting of the same source, coupled to crystallization, is able to fully explain the whole compositional range exhibited by Etnean lavas. In detail, the results allow to interpret the lavas as coming from degrees of melting growing from Spagnolo (~1%) to FS (~9%), together with variable percentages of crystallization (~0-5% for FS, ~12-14 % for Maletto, ~ 13-17% for Montagnola and De Fiore and finally ~ 4-16% for Spagnolo). These crystallization percentages are estimated starting from the composition of melts from an isobaric melting. If we consider an isothermal melting the crystallization percentages will be subjected only to a slight variation.

3) Once obtained the fractions of batch melting and crystallization related with each lava, using the measured trace elements contents, we went back to initial trace elements composition of the mantle source characterizing each investigated lavas. In doing so, we used the equation reported below for batch melting to achieve the source composition for Zr, Nb, Ce, Yb, Th, La, Y, Ta (the selected incompatible trace elements from those represented in the ratios of **Fig 4.12**):

$$C^{l}_{i} = C^{0s}_{i} / D(1-F)+F \qquad [1]$$

where C^{l}_{i} and C^{0s}_{i} are the concentration of i-element respectively in the melt and in the solid source; F is the melting fraction that varies from 0 to 1 and D is the partition coefficient of the element (Morbidelli, 2003). The mineral-melt partition coefficients for mafic and ultramafic melts used for the calculation are from White (2009).

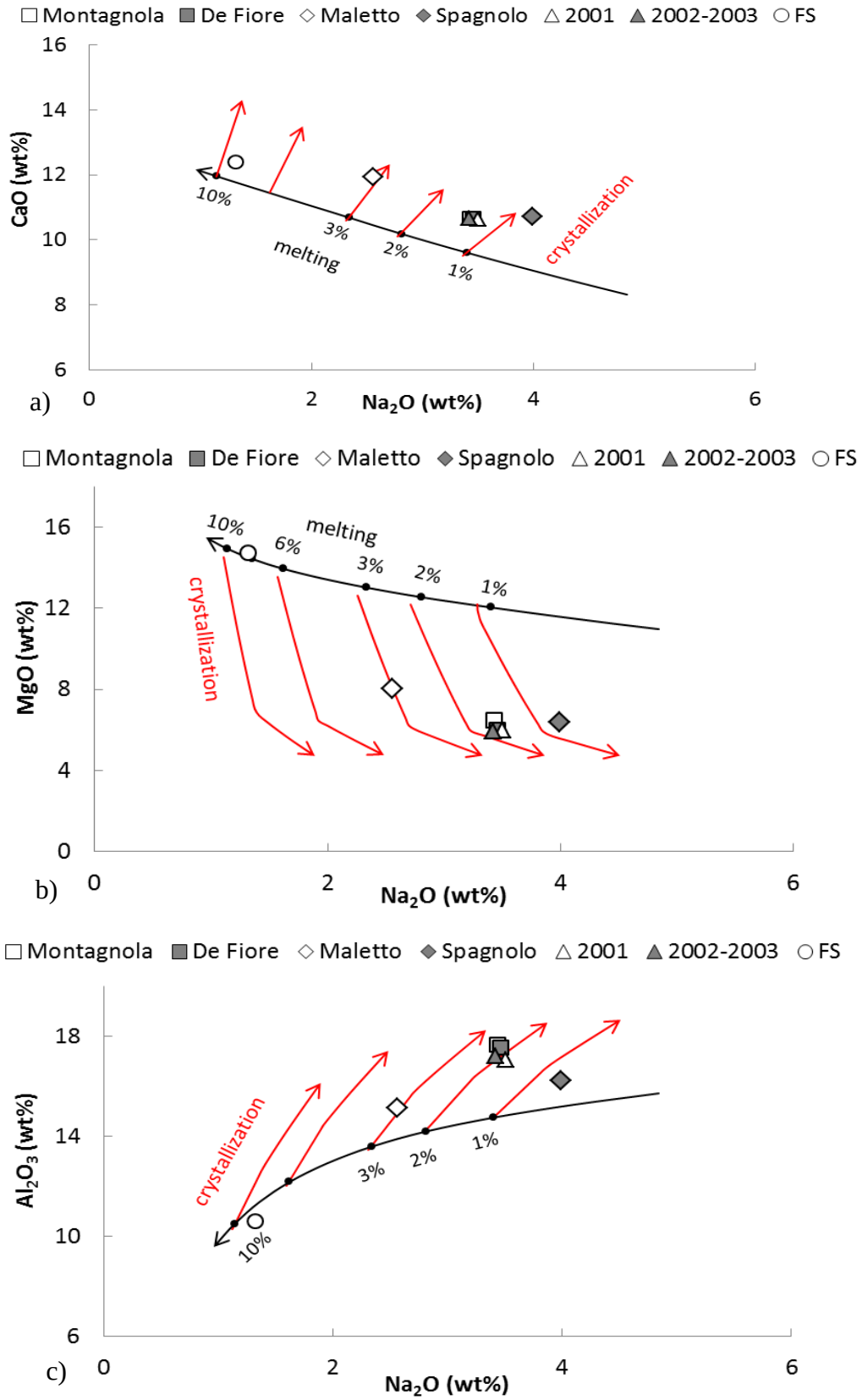

Fig 4.13 a) Na_2O vs CaO, **b)** Na_2O vs MgO, **c)** Na_2O vs Al_2O_3 variations connected with melting (black curve) and crystallization (red arrows) processes. Labels are referred to percentages of melting. Conditions are: T=1100-1400°C (melting process) and T=1200-1050°C (crystallization process) at P=1GPa and QFM buffer. Simulation carried out by MELT code. Further details into the text.

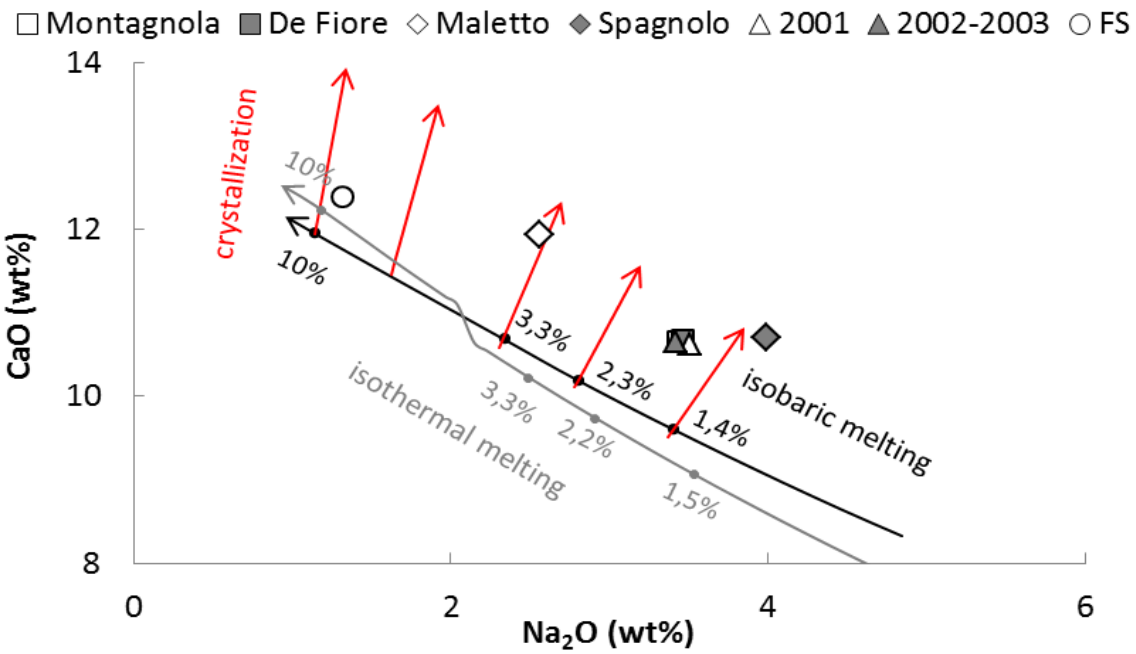

Fig 4.14 Na_2O vs CaO variations connected with isobaric melting (black curve), isothermal melting and crystallization (red arrows) processes. Labels are referred to percentages of melting. Conditions are: T=1100-1400°C (melting isobaric process) and T=1200-1050°C (crystallization process) at P=1GPa and P=7400-2000 bars at 1250°C and (melting isobaric process). Simulation carried out by MELT code. Further details into the text.

The calculated trace element concentration of the mantle source modeled for each Etnean lava are reported in **Table 9b** and the corresponding ratios plotted in **Fig 4.15**. As evident from **Fig 4.15**, the principal process that can originate a substantial variation in the geochemical ratios is partial melting, while the estimated percentages of crystallization can produce very small changes (see arrows in the corner of figures). As a main result, the calculations for Zr/Nb vs Ce/Yb and Th/Y vs La /Yb ratios of the Etnean lavas bring back to a primordial source that testifies a common origin for all the investigated lavas (**Fig 4.15**). Moreover, the source is resulted to mainly have a peridotitic nature in terms of trace element signature, nevertheless it is also evident a significant contribution from the pyroxenitic veins. In both trace elements ratio plots Zr/Nb vs Ce/Yb and Th/Y vs La /Yb, it in fact falls along an hypothetical mixing curve between a peridotitic and pyroxenitic end-member, with about 10-20% of pyroxenite (**Fig 4.16**).

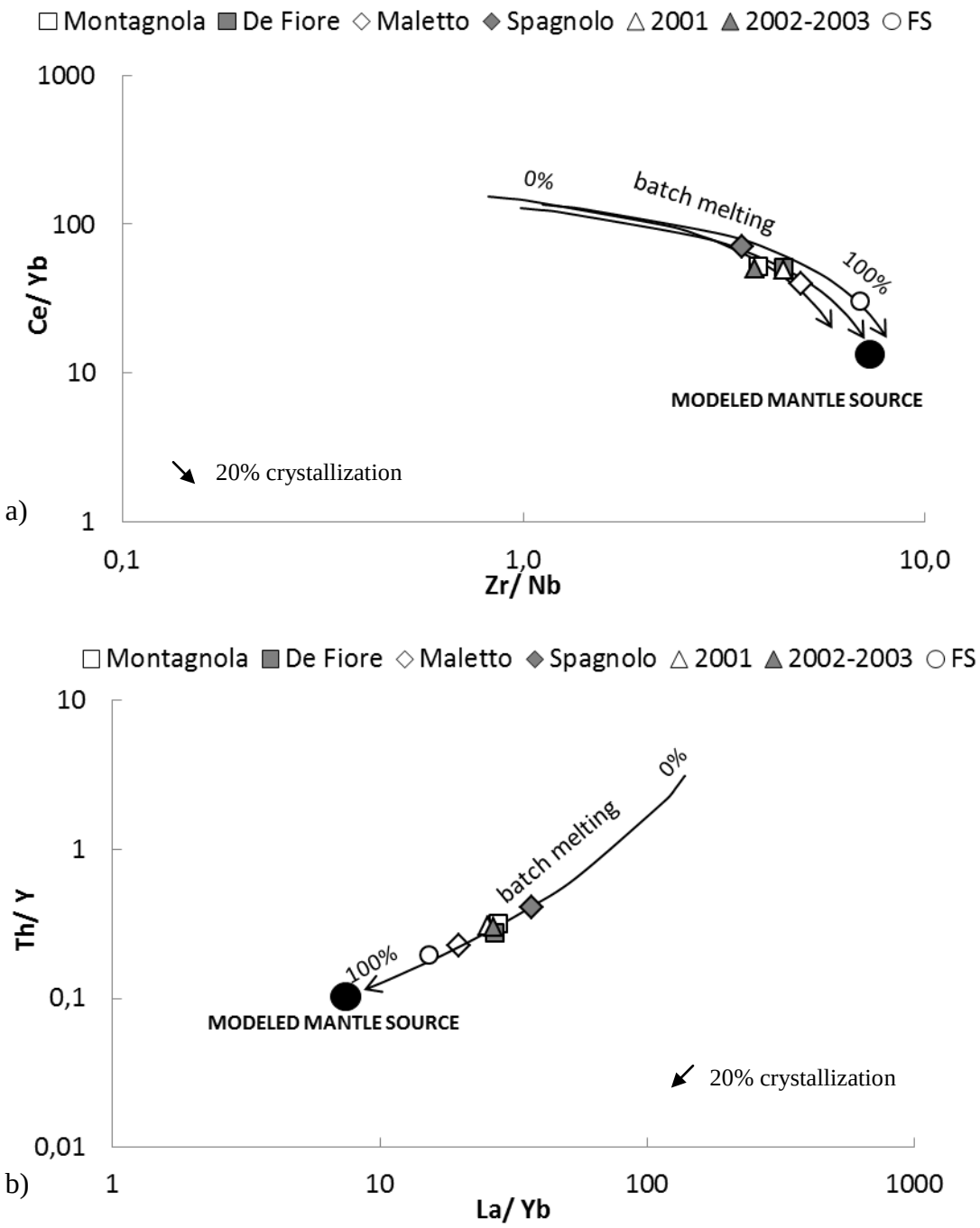

Fig 4.15 a) Zr/Nb vs Ce/Yb and b) La/Yb vs Th/Y ratio variations connected with the calculated melting percentages. In the top of figure the calculations corresponding to different melting percentages bringing back each lava to mantle source slightly different while in the second figure the calculated mantle sources are practically coincident. The small black arrow in the corner of the two plots displays the maximum effect due to 20% crystallization.

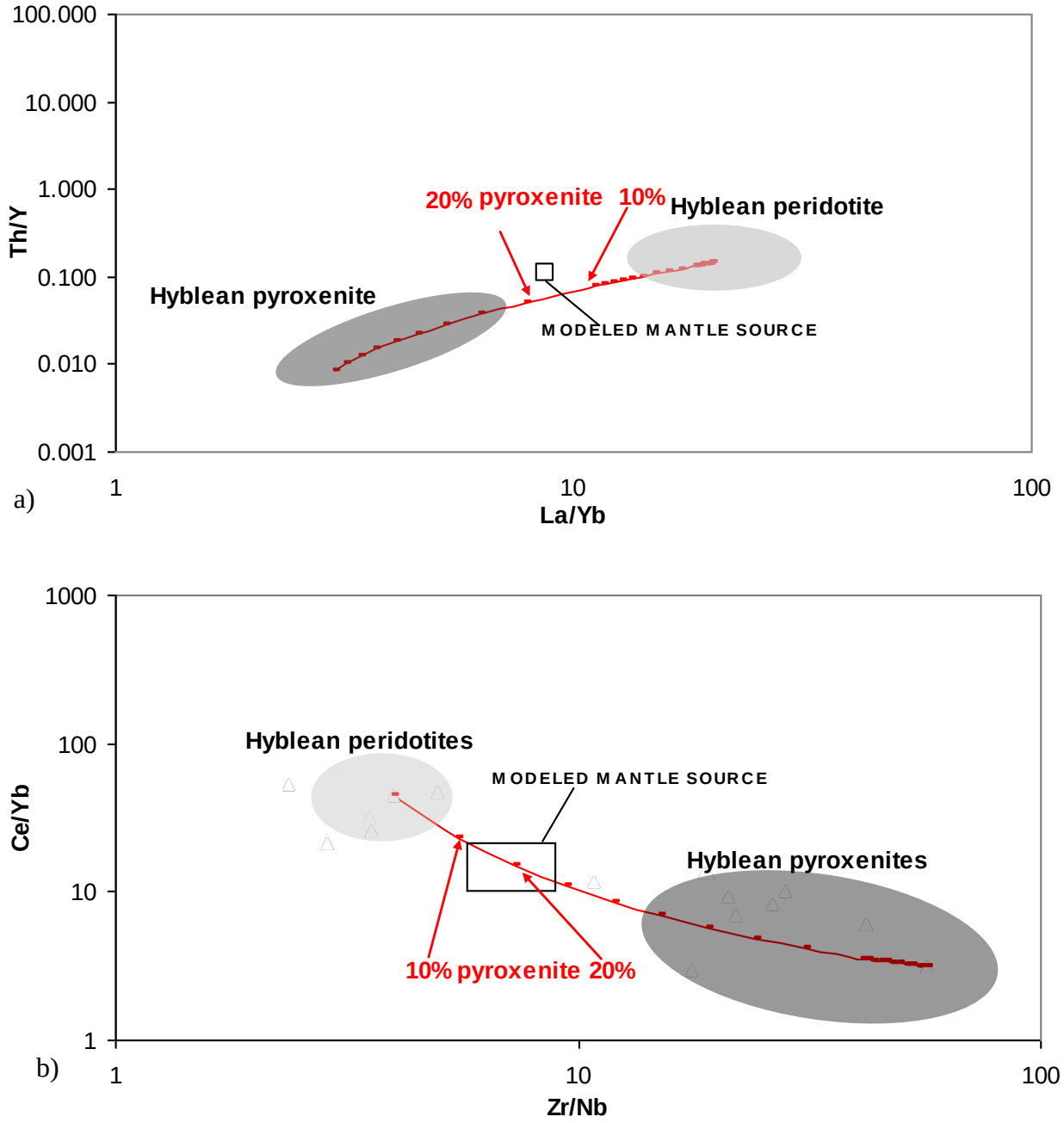

Fig 4.16- Mixing curves between an hypothetical peridotitic and pyroxenitic end-member in a) La/Yb vs Th/Y and b) Zr/Nb vs Ce/Yb plot. The calculated mantle source for the Etnean lavas result compatible with a peridotitic mantle veined by 10-20% of pyroxenites.

a)

T (°C)	Pressure (bar)	F (melt fraction)	SiO_2 (wt%)	TiO_2	Al_2O_3	Fe_2O_3	FeO	MgO	CaO	Na_2O
1310	10000	0,003	50,18	0,82	15,71	1,06	8,09	10,97	8,32	4,84
1320	10000	0,008	49,54	0,87	15,25	1,11	8,64	11,53	8,98	4,09
1330	10000	0,014	48,98	0,90	14,75	1,15	9,14	12,06	9,62	3,40
1340	10000	0,023	48,57	0,92	14,19	1,18	9,57	12,56	10,20	2,81
1350	10000	0,033	48,36	0,93	13,59	1,21	9,85	13,04	10,70	2,34
1360	10000	0,046	48,27	0,89	12,92	1,24	10,13	13,50	11,11	1,94
1370	10000	0,061	48,28	0,84	12,18	1,26	10,40	13,97	11,45	1,62
1380	10000	0,080	48,38	0,76	11,37	1,29	10,65	14,45	11,73	1,36
1390	10000	0,101	48,55	0,68	10,51	1,32	10,86	14,96	11,97	1,14
1400	10000	0,126	48,79	0,60	9,58	1,35	11,04	15,51	12,17	0,96

b)

MODELED MANTLE SOURCE	Zr (ppm)	Nb	Zr/Nb	Ce	Yb	Ce/Yb	Th	Yb	Th/Y	La	Y	La/Yb
Spagnolo	12	1.95	5.90	3.59	0.18	19.94	0.2	0.23	0.11	2	1.78	8.70
Fs	15	1.8	8.06	3.8	0.22	17.62	0.2	0.23	0.11	2	1.78	9.70
Maletto	7.8	1.1	7.09	3.86	0.23	16.78	0.2	0.23	0.11	2	1.78	10.70
Montagnola	6.9	0.96	7.19	3.03	0.21	14.57	0.2	0.23	0.11	2	1.78	11.70

Table 9- a) Variable composition of a melt obtained by simulating a progressive isobaric melting of a lherzolite; b) Element trace composition of the modeled Etnean mantle source obtained by batch melting formula (see the text for further details).

4.3 Sr-Nd isotopes

4.3.1 Hyblean area

Sr- and Nd-isotope data measured in clinopyroxenes from peridotites and pyroxenites are listed in **Table 7** and plotted in **Fig 4.17**. The peridotites showed almost homogeneous $^{86}Sr/^{87}Sr$ and $^{143}Nd/^{144}Nd$ values of ~0.7029 and ~0.5129, respectively, while the pyroxenites exhibited $^{143}Nd/^{144}Nd \approx 0.5130$ and a more variable $^{86}Sr/^{87}Sr$ ratio between 0.7028 and 0.7031. As shown in Fig 4.17, our values are consistent with those reported by Bianchini et al. (2010) and Tonarini et al. (1996). Consideration of the complete data set indicates the absence of any appreciable differences in the $^{86}Sr/^{87}Sr$ ratios among peridotites and pyroxenites, while their $^{143}Nd/^{144}Nd$ ratios are slightly but significantly more variable. The more radiogenic (ie, ^{143}Nd richer) value of pyroxenites with respect to peridotites confirms the presence of two distinct compositional groups, as already noticed from trace element geochemistry and evidence once again (see results of Zr/Nb ratio) a slight tendence of pyroxenitic and peridotitic nodules respectively toward a depleted mantle and an HIMU-type source.

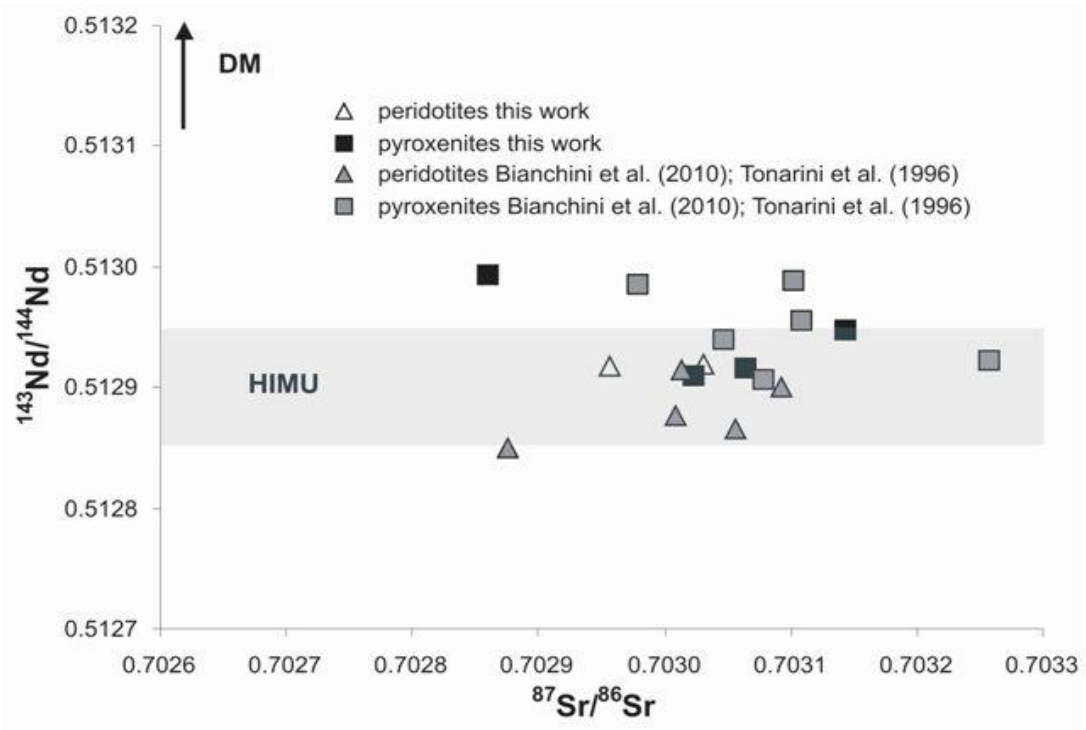

Fig 4.17- Sr-Nd isotopic composition of Hyblean xenoliths, this work and literature (Tonarini et al., 1996; Bianchini et al., 2010). Nd isotopes of peridotites plots entirely in the HIMU field , while higher $^{143}Nd/^{144}Nd$ in pyroxenites may suggest DM end member. The DM and HIMU fields from Zindler and Hart (1986).

4.3.2 Etna

Sr and Nd isotopic analyses for studied samples are taken from literature; given the high homogeneity of targeted eruptions we can safely assume that they may well be consistent with data derived from this work (see **Table 10**; data from Viccaro and Cristofolini, 2008; Kamenetsky and Clocchiatti, 1996; Armienti et al., 2004).

In **Fig 4.18** are portrayed the $^{87}Sr/^{86}Sr$ vs $^{143}Nd/^{144}Nd$ systematics for the Etna rocks compared with Hyblean xenoliths. The $^{143}Nd/^{144}Nd$ is in the range of 0.512860 -0.512890 whereas $^{87}Sr/^{86}Sr$ varies in the range 0.7033 - 0.7037.

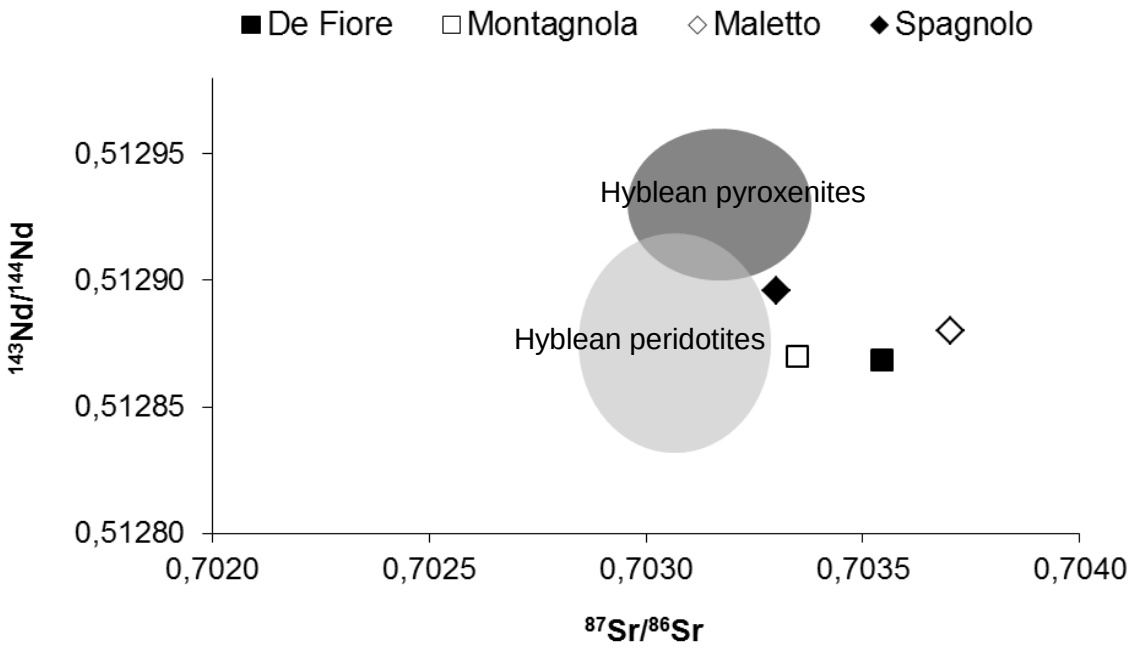

Fig 4.18- Sr-Nd isotopic composition of Hyblean xenoliths from literature (see table 8). Sr-Nd isotopic composition of Hyblean xenoliths from this work and from literature (Tonarini et al., 1996; Bianchini et al., 2010).

M. Spagnolo shows the most depleted composition (ie the least radiogenic Sr and the highest radiogenic Nd) . Also, with respect to the Hyblean xenoliths dataset the Etnean samples are higher in $^{87}Sr/^{86}Sr$ but in the same $^{143}Nd/^{144}Nd$ range of peridotitic nodules, with M. Spagnolo being the closest to Hyblean pyroxenites.

Armienti et al. (2004) recognized an inverse correlation, within the "mantle array", of Sr and Nd isotopes among early tholeiities and alkaline basalts, with also a significant distinction between pre-1971 (historical) alkaline lavas (depleted mantle source) with alkaline post-1971 basalts (enriched mantle source) . Armienti et al. (2004) interpreted this variation due to a mixing process between a depleted mantle source and a slab-released fluids, in the geodynamical context of

the retreating Ionian slab. They were also able to infer a lower crustal contaminating agent and, in a lesser amount, also of the sedimentary basement of Mt. Etna. Indeed isotopic data from Maletto show a decoupling between the $^{87}Sr/^{86}Sr$ and $^{143}Nd/^{144}Nd$ ratios: the high $^{87}Sr/^{86}Sr$ are not accompanied by a correspondent isotopic shift of the isotopic Nd, consequently these were interpreted as a result of the product of selective contamination of sediments-derived Sr. This ending was also raised by Marty et al. (1994), who attributed the Sr-Nd isotopic variations, measured in some tholeiitic and alkali trachybasalt lavas from Etna, to sediment contamination .

Taking into account these interpretations and considering that the Sr-Nd isotopic values from investigated eccentric products are within the variation range of those measured by the above mentioned authors, we can imagine a similar process for the lavas investigated in this work.

Thus starting from the most primitive isotopic values of Spagnolo center, that reflect both a peridotitic and pyroxenitic contribution, a shallow contamination level by sedimentary rocks could move the primordial isotopic marker of this lavas toward more radiogenic values.

Sample	De Fiore[1]	Montagnola[2]	Maletto [3]	Spagnolo[3]	Et 2001[1]
$^{87}Sr/^{86}Sr$	0,703544	0,703350	0,703703	0,703300	0,703576
$^{143}Nd/^{144}Nd$	0,512869	0,512870	0,512880	0,512896	0,512874

[1] From Viccaro et Cristofolini, 2008

[2] From Armienti et al., 2004

[3] From Kamenesky et Clocchiatti, 1996

Table 10 - Sr-Nd isotopic composition of primitive products from literature.

5.Noble gas from fluid inclusions

When a crystal grows in the presence of a fluid phase, fluids may be trapped as imperfections on the growing crystal to form primary fluid inclusions (hereafter FI) and represent a track of the fluid phase in equilibrium with magma (or , in the case of secondary FI, might represent late stage fluid circulation). The trapped fluid may be liquid, vapour, or also a supercritical fluid and its composition may include essentially pure water, brines, gas bearing liquid and silicate, sulphides or carbonate melts.

Our study is focused on the investigation on the noble gases content in FI (He, Ne, Ar abundances and isotopic ratios) as they represent important geochemical tracers. Indeed they are of great interest to define the mantle source characteristics and to study its evolution through the time, being also capable to give information on some pre- and post-eruptive processes that characterized the history of a magma.

Three main characteristics make them particularly sensitive as geochemical tracers: 1) the isotope composition of each noble gas, that are markers of sources, 2) the high incompatibility that makes them depleted in the solid Earth and 3) the chemical inertia.

5.1 Hyblean area

5.1.1Chemical and isotopical composition of fluid inclusions

FI from olivine and pyroxene crystals of Hyblean ultramafic xenoliths represent a primary gaseous phase (dominated by CO_2) coexisting with growing minerals at mantle depths, as demonstrated by thermobarometric and microthermometric studies carried out in the same area (Sapienza et al., 2005; Tonarini et al., 1996). The concentrations of noble gases in the studied xenoliths are listed in Table 11. The He content varied from 7.3×10^{-14} to 2.6×10^{-11} mol/g in mineral separates of peridotite nodules, and from 5.1×10^{-13} to 3.4×10^{-11} mol/g in those of pyroxenite (**Fig 5.1**). The He abundance in peridotites is in overlap with the range reported for Hyblean samples by Sapienza et al. (2005). The Ar concentration varies from 1.89×10^{-13} to 6.64×10^{-12} mol/g and from 8.2×10^{-13} to 3.2×10^{-11} mol/g, respectively. The He -Ar plot in **Fig 5.1** shows a positive correlation, which implies that samples He-richer are also Ar-richer; this behaviour was observed in all the investigated samples, although with different He/Ar ratios.

The He and Ar concentrations differ systematically among the cogenetic minerals (olivines, orthopyroxenes, and clinopyroxenes) of each sample (see **Table11**), being slightly higher in clinopyroxenes and orthopyroxene than in olivine. The $^3He/^4He$ ratios were also higher in clinopyroxenes and orthopyroxene. This partially agrees with the findings of Sapienza et al. (2005),

who reports generally comparable values in olivine and orthopyroxene but lower than in coexisting clinopyroxenes.

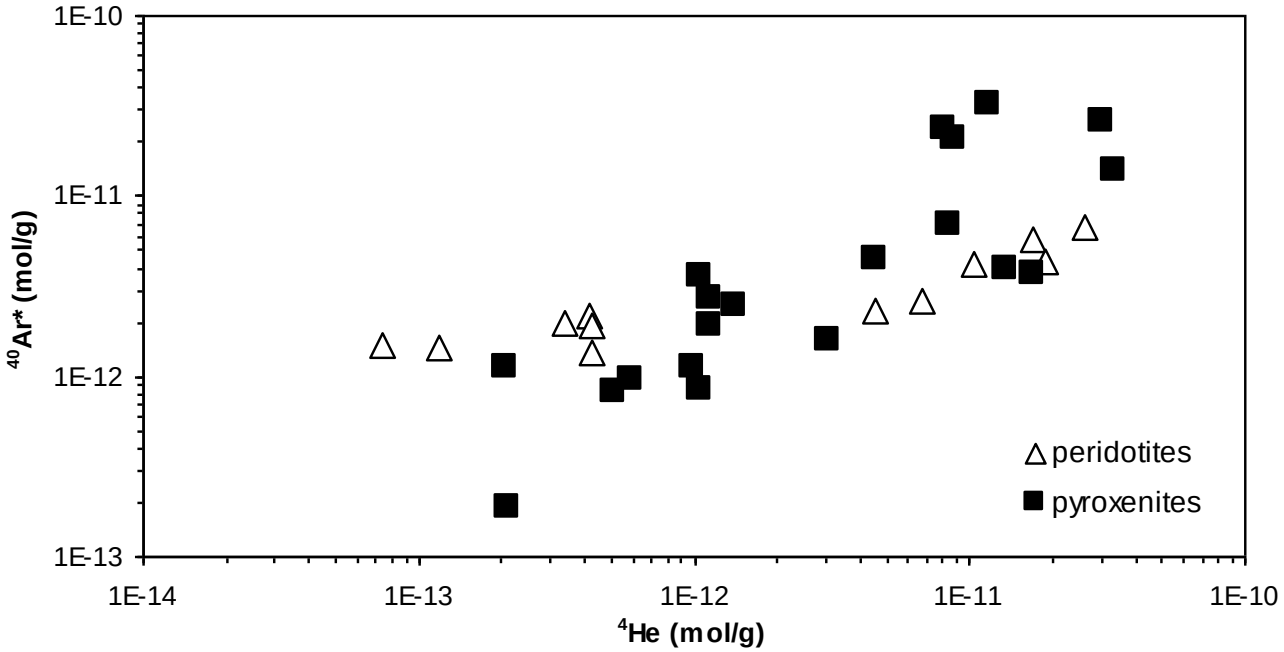

Fig 5.1 - ^{40}Ar* vs ^{4}He concentrations of fluid inclusions from Hyblean peridotites and pyroxenites.

It is well known that FI can be contaminated by air, thereby affecting also the source signature of noble gases. In order to evaluate the air contribution in our samples, we plotted ^{4}He/^{20}Ne versus ^{40}Ar/^{36}Ar ratios, as shown in **Fig 5.2**. The ^{4}He/^{20}Ne ratio varied between 61 and 4740, while that of ^{40}Ar/^{36}Ar varied between 316 and 939 (^{40}Ar/^{36}Ar atm = 295.5). We observe that all of the samples plot on a computed curve of the binary mixing between an atmospheric end member and a hypothetical MORB source (Graham et al., 2002; Marty et al., 1983), thereby confirming atmospheric contamination of the gases released from FI (**Fig 5.2**; see caption for further details). It is noteworthy that the highest ^{4}He/^{20}Ne and ^{40}Ar/^{36}Ar ratios (resembling the lowest air contamination of our samples) were generally observed in samples with the highest gas contents released from FI. The most likely origins of the atmospheric signatures are: (1) air contamination in the mantle due to subduction of atmospheric components (e.g., Sarda, 2004) and (2) air entrapment in microcracks of minerals during or after the eruptive activity (e.g., Nuccio et al., 2008).

The mantle-contamination hypothesis can be rejected based on the ^{40}Ar/^{36}Ar ratios measured in the gas emission of Mofeta dei Palici, located in the northern Hyblean area and close to

Quaternary volcanic systems and showing $^{40}Ar/^{36}Ar$ values in the range of 1600–2000, which are consistent with a mixing between air and a MORB mantle (Nakai et al., 1997; INGV-PA database). These ratios are much higher than those measured in our FI. Given that the Hyblean mantle surely has $^{40}Ar/^{36}Ar$ ratios above 2000, the low $^{40}Ar/^{36}Ar$ ratios of FI cannot be inherited from the mantle but are probably caused by air contamination that occurs at shallow levels or after the entrapment of FI. Similar conclusions have been previously drawn by FI studies from other areas (Graham, 2002; Martelli et al., 2011; Nuccio et al., 2008; Porcelli et al., 2002). At the present state of knowledge, we therefore believe that air components entrapped in microcracks of minerals during or after their eruption provide the most likely explanation of air contamination in our FI (Ballentine and Barfod, 2000).

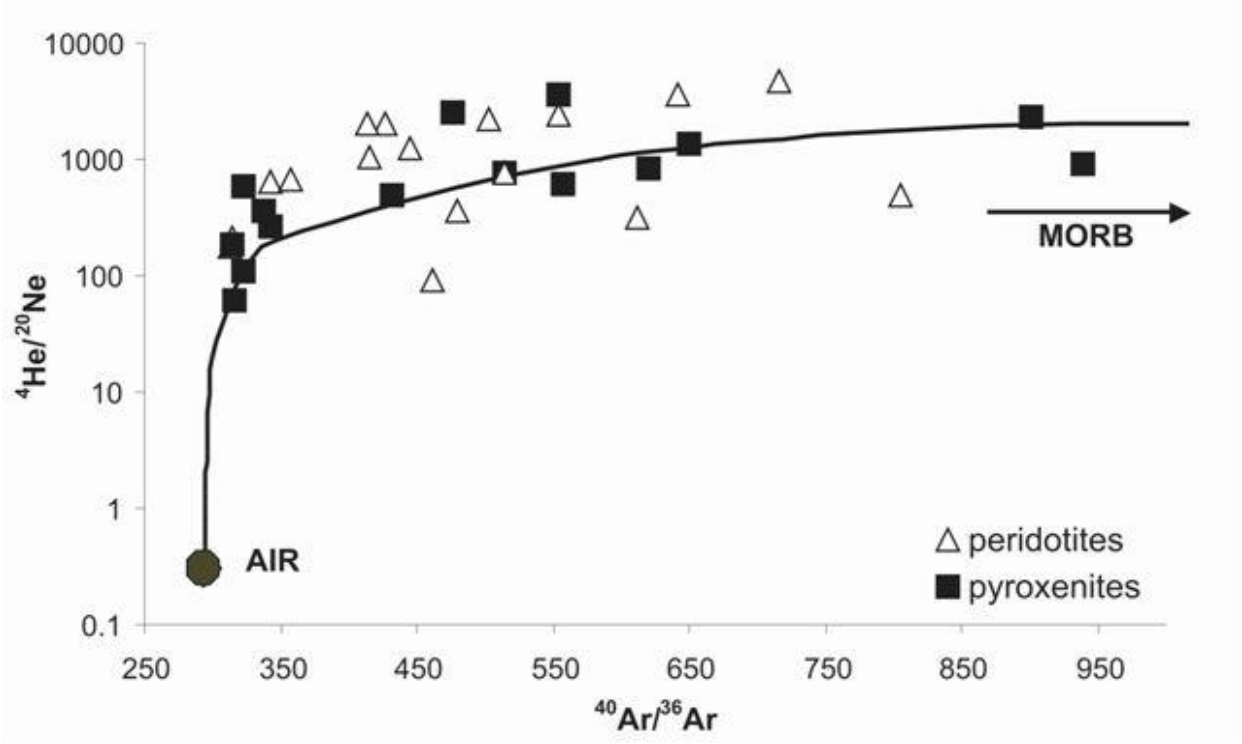

Fig 5.2 - $^4He/^{20}Ne$ vs $^{40}Ar/^{36}Ar$ ratios of fluid inclusions from Hyblean xenoliths. The curve defines a mixing trend between two end-member: 1) MORB having $^4He/^{20}Ne$ ~10000 (Marty et al., 1983), $^{40}Ar/^{36}Ar$ ~40000 (Graham et al., 2002) AIR having $^4He/^{20}Ne$ =0.318, $^{40}Ar/^{36}Ar$ =295.5.

We tested if air contamination could affect the $^3He/^4He$ ratios using the well-known formula of Giggenbach et al. (1993) that uses $^4He/^{20}Ne$ of the atmospheric endmember to evaluate the degree of contamination of a sample. The results demonstrate that these corrections have practically negligible effects. The He contents in FI were in fact practically unmodified by air contamination due to the low concentration of He (5.2 ppm) in air. The ^{40}Ar concentration in FI was corrected by assuming that all of the ^{36}Ar found in the samples was of atmospheric origin, according to the following reported equation:

$$^{40}Ar^{*} = {}^{40}Ar_{meas} - (({}^{40}Ar/{}^{36}Ar)_{air} \times {}^{36}Ar_{meas})$$

where $^{40}Ar^{*}$ represents the corrected ^{40}Ar, and the "meas" subscript stands for "measured".

This equation allowed us to also compute an air-corrected-$^{4}He/^{40}Ar$ ratio, hereafter referred to as $^{4}He/^{40}Ar^{*}$ (see **Table11**).

The Rc/Ra values varies between 7.0 and 7.4 in the peridotites, in accordance with those observed by Sapienza et al. (2005), while is in the range 7.2 - 7.6 in the pyroxenites. The $^{4}He/^{40}Ar^{*}$ ratios varies between 0.4 and 8 in the peridotites and between 0.6 and 15 in the pyroxenites, i.e. in partial overlap with the former. The Rc/Ra ratios are plotted versus the $^{4}He/^{40}Ar^{*}$ ratios in **Fig 5.3**. Generally there is a positive trend from the peridotitic samples (having the lowest Rc/Ra and $^{4}He/^{40}Ar^{*}$ average ratios) to the pyroxenitic samples (having the highest values of both ratios).

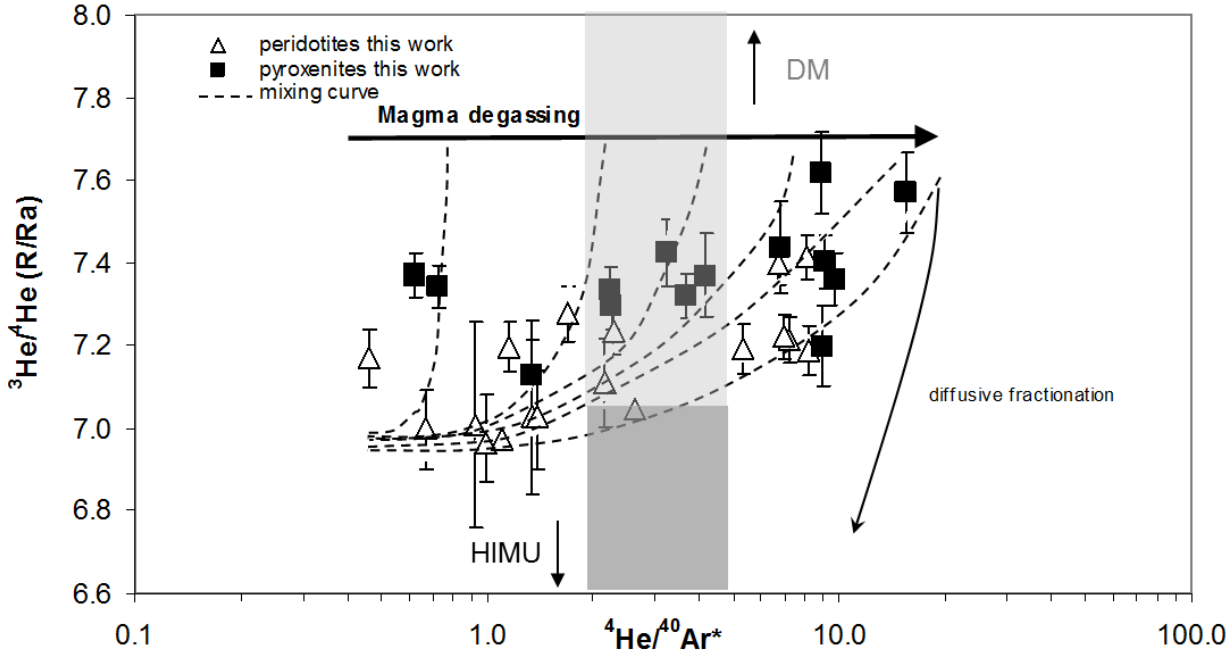

Fig 5.3 - Plot of $^{3}He/^{4}He$ (R/Ra) corrected for air contamination vs $^{4}He/^{40}Ar^{*}$ ratios of peridotites and pyroxenites. The dashed curves result from a mixing, which is a consequence of metasomatic processes, between a DM and a HIMU end-member. The dark thick arrow indicates the variations of $^{4}He/^{40}Ar^{*}$ ratio during degassing processes. See the text for more information about DM (light gray area) and HIMU (black area) sources. The meaning of the diffusive fractionation curve (thin curve) is exposed in the text (section 5.1.2).

	Sample	Mineral phase	Weight (g)	$^{4}He\ 10^{-13}$ (mol/g)	$^{20}Ne\ 10^{-15}$ (mol/g)	$^{40}Ar\ 10^{-12}$ (mol/g)	Rc/Ra	$^{4}He/^{20}Ne$	Err +/-	$^{40}Ar/^{36}Ar$	Err (%)	$^{4}He/^{40}Ar^{*}$
PERIDOTITES	XIH-1	Ol	3,0	1,2	5,6	1,4	7,0	211,9	0,19	314,8	0,05	1,3
			1,7	0,7	0,4	1,5	7,0	180,2	0,25	312,2	0,05	0,9
		Opx	2,2	4,2	0,7	2,2	7,0	637,9	0,11	342,7	0,06	1,4
			1,4	3,4	0,5	2,0	7,0	685,3	0,12	357,1	0,07	1,0
		Cpx	1,6	4,2	0,3	1,9	7,0	1236,5	0,13	445,7	0,07	0,7
			1,0	4,3	0,4	1,3	7,0	1034,8	0,10	414,9	0,06	1,1
	XIH-2	Ol	3,2	2,1	0,3	1,1	7,1	596,6	0,11	323,4	0,03	2,2
			3,3	2,1	0,3	0,2	7,1	762,5	0,08	513,7	0,02	2,6
		Opx	2,0	10,0	2,8	1,1	7,2	359,2	0,06	479,6	0,04	2,3
			1,6	5,9	6,5	1,0	7,3	90,7	0,07	461,8	0,05	1,7
			1,7	11,4	3,7	1,9	7,2	310,3	0,06	611,1	0,02	1,1
			0,7	10,6	2,2	3,6	7,2	489,2	0,07	804,8	0,27	0,5
	XIH-3	Ol	2,0	66,6	3,3	2,7	7,2	2033,0	0,06	426,8	0,03	8,2
			1,9	45,4	2,2	2,3	7,2	2036,1	0,06	414,1	0,07	6,9
		Opx	2,1	168,6	7,5	5,7	7,2	2245,8	0,06	502,1	0,05	7,2
			1,2	102,7	4,2	4,1	7,2	2453,8	0,06	553,5	0,06	5,3
		Cpx	1,1	263,0	5,5	6,6	7,4	4739,9	0,05	716,4	0,04	6,7
			0,7	188,5	5,1	4,3	7,4	3668,6	0,05	641,8	0,05	8,1
PYROXENITES	XIP-4	Cpx	0,8	302,1	35,4	25,6	7,3	853,9	0,06	620,1	0,10	2,3
			0,6	337,3	14,7	13,6	7,3	2294,1	0,05	900,9	0,04	3,7
	XIH-14	Cpx	0,5	13,9	22,7	2,4	7,6	61,4	0,10	315,9	0,03	8,8
			0,5	30,4	8,4	1,6	7,6	360,8	0,10	338,3	0,07	15,4
			0,4	11,5	6,3	2,7	7,4	183,0	0,11	314,9	0,42	6,8
			0,6	10,5	3,9	0,8	7,2	269,7	0,10	342,7	0,07	9,0
			0,6	5,1	0,3	0,8	7,1	1833,5	0,13	550,4	0,04	1,3
	XIC-26	Cpx	0,5	116,2	107,9	32,3	7,4	107,7	0,10	323,3	0,07	4,2
			0,2	83,6	6,2	6,9	7,3	1342,8	0,05	649,2	0,27	2,2
	XIP-28	Cpx	0,5	170,4	4,7	3,7	7,4	3660,9	0,06	554,2	0,04	9,8
			0,3	136,2	5,3	3,9	7,4	2580,4	0,06	477,1	0,04	9,1
	XIP-17	Cpx	0,3	45,8	9,3	4,5	7,4	490,3	0,08	431,4	0,04	3,2
			0,5	88,8	9,8	20,7	7,4	904,1	0,05	938,6	0,02	0,6
			0,5	81,4	13,0	23,9	7,3	624,8	0,05	556,6	0,04	0,7
AIR								0,3		295,5		

Table 11- Noble gases analyses of mineral phases (olivines and clinopyroxenes) from peridotitic and pyroxenitic Hyblean xenoliths.

5.1.2Noble gases as geochemical tracers of processes

In order to account for the observed variations of Rc/Ra and $^{4}He/^{40}Ar^{*}$ ratios, we need to consider the main processes, both post-eruptive and mantle-related, that can affect the noble-gas signature.

Post-eruptive processes

Posteruptive processes that could affect the variability of $^{3}He/^{4}He$ ratios in FI are cosmogenic ^{3}He production and radiogenic ^{4}He. Samples were collected from surfaces in rapid erosions, and the XIH1 and XIH3 samples were from road cuts, which should have made massive ingrowth of cosmogenic helium highly unlikely. In principle, the crushing procedure should release only gas retained in the bubbles and not matrix-sited components such as posteruptive ^{3}He and ^{4}He, further preventing both cosmogenic and radiogenic contributions implanted in the crystal matrix. Also, our data on peridotites display $^{3}He/^{4}He$ values (7.0–7.4 Ra) that overlap those of Sapienza et al. (2005) (7.0–7.6 Ra) for similar samples, despite us using a single-step crushing while Sapienza et al. (2005) used prolonged crushing (strokes for 2.5 minutes). It is reasonable to assume that if the samples were rich in a postmagmatic component that could be released by crushing, very different crushing techniques should give different results.

In addition, considering that the two principal parameters that control the posteruptive production of ^{3}He and ^{4}He (age of the sample and exposure at the surface) are similar for pyroxenites and peridotites, and that for the same He concentration the $^{3}He/^{4}He$ ratio is in most cases higher for pyroxenites than for peridotites (**Fig 5.4**), we attribute this isotopic difference to genetic processes rather than to posteruptive processes.

Therefore, even if we cannot definitely exclude slightly alteration of the original $^{3}He/^{4}He$ ratio of individual samples by posteruptive processes, the mean difference between peridotites and pyroxenites should be largely attributable to mantle processes.

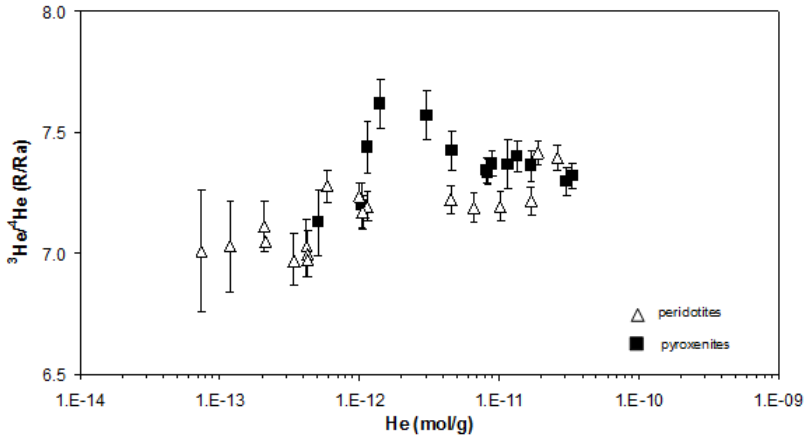

Fig 5.4 - $^3He/^4He$ (expressed as R/Ra) ratio vs He concentration in the investigated samples.

Mantle processes

In their study of worldwide mantle xenoliths, Yamamoto et al. (2009) observed that the $^4He/^{40}Ar^*$ ratio ranges from a typical mantle value of 1–5 (Graham, 2002; Ozima and Podosek, 1983) down to 0.1, coupled to a decrease in $^3He/^4He$ from 7 to 3 Ra. This behaviour was attributed to kinetic fractionation due to different noble-gases diffusivities through the mantle mineral assemblage, towards magma channels permeating the mantle itself. Because of their high incompatibility, noble gases would preferentially be partitioned in the magma relatively to mantle minerals with the net result to diffuse to magma channels. Under such conditions, the different diffusivities of ^3He, ^4He, and ^{40}Ar would induce a kinetic fractionation of these isotopes, and so the $^3He/^4He$ and $^4He/^{40}Ar^*$ ratios would decrease in the mantle source, which also would result depleted in noble gases. Following the approach of Yamamoto et al. (2009), we calculated how the noble-gas ratios should vary as a result of the diffusive fractionation (see Yamamoto et al., 2009, for further details on boundary conditions). The process would produce a dramatic decrease in Rc/Ra compared to that of $^4He/^{40}Ar^*$, showing a conflicting behaviour with respect to the trend observed in the data set (**Fig 5.3**).

With the aim to develope a suitable model to fit our data, we recall that magma degassing induces large changes in the $^4He/^{40}Ar^*$ ratio as a consequence of the different solubilities of noble gases in silicate melts (e.g., Burnard, 2004; Moreira and Sarda, 2000; Paonita and Martelli, 2006, 2007, and references therein). As magma ascends into the mantle as a consequence of depressurization, the noble gases leave the magma in proportion to their solubilities.

Specifically, due to the solubility of He being higher than that of Ar (e.g., Iacono Marziano et al., 2010; Nuccio and Paonita, 2000), the degassing process would increase the $^4He/^{40}Ar^*$ ratio of the residual magma. Based on the equilibrium degassing calculations of Paonita and Martelli (2007)

for a typical basalt raising from upper mantle and exsolving CO_2-dominated fluids, the first gas in vesicles that separate from a melt with $^4He/^{40}Ar \approx 3$ have a $^4He/^{40}Ar$ ratio of ~0.2 (see **Fig 5.5**). This ratio would increase as the magma ascends. FI entrapped at different pressures in the forming minerals can hence record $^4He/^{40}Ar^*$ ratios reflecting variable extents of degassing. By assuming an open-system degassing, a hypothetical pressure decrease from ~0.9 to 0.7 GPa—which is within the range of the expected depths of the investigated products (27–35 km; Sapienza et al., 2005)—is readily able to explain the observed $^4He/^{40}Ar^*$ variations (**Fig 5.5**).

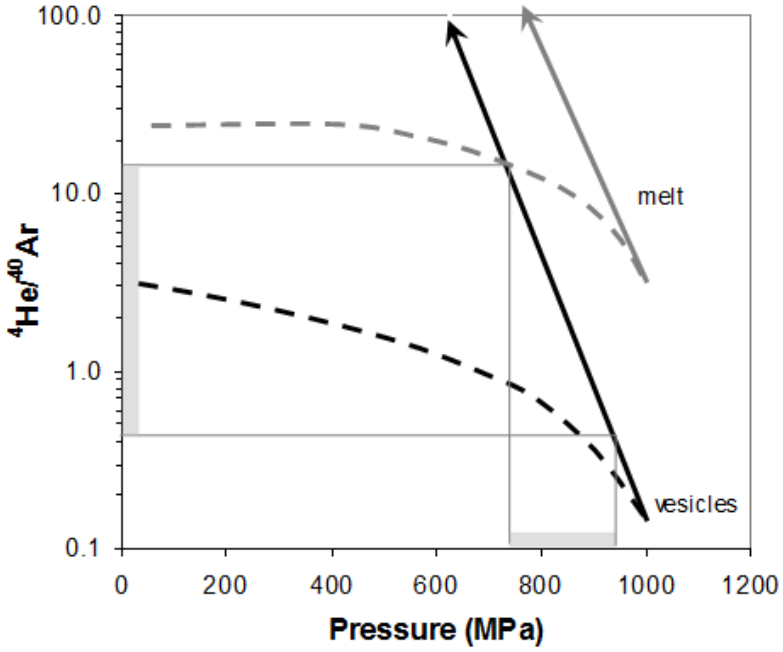

Fig 5.5 - Variations of $^4He/^{40}Ar^*$ ratio in melt (gray curves) and vesicles (black curve) during closed (dashed curve) and open (continuous curve) system degassing due to the decompressive ascent of magma. The shaded areas show the variation range of the $^4He/^{40}Ar^*$ ratio for the vesicles during a hypothetical magmatic depressurization from ~900 to 700 MPa (see the text for details). The equilibrium degassing model and volatile solubilities were the same as reported by Paonita and Martelli (2007) for a basalt melt at 1200°C. The initial conditions were H_2O and CO_2 contents of 0.3 wt% and 1 wt%, respectively, and an initial He/Ar* ratio of 3, in accordance with a pristine basaltic magma from the upper mantle (Paonita and Martelli, 2007).

Paonita and Martelli (2007) simulated a slow CO_2-dominated bubble growth, insering different diffusivities for the two He isotopes ($D_{3He} \approx \sqrt{4/3}\ D_{4He}$) and observed any kinetic fractionation between melt and vescicles for the examined noble gases as the much higher diffusivity of He relative to that CO_2 preserves the vapour-melt equilibrium of the former during the process. On the basis of these results we can be excluded a kinetic fractionation of ^3He and ^4He

during magma degassing of CO_2-dominated fluids (like our FI) and hence a further process must occur in conjunction with degassing to explain the measured $^3He/^4He$ variations. Starting from the mentioned petrologic and geochemical evidence, we propose that the He-isotope variability results from the heterogeneous mantle characteristics, where two local endmembers having different Rc/Ra values can be identified: (1) the peridotitic domain having R/Ra ≈ 7 and (2) the pyroxenitic domain with R/Ra ≥ 7.6.

In this regard, it is opportune to remember that the values of peridotites are closer to those of a HIMU-type mantle source (R/Ra = 5–7; Hanyu and Kaneoka, 1998; Moreira and Kurz, 2001), while those of pyroxenites approach those of a DM-type source (R/Ra = 8±1; Allègre et al., 1995). Accordingly, the deep high-Rc/Ra pyroxenite melt decompresses during ascent, reaching the low-Rc/Ra peridotitic levels. Open-system degassing can easily increase the $^4He/^{40}Ar$ ratios of the pyroxenite from values starting at around 0.4, such as for an early vapor separated from melt having typical mantle production ratio (see above), up to 15 or even more. The subsequent mixing process would occur between the high-Rc/Ra pyroxenite having variable $^4He/^{40}Ar$ ratios and a low-Rc/Ra peridotitic mantle with $^4He/^{40}Ar$ = 0.4–1.0. This range, which is slightly lower than the typical produced ratios of 1–5 (Ozima and Podosek, 1983), could result from the extraction of liquids produced by partial melting of the primordial peridotite. In fact, due to the incompatibility being higher for He than for Ar ($D_{He} = 1.17 \times 10^{-4}$ versus $D_{Ar} = 1.10 \times 10^{-3}$; Heber et al., 2007), ~1% of melting would account for the required decrease in He/Ar in the residual peridotite. This would also confirm the depleted character of the Hyblean peridotite, as already proposed by other researchers (Sapienza and Scribano, 2000). **Fig. 5.3** sketches the process using a set of two-endmember mixing curves between a fixed term and other endmembers with different $^4He/^{40}Ar$ ratios. The grid clearly shows that the described process may easily explain the complete data set.

In a previous study of Hyblean peridotitic xenoliths, Sapienza et al. (2005) had already observed a variability of R/Ra (in the range 7.3±0.3), although they did not investigate pyroxenitic xenoliths, and they proposed a deep metasomatizing source. Based on our results, the Hyblean pyroxenites would therefore represent a metasomatizing agent (having R/Ra ≈ 7.6) that is located in a deeper portion of the local lithospheric mantle, while the peridotites would correspond to a shallower layer (having R/Ra ≈ 7) that was occasionally injected by primitive mantle melts (cooled in depth as pyroxenites) ascending from depth (Perinelli et al., 2008; Sapienza and Scribano, 2000; Scribano et al., 2008). This would result in the shallower portion of the Hyblean mantle being partially or totally refertilized by these metasomatizing melts.

It is noteworthy that the measured $^3He/^4He$ values of the Hyblean xenoliths (7.0–7.6 Ra) were slightly but distinguishably higher than those measured in all other mantle xenoliths from

Europe and North-Africa (5.6–7.0 Ra; Beccaluva et al., 2007, 2008; Dunai and Baur, 1995; Gautheron et al., 2005; Martelli et al., 2011). Furthermore, such values are the highest measured in recent basaltic lavas of Italian Plio-Quaternary volcanism (Martelli et al., 2008, and references therein; Marty et al., 1994), with the notable exception of free gases sampled from thermal springs of Pantelleria Island reaching similar values (Parello et al., 2000).

5.1.3 Evidences of mantle metasomatism by coupling noble gases and trace elements data

The geochemical investigations on Hyblean xenoliths carried out in this study suggest the existence of a vertical heterogeneity of Hyblean mantle, being characterized by a deep layer supplying the pyroxenitic melts that partially metasomatize a peridotitic shallower portion. We subsequently investigated the quantitative relationships between trace elements and $^{3}He/^{4}He$ data.

Fig 5.6 shows average R/Ra versus Sm and Nd concentrations of single nodules. Pyroxenites and peridotites defined two distinct endmembers of Hyblean mantle, where the highest R/Ra data were found in the pyroxenites that also showed the highest Sm and Nd concentrations, while the same correspondence at the lowest values was observed in the peridotites. The two mantle layers, characterized by extreme Sm, Nd, and R/Ra values of the complete data set, would be (1) the peridotitic one, with an average R/Ra ≈ 7, Sm ≈ 0.25 ppm, and Nd ≈ 0.1 ppm, and (2) the pyroxenitic one, characterized by an average R/Ra ≈ 7.4, Sm ≈ 3.5 ppm, and Nd ≈ 13 ppm.

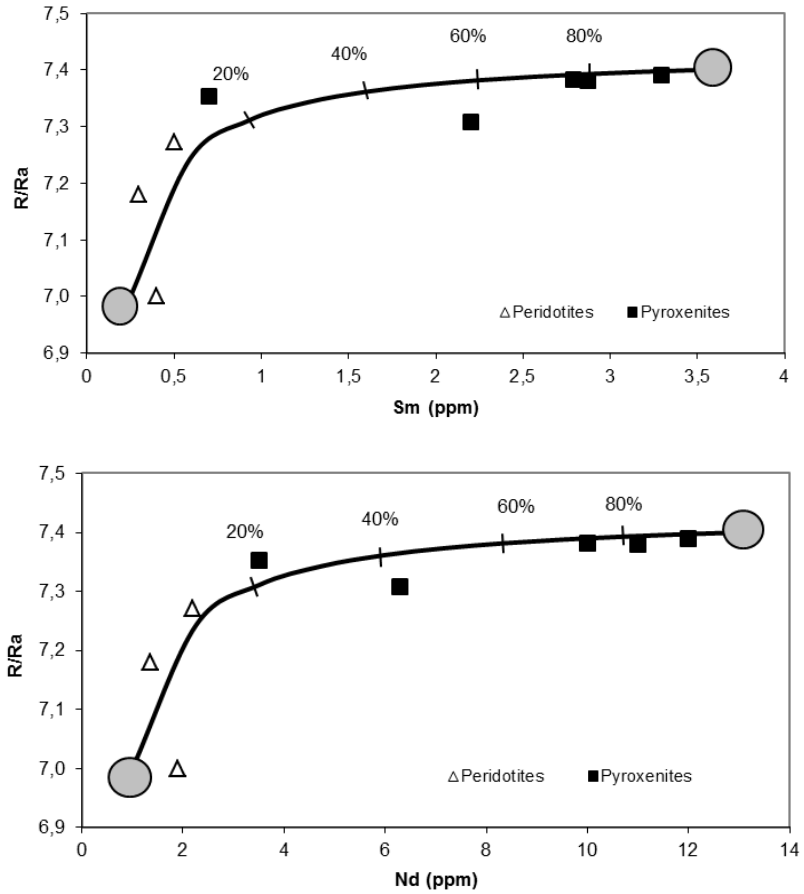

Fig 5.6 - Plot of $^{3}He/^{4}He$ (R/Ra) vs Sm (a) and Nd (b) concentrations of whole rock from Hyblean peridotites and pyroxenites. The curves describe a mixing trend between two hypothetical end-members associated respectively with peridotitic and pyroxenitic sources. Ticks indicate percentages of the pyroxenitic endmember. The He concentrations of the two endmembers, used to calculate the mixing path, were the highest measured in pyroxenites and the lowest in peridotites.

Different degrees of metasomatism were modeled assuming a mixing process between the two endmembers, as already observed for the noble gases and the REE data independently.

Inspection of **Fig 5.6** shows that the strongly convex shape of the resulting mixing curves is in a good agreement with our data, suggesting that the cryptic metasomatic process could potentially control both trace-element and noble-gas signatures. Furthermore, peridotites and pyroxenites represent two distinct domains of the same mantle with all of the intermediate terms.

Whereas Sm and Nd mix linearly, the large amount of He in pyroxenites makes the isotopic ratio of this volatile extremely sensitive to put into evidence even very small extents of metasomatism. In fact, a very low metasomatic contribution from pyroxenite (<2%) dramatically changes the isotope ratio of peridotite mantle although it do not practically modify the trace elements. On the other hand, the Nd and Sm-poor peridotites samples have suffered around 30% of cryptic mixing with pyroxenite, but they still exhibit unaffected He isotopic marker. Again, the scarcity of both He and incompatible trace elements accounts for a strongly depleted character of Hyblean peridotites, which probably also suffered extensive degassing during melt extraction. The He-isotope ratio gives some indications about the widely debated genesis of pyroxenites on a worldwide scale, with the two main groups of interpretations being (e.g., Bodinier and Godard, 2003; Downes, 2007) (1) crystal precipitation from deep-mantle magmas along narrow lithospheric conduits or (2) recycling and recrystallization of subducted components belonging to old oceanic crust in a convecting mantle. Our data indicate the high He-isotope ratio of Hyblean pyroxenites, which is close to the mean value of MORBs intended as samples of the convecting upper mantle (Graham, 2002). Our data are thus consistent with the Hyblean pyroxenites originating from the first of the two hypothesized mechanisms, while processes connected to recycled components by subducted slab should involve a lower He-isotope ratio due to time-integrated ^{4}He growth from U and Th radioactive decay.

5.1.4 Inferences from the heterogeneity of the Hyblean mantle

The geochemistry of Zr/Nb, Sr and Nd isotopes, and noble gases in our mantle xenoliths highlights that Hyblean peridotites and pyroxenites resemble well-known HIMU and DM mantle sources, respectively. Furthermore, the petrographic evidence (peridotitic nodules veined from pyroxenites) account for a deeper origin for the pyroxenites, so that the mantle layer having HIMU characteristics would be shallower than the DM-type one. Such inferences raise two main questions: (1) can a recycled component be associated with a peridotitic mantle and a DM be associated with a pyroxenitic mantle, and (2) what is the meaning of their peculiar vertical stratification?

With regard to the first question, Sobolev et al. (2008) showed that the enriched component is frequently linked to reaction pyroxenite (ie a pyroxenite derived by reaction of the surrounding peridotite with recycled crust), whereas the depleted component is likely to be derived from a peridotitic source, this being in contrast with our results. However, studying mantle xenoliths from the Canary Islands, Gurenko et al. (2009) suggested that a recycled mantle component is not necessarily linked to an eclogite-pyroxenite paragenesis. In fact, it could also exist in the form of peridotite whenever an old (>1 Ga) recycled component had sufficient time to be stirred back into the peridotitic matrix. The results of our study are thus consistent with the second hypothesis, and suggest that the mineralogical assemblage of recycled mantle component can range from pyroxenites, "hybrid melts", up to peridotites.

Concerning the inferred vertical stratification, our results contrast with the view that the Euro-Mediterranean HIMU is generated by upwelling of a deep plume (e.g., Hoernle et al., 1995). In fact, when linking the HIMU/FOZO signature to a mantle plume of recycled material, we would expect the HIMU to originate at deeper mantle levels than MORB (Rotolo et al., 2006). However, different models can support our inferred location of HIMU shallower than MORB: Scribano et al. (2008) assumed the presence of a serpentinite-hosted hydrothermal system in the Hyblean lithosphere as a result of tectonic uncovering and seafloor exposure of the uppermost mantle since middle Triassic. This hypothesis could account for the HIMU marker of peridotites through the hydrothermal addition of U to altered rocks, especially after serpentine formation (Michard and Albarède, 1985). The homogeneous isotope marker of He in olivines, orthopyroxenes, and clinopyroxenes of the peridotitic samples supports the radiogenic production of ^{4}He from serpentine veins and its uniform diffusion toward the three mineralogical phases. Since the serpentine veins were mainly found in microcracks within olivine or along grain boundaries, we expect the R/Ra ratios to be more radiogenic in olivines than in pyroxenes, in contrast with what we observed. This would also require migration of He from the lattice into FI, although we showed that this process seems to be of minor importance (see Section 5.1.2). The more primitive He-isotope composition of pyroxenites

would also imply either that the latter ones infiltrated the peridotitic matrix subsequent to the hydrothermal circulation causing the HIMU signature or that the analyzed pyroxenites sampled portions of pyroxenitic veins that were physically distant from the contact area with the surrounding peridotite, so as to avoid the main interaction with serpentinizing fluids.

Indeed, the most striking feature of the investigated HIMU signature is its widespread occurrence in several Euro-Mediterranean areas (Cebria and Wilson, 1995; Macera et al., 2003; Wilson and Downes, 1992; Wilson and Bianchini, 1999), so that any explanation should preferentially involve a regional scale. Lustrino and Wilson (2007) summarized some of the different models that support the presence of a Euro-Mediterranean HIMU mantle without invoking a mantle plume actively upwelling from a thermal boundary layer at the core–mantle boundary. The signature of recycled component may be simply inherited by the shallow upper mantle in the form of a metasomatized lithosphere or enriched asthenosphere, as suggested by the SUMA model (statistical upper mantle assemblage) (Meibom and Anderson, 2004). Based on this, Piromallo et al. (2008) explained the common HIMU-like character of erupted lavas in different tectonic environments of the Euro-Mediterranean region by proposing a sub-lithospheric dragging of the plume head located in the Canary–Cape Verde zone as a result of a north-to-eastward migration of the Eurasian and African plates away from the hot spot (see **Fig 5.7**) . This would have allowed a spreading of plume material in the shallow sub-lithospheric mantle so as to produce a geochemically anomalous (HIMU-like) level located above the depleted upper mantle. We therefore conclude that the somewhat anomalous mantle stratification that we have suggested here for Hyblean mantle can be explained within the framework of the above model.

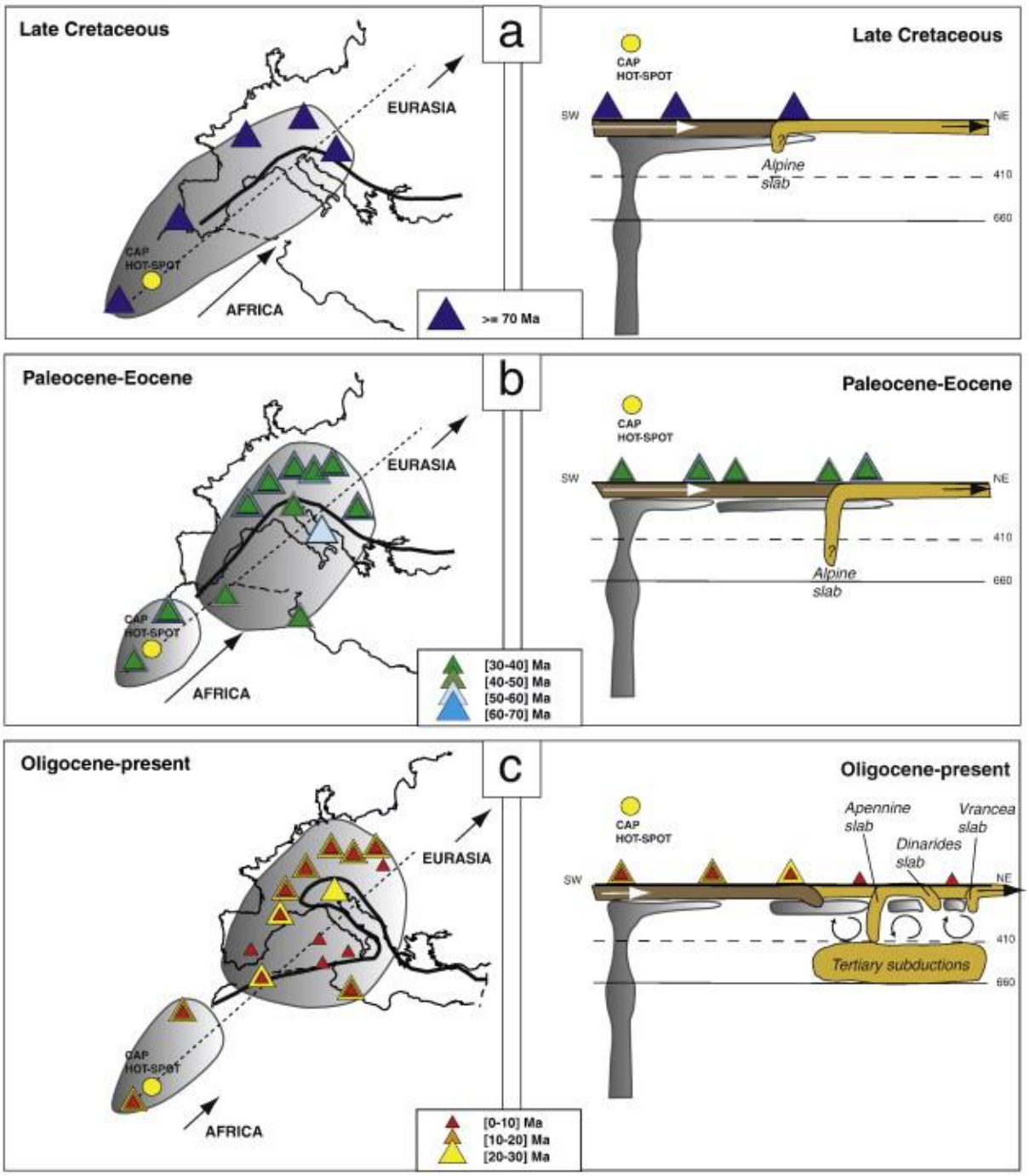

Fig 5.7 Highly idealized sketch, showing mechanism responsible for the common HIMU-like character of European alkaline lavas erupted enduring over about 100 million years in diverse tectonic environments. **Left-hand panels:** map views of Africa–Eurasia absolute motion in the hotspot reference, location of alkaline volcanic centers and extent of the contaminated region (grey area). CAP hot spot location (yellow dot) is fixed and generally refers to Canary–Cape Verde plume. The thick black lineament corresponds to the suture between the African and Eurasian plates. **Right-hand panels:** cross-section through a SW–NE trending profile; positions of the volcanic fields and subducted slabs are roughly projected along the section (From Piromallo et al., 2008).

5.2 Etna

5.2.1Chemical and isotopical composition of fluid inclusions

The concentrations of noble gases in the phenocrysts of the studied Etnean lavas are listed in **Table 12**. The He content varies from 2.97×10^{-13} to 2.18×10^{-12} mol/g respectively from FS to Spagnolo olivines and from 3.61×10^{-14} to 3.04×10^{-13} mol/g respectively from De Fiore to FS clinopyroxenes while the R/Ra ranges from 6.69 to 7.62 from Montagnola to Spagnolo olivines and from 4.87 to 6.59 from De Fiore to Spagnolo pyroxenes (**Fig 5.8**).

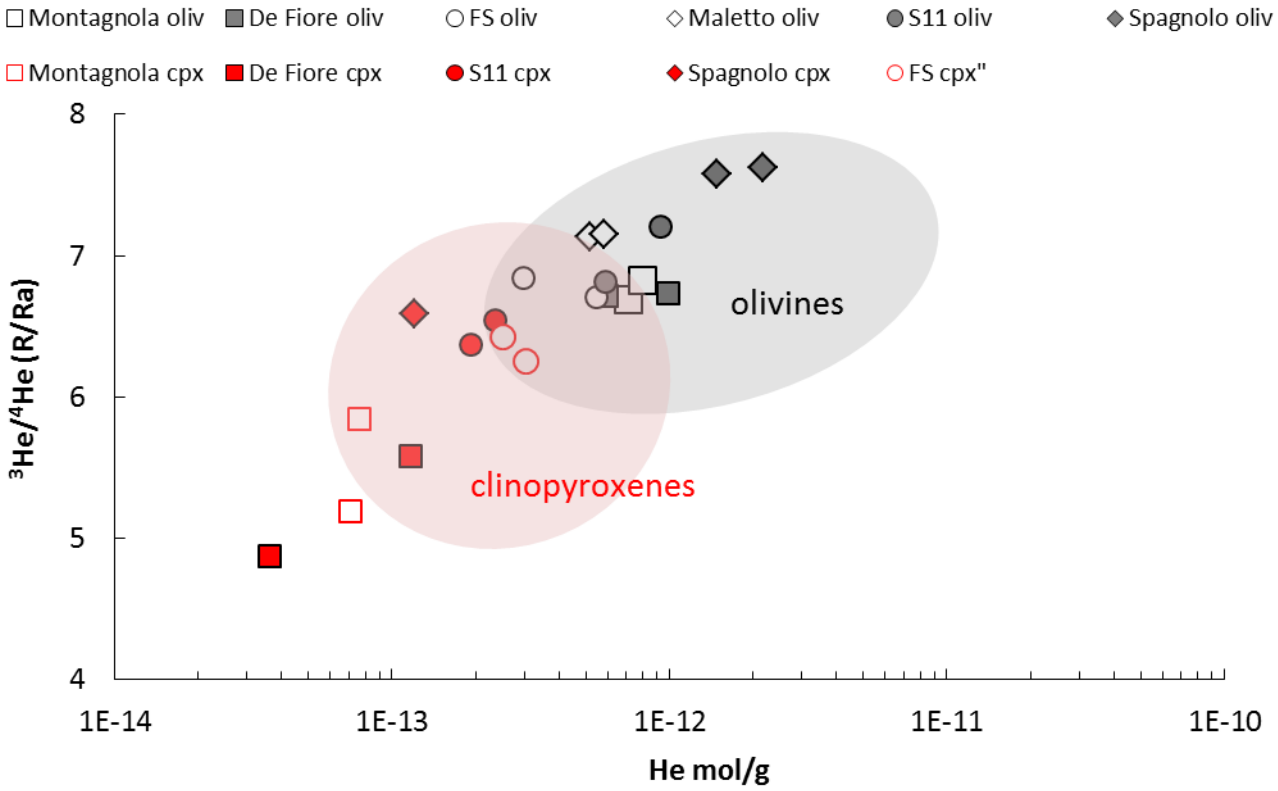

Fig 5.8 - Plot of $^{3}He/^{4}He$ (R/Ra) vs He abundances from olivine and pyroxene FI from Etnean primitive lavas. The red and gray shaded area are from Etnean clinopyroxenes and olivines, respectively taken from Marty et al., 1994 and Nuccio et al., 2008.

As underlined in the section 5.1.1 the FI can be contaminated by air, thereby affecting also the source signature of noble gases. In order to evaluate the air contribution in our samples, we plotted $^{4}He/^{20}Ne$ versus $^{40}Ar/^{36}Ar$ ratios, as shown in **Fig 5.9**.

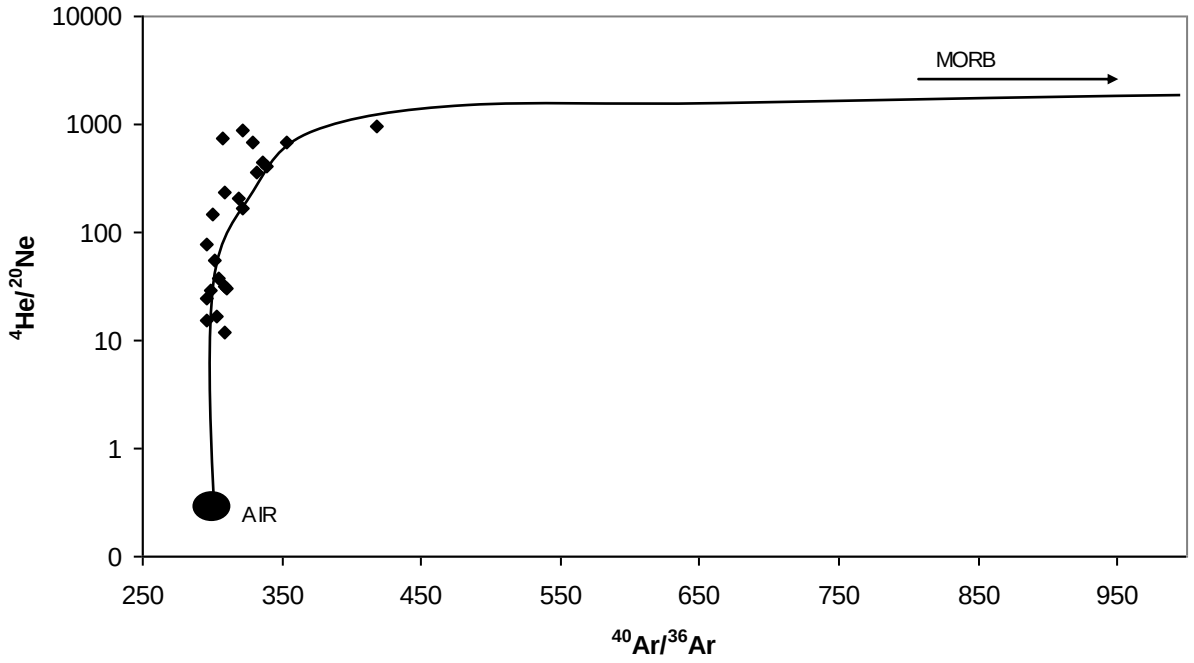

Fig 5.9 - Plot of $^{40}Ar/^{36}Ar$ vs $^{4}He/^{20}Ne$ ratios of olivine and pyroxene FI from Etnean primitive lavas. The curve defines a mixing trend between two end-member: 1) MORB having $^{4}He/^{20}Ne$ ~10000 (Marty et al., 1983), $^{40}Ar/^{36}Ar$ ~40000 (Graham et al., 2002) AIR having $^{4}He/^{20}Ne$ =0.318, $^{40}Ar/^{36}Ar$ =295.5.

The $^{4}He/^{20}Ne$ ratio varied between 12 and 950, while that of $^{40}Ar/^{36}Ar$ varied between 296 and 418. We observed that all of the samples fall on a computed curve of the binary mixing between an atmospheric end member and a hypothetical MORB source (Graham et al., 2002; Marty et al., 1983), thereby confirming atmospheric contamination of the gases released from FI (Fig 5.9; see caption for further details). Consideration similar to those made for the Hyblean samples in Sec 5.1.1, taking in account the Etnean peripheral gas emissions sampled by the Etna group of INGV-Pa ($^{40}Ar/^{36}Ar$ ratio values up to 1800), suggests that the low $^{40}Ar/^{36}Ar$ ratios of FI were not inherited from the mantle. Instead they were probably caused by air contamination that occurred after the entrapment of FIs.

Even in this case (see section 5.1.1), we subtracted the air contamination from the $^{3}He/^{4}He$ ratios using the formula of Giggenbach et al. (1993) and we report the corrected $^{3}He/^{4}He$ values as Rc/Ra values. The Rc /Ra ($^{3}He/^{4}He$) ratio varies from 7 to 7.6 from FS to Spagnolo olivines respectively and from 4.8 to 6.59 from De Fiore to Spagnolo clinopyroxenes respectively (Fig 5.8). In **Fig 5.8** we also report the data relative to olivine and clinopyroxene crystals from lavas (red and gray shaded areas in figure) covering the major episodes of Etna volcanism, from the pre-Etnean tholeiitic pillow lavas to the more recent alkali trachybasalts (Marty et al.,1994) and volcanics erupted during 2001-2005 (Nuccio et al., 2008). The **Fig 5.8** highlights an overlapping between our dataset and those of Marty et al. (1994) and Nuccio et al. (2008) so underlining a consistency in the

information. In detail a positive trend between He concentration and isotopic ratios is evident: the olivines result richer in He and with higher Rc/Ra ratios while the pyroxenes are poorest in He and show lower Rc/Ra ratios. Although this behaviour seems to characterize the Etnean samples, it is not a general result of FI investigations which also report products having higher noble gas amounts in pyroxenes (Martelli et al., 2004; Shaw et al., 2006).

5.2.2 Olivine-pyroxene disequilibria

The decoupling between isotopic values of olivine and pyroxene-hosted FI is an amply discussed argument by previous authors on lavas from Etna volcano (Marty et al.,1994; Nuccio et al., 2008) and in other FI from basaltic volcanoes (Hilton et al., 1995; Patterson et al., 1997; Shaw et al., 2006) and it is still matter of debate. In order to justify the different results for two different mineralogical phases, many authors (Marty et al. 1994; Hilton et al., 1995; Shaw et al., 2006) propose that the pyroxenes crystallize after the olivines or that the closure temperature (ie the T at which diffusive loss becomes negligible) of cpx is lower than for olivines, with the result that the former record the characteristics of a magma showing a more radiogenic isotopic ratio of helium.

The decrease of helium isotopic ratio could be caused by either magma aging (which imply a radiogenic ^{4}He production) or crustal contamination of a residual magma during storage in the magmatic reservoirs. Through radiogenic decay calculations starting from U and Th content in Etneas lavas, Marty et al. (1994) estimated exceedingly long time span (20-40 kyr) to be compatible with the much smaller refilling cycles of the Etnean magma reservoirs (<10 kyr; Condomines et al., 1982,1987), thus they preferred a decreasing of $^{3}He/^{4}He$ ratio due to addition of pre-eruptive radiogenic helium inclining for the crustal contamination hypothesis.

Nuccio et al., 2008 refuse also the crustal contamination possibility because both olivine and pyroxenes are early phases crystallizing from Etnean magmas (Clocchiatti et al., 2004; Corsaro et al., 2007; Armienti et al., 2007), so they should record no variations in the He isotopic characteristics of the magma. Alternatively, Nuccio et al. (2008), based on the model of Harrison et al. (2004), propose that the differences of He isotope ratio between olivines and pyroxenes mainly depend on the different crystal structure of two mineralogical phases. The packed structure of olivine crystals could reduce any secondary change, after crystallization so avoiding the diffusive kinetic fractionation of He from crystal and preserving the original magma signature (Craig and Lupton, 1976; Mamyrin and Tolstikhin, 1984; Ozima and Posodek, 1983; Martelli et al., 2004).

Regardless of the model proposed to explain the He isotopic olivine-pyroxene disequilibrium, it is evident that the pyroxene phenocrysts did not preserve the primordial mantle

signatures. In order to carry out our study on the Etnean mantle source, we will focus only on the olivine minerals so to get information strictly related to original magma characteristics.

5.2.3 He isotope variation in olivine phenocrysts

Focusing on the olivine phenocrysts of investigated Etnean lavas, the decreasing $^{3}He/^{4}He$ from the oldest Spagnolo and Maletto products to the most recent FS and after Montagnola, De Fiore, 2001 and 2002-2003 result in a difference of 1 Ra between the above volcanics (**Fig 5.10**). Given the different age between the samples, we question if the isotopic He marker of Etnean mantle source changed during time.

Although olivines from 2001 Etnean eruption show values of R/Ra ≈6.9 (Nuccio et al., 2008), consistent with the youngest lavas analyzed in this work, the gas emissions sampled at P39 site by Caracausi et al. (2003a) during the same eruption, reached a R/Ra as high as 7.6. This is interpreted as related to volatile-rich magma recharge from depth into the Etnean shallow plumbing system and represents a strong evidence that the helium isotopic marker of Etnean mantle today is at least 7.6 Ra. Then, the variation trend of R/Ra from Spagnolo to the recent lavas is likely to be due to secondary processes and it is not correlated to mantle source variations.

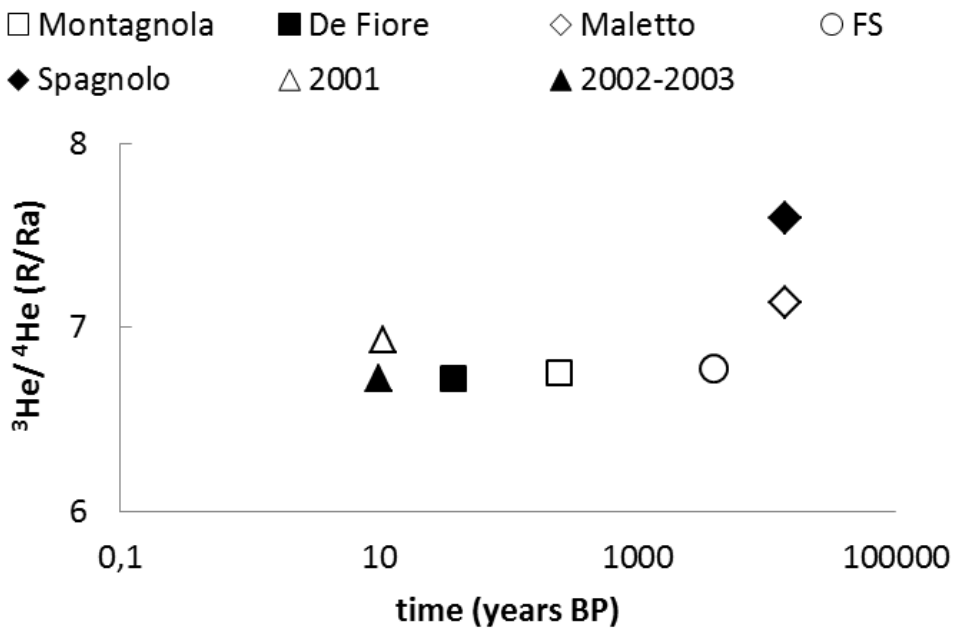

Fig 5.10 - Plot of $^{3}He/^{4}He$ (R/Ra) vs time for Etnean primitive products. R/Ra average of 2001 and 2002-2003 eruptions from Nuccio et al., 2008. Time estimates for the historical Etnean products from Condomines et al., 1982, Kamenetsky and Clocchiatti, 1996, Coltelli et al., 2005 and Kamenetsky et al., 2007.

Post-eruptive processes

As mentioned in the previous section the gaseous manifestations sampled by Caracausi et al., 2003a during the 2001 eruption in the Eastern and Southern parts of Etna volcano highlighted for the Etnean mantle source an He isotopic marker at least of 7.6, althought the He isotopic from LV2001 lava olivine fluid inclusions (Nuccio et al., 2008) exhibited a lower R/Ra (≈6.9). In this context, the $^{3}He/^{4}He$ values lower than 7.6 measured in several Etnean lavas investigated in this work, both recent (De Fiore, Montagnola) and historical (FS, S11 and Maletto), are not indicative of a mantle source. Between the studied Etnean products only Spagnolo showed $^{3}He/^{4}He$ ratios compatible with the 2001 gases emissions. Then there are two different possibility to interpret the higher He isotopic ratios of Spagnolo: 1) it represents the primordial value of mantle source or 2) it is the result of an increasing of $^{3}He/^{4}He$ due to ^{3}He cosmogenic production.

Obviously the variable amount of cosmogenic ^{3}He in the sample and then the higher $^{3}He/^{4}He$ ratio are stricltly connected with the exposition times of the volcanic product to the surface.

As Mt Maletto and FS (<14 ky and 4 ky respectively) are almost coeval with Mt Spagnolo (<14 ky), if cosmogenic processes influenced the R/Ra of Mt Spagnolo increasing it until 7.6 Ra then also the helium isotopic ratio of FS and Maletto would be the same. As Maletto and FS present R/Ra lower than 7.6 (7.1 and 6.8 respectively), then we can deduce that Mt Spagnolo exhibits $^{3}He/^{4}He$ mantle signature.

Established that the isotopic helium of M. Spagnolo reflects value near to that of mantle source how can we interpret the lower $^{3}He/^{4}He$ from all the other examinated Etnean products? A process possible to lower the He isotopic ratio below 7.6 is the post-eruptive radiogenic production of ^{4}He but considerations similar to those made for the cosmogenic process led us to exclude also this together with all trials strictly connected with the time.

Pre-eruptive processes

Processes capable to lower R/Ra of the Etnean reservoir are matter of debate. If we constrain the refilling time to 10 ky on the basis of the results of Condomines et al. (1982,1987), and we assume the value of 10^{-11} mol/g He in magma, as estimated by Marty et al. (1994), then magma aging would not be able to lower R/Ra by about 0.6 units. On the other hand, Nuccio et al (2008) excluded crustal contamination in lowering R/Ra by 0.5 units within a few years-long time period, based on diffusivity of He in melts (5×10^{-5} cm^2/s, Lux, 1987). Nevertheless, similar calculations display that He could diffuse by several tenths of meters into the magma body in 10 ky and, in this condition, advective dynamics of magma could also mix the whole reservoir. Therefore, crustal contamination could be able to act in long time so as to significantly lower the He isotope marker of the reservoir.

It is not the aim of this study to deeply investigate this aspect. Despite the true involved processes, what is important is that, based on our results, a resident magma having 6.8 R/Ra probably characterizes most of the crustal reservoirs below Etna, while the mantle source supplies melts with R/Ra values of 7.6 or even more. This means that a partial contamination of the magma, during its raise through the magmatic reservoir could have generated the low helium isotopic ratios of the recent Etnean lavas. In this framework, rate of ascent, time of storage and mixing would be key parameters in controlling the R/Ra values of an erupted lava. Considering that the helium isotopic data from FI entrapped in olivines of Etnean products have generally R/Ra $\leq$7 (Marty et al., 1994; Nuccio et al., 2008), then it is likely that Spagnolo, having R/Ra of 7.6, was characterized by very quick rise which has prevented a long storage and mixing in the magmatic reservoir and consequently a significant contamination.

5.2.4 Influence of a metasomatic component in the Etnean lava genesis highlighted from noble gases and trace elements geochemistry

In section 5.1.3, the coupling of $^{3}He/^{4}He$ and some trace element abundances of Hyblean xenoliths that allowed us to identify both: 1) a mantle heterogeneity, represented by a peridotitic and a pyroxenitic domain respectively and 2) metasomatic events, characterized by pyroxenitic melts intruding the peridotitic matrix. Also, we were able to locate by trace elements geochemistry the mantle source of the Etnean lavas along a mixing curve between Hyblean-like mantle sources having pyroxenitic and peridotitic affinity, respectively.

At this stage, it is full of interest to confirm the relation between the Hyblean and Etnean mantle, in the case of He isotopes. It also allows to investigate if and eventually how much a metasomatic pyroxenitic component is involved in the melting of the Etnean peridotitic mantle, as the large amount of He in pyroxenites makes this element very sensitive to put into evidence the metasomatism. With this aim, we reported the values of the estimated primordial mantle source for the Etnean lavas in a $^{3}He/^{4}He$ vs Nd plot (**Fig 5.11**).

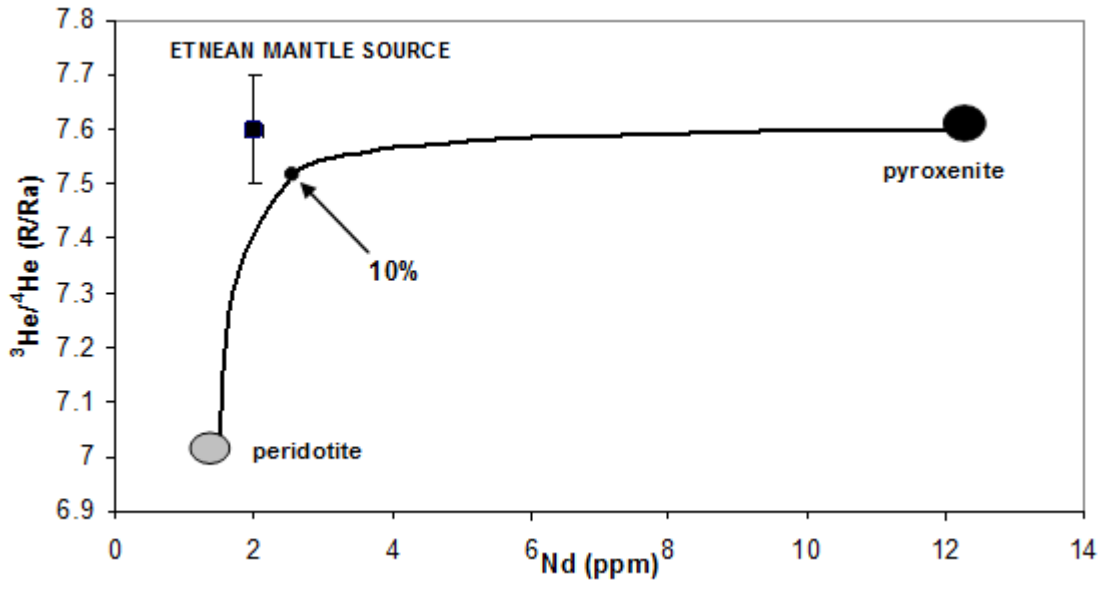

Fig 5.11- Plot of $^{3}He/^{4}He$ (R/Ra) vs Nd abundances from Etnean calculated mantle source (see text for details). The curve describes a mixing trend between two hypothetical end-members associated respectively with a peridotitic (R/Ra=7; Nd=1.5 ppm) and a pyroxenitic (R/Ra=7.6; Nd=12ppm) source. The point indicates the percentage of pyroxenitic end member. The He concentrations of the two end members, used to calculate the mixing path, are the highest measured in pyroxenites and the lowest in peridotites.

The Nd elemental concentration for the original source was calculated with the same procedure used for the others investigated trace elements (see section 4.2.2), while the $^{3}He/^{4}He$ values considered representative of the Etnean mantle source is that from Spagnolo FI, as coherent with the Etnean gases emissions of 2001. In the same figure, the Etna source can be compared to fields of Hyblean peridotite and pyroxenite, as well as their peculiar curve of mixing. It is remarkable that, due to the strong convexity of the mixing curve, the Etna source is compatible with the mixing process. In fact, the low Nd abundance (~ 2 ppm), typical of a peridotitic source, associated to the high R/Ra values (R/Ra=7.6), typical of a pyroxenitic mantle, highlights the contribution of pyroxenitic veins in the genesis of Etnean lavas from a mainly peridotitic mantle. Indeed, asunderlined previously, the pyroxenitic metasomatic events gives a strong fingerprint to the helium isotopic marker but increase only slightly the concentration of trace element so retaining values closer to peridotite. The mixing curve between the peridotitic and the pyroxenitic end-member allows to evaluate the amount of pyroxenitic melt involved in the Etnean lava genesis that resulted to be ~10% (**Fig 5.11**). The above percentage is coherent with the evaluations from trace element geochemistry where we estimated a pyroxenitic contribution in the Etnean mantle source of ~ 10-20% (see section 4.2.2).

The **Fig 5.12** shows a mixing curve between a peridotitic and pyroxenic end-member, characterized respectively by $^{3}He/^{4}He$=7Ra, Zr/Nb=4 and by $^{3}He/^{4}He$ = 7.6 Ra, Zr/Nb=56. The strongly convex shape of the resulting mixing curves, still coherent with that showed in fig 5.11, corroborate both: 1) the similar behaviour of trace elements to metasomatism events and 2) the pyroxenitic percentage (10-20%) involved into peridotitic mantle melting.

An heterogeneous mantle source for Mt Etna volcano was already hypothesized by Viccaro et al., 2008 in order to explain the variability of the trace element and isotopic composition from some Etnean historic (pre-1971) and recent (post-1971) volcanic rocks. The authors proposed for the genesis and evolution of the studied magmas a melting of a depleted mantle re-fertilized by plume – related silicate melt/fluids, inheriting a signature likely derived from ancient hydrotermally altered oceanic crust stored for long time in the mantle.

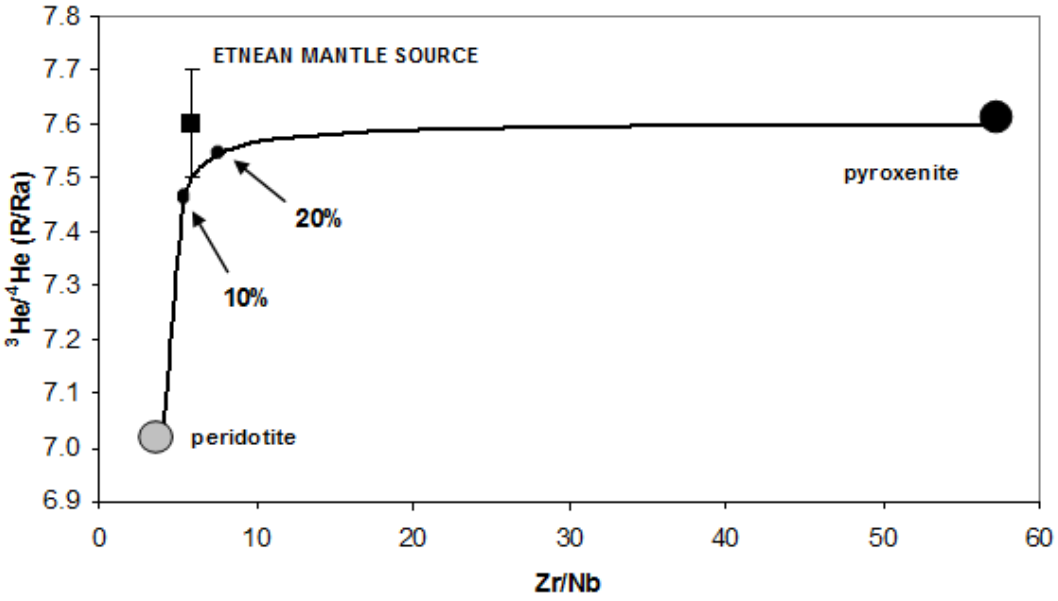

Fig 5.12- Plot of $^3He/^4He$ (R/Ra) vs Zr/Nb ratio from Etnean calculated mantle source (see text for details). The ticks indicate the percentages of pyroxenitic end member. The curves describe a mixing trend between two hypothetical end-members associated respectively with a peridotitic (R/Ra=7; Zr/Nb=4 ppm) and a pyroxenitic (R/Ra=7.6; Zr/Nb=56ppm) source. The He concentrations of the two end members, used to calculate the mixing path, are the highest measured in FI of pyroxenites and the lowest in FI of peridotites, while the Zr and Nb concentrations correspond to highest and lowest Zr/Nb ratios measured in pyroxenites and peridotites respectively.

Sample	Mineral	$^{4}He\ 10^{-13}$ (mol/g)	$^{20}Ne\ 10^{-15}$	$^{40}Ar\ 10^{-13}$	Rc/Ra	Err totale +/-	$^{40}Ar/^{36}Ar$	Errore (%)
De Fiore	Oliv	9,87	1,44	6,13	6,73	0,06	328,60	0,27
		5,92	2,56	3,98	6,71	0,13	308,51	0,10
	Cpx	1,16	3,03	18,46	5,58	0,16	304,23	0,02
		0,36	2,29		4,87	0,64		
Montagnola	Oliv	7,1	1,97	2,33	6,69	0,10	331,65	0,02
		8,03	1,82	4,02	6,82	0,14	335,81	0,29
	Cpx	0,708	4,23	13,56	5,19	0,20	303,03	0,02
		0,76	2,65	19,08	5,84	0,39	298,80	0,05
Spagnolo	Oliv	21,8	2,29	8,13	7,62	0,10	417,89	0,10
		14,9	2,2	8,84	7,57	0,09	354,00	0,10
	Cpx	1,2	3,87	7,99	6,59	0,45	308,91	0,10
		0,49	3,28	5,4	4,50	0,28	295,96	0,10
Maletto	Oliv	5,16	0,58	4,36	7,13	0,13	321,41	0,10
		5,82	1,45	2,58	7,15	0,16	339,00	0,10
FS	Oliv	5,44	2,6	4,99	6,71	0,13	319,07	0,29
		2,97	12,4	108,11	6,84	0,17	296,11	0,10
	Cpx	3,04	3,96	16,47	6,25	0,16	295,84	0,29
		2,5	4,5	5,81	6,43	0,16	302,27	0,10
S11	Oliv	5,9	27,1	87,97	6,81	0,14		
		9,29	1,23	1,94	7,21	0,14	307,97	0,10
	Cpx	2,37	7,88	1,37	6,55	0,13	309,67	0,02
		1,92	1,28	2,5	6,37	0,19	300,61	0,10

Table 12- Noble gases analyses of mineral phases from Etnean tephra and lavas.

6. Conclusions

In order to investigate the characteristics of the mantle source in Eastern Sicily, a comprehensive geochemical study of Etnean and Hyblean products was performed, with the principal aim to understand similarities among the mantle sources feeding the Plio-Quaternary volcanic provinces.

Mantle-derived ultramafic xenoliths, consisting of peridotites and pyroxenites nodules found into some Miocenic age diatremes, were selected to better characterize the lithospheric mantle below the Hyblean area. New data of major and trace elements coupled to Sr-Nd isotopes are here provided and are compared with those available from previous studies. These geochemical data were integrated with noble gases isotopic data from fluid inclusions hosted in mantle xenoliths.

Very primitive pyroclastic fall-deposits and eccentric lavas with a chemical composition variable from basalt to trachybasalt were selected to characterize the Etnean mantle source. Noble gases analyses of fluid inclusions in olivine and clinopyroxene phenocrysts was coupled to a more general study on whole rock major and trace elements , and implemented with Sr-Nd isotopic data derived from previous studies.

The integration of these data led us to the following conclusions:

1) The mantle below the Hyblean area is heterogeneous, featured by a shallower peridotitic layer with more enriched geochemical fingerprint (R/Ra of ~7, $^{143}Nd/^{144}Nd$ of ~0.5129 and Zr/Nb of ~ 4) with respect to a deeper pyroxenitic layer characterized by a more primitive character (R/Ra up to 7.6, $^{143}Nd/^{144}Nd$ of ~0.5130 and Zr/Nb of ~30). Peridotites and pyroxenites seem to display HIMU and DM affinities, respectively.

Our interpretation is that metasomatic processes interested the Hyblean lithosphere and the deep-seated pyroxenites (former primitive mantle melts) were recognized to represent the metasomatizing agent. During their ascent these primitive melts variably permeated the peridotitic mantle at different levels, producing a variable degree of refertilization.

2) The metasomatic processes affected distributions of both trace elements and noble gases. Previous studies of mantle xenoliths hypothesized a decoupling of noble gases in fluid inclusions with respect to radiogenic isotopes and trace elements. As we show here different geochemical tracers can display very different sensitivity to the effects of metasomatic mixing between two end-

members, hence this should be carefully considered when hypothesizing decoupling between noble gas and trace element geochemistry.

3) Primitive magmas from Etna originate from different melting degree of a mantle source very similar to the Hyblean one. The geochemical characteristics of the Etnean mantle source suggest a strict relation with the Hyblean mantle, supporting the hypothesis of an heterogeneous and metasomatized lithosphere common to both areas. Indeed, the geochemistry of trace elements locates this source on the mixing zone between the peridotite and pyroxenite groups, thus testifying a simultaneous contribution of two components in the genesis of the investigated lavas. Also the Nd isotopes underline a certain relation with both the mantle levels while the helium isotopes, showing a more sensitivity to effect of metasomatic mixing, exhibit typical pyroxenitic values.

4) During their storage in the magmatic reservoir and their rise to surface, these products are interested by a different level of crystallization and are contaminated variably by fluids from crustal component. This results in more radiogenic He and Sr-Nd isotopic composition .

ACKNOWLEDGMENTS

I would to thank my tutor the Professor Silvio Rotolo for his useful teachings and for his constructive suggestions.
A particular thank is for my co-tutor Dr Antonio Paonita for his patience and useful teachings, for all the time he spent for my research project but above all for the efforts he made to transmit me a scientific method to approach the research which represent the most precious teaching of myPhD.
I am grateful to Dr Andrea Rizzo and Dr Mauro Martelli to supporting me with their experience during this work and to helping me with their always qualified and accurated advices.
Thank to Mariano Tantillo for his assistance during analytical work at the noble gases laboratory, to Lorenzo Brusca and Sergio Bellomo for their help to LA-ICP-MS analyses and finally to Franco Furnari for his suggestions during SEM-EDS measurements.
Dr David Hilton and Dr Massimo Pompilio are thanked for critically reading of my thesis and for their reviews, valuable for improving the manuscript.
Collaborations with Dr Rosa Anna Corsaro and Professor Vittorio Scribano have enriched my research.

References

Acocella, V., Neri, M., 2003. Wath makes flank eruptions? The 2001 Mount Etna eruption and its possible triggering mechanisms. Bullettin Volcanology 65, 517-529.

Allard, P., Behncke, B., D'Amico, S., Neri, M., Gambino, S., 2006. Mount 1993-2005: Anatomy o fan evolving eruptive cycle. Earth Science Reviews 78, 85-114.

Allègre, C.J., Moreira, M., Staudacher, T., 1995. 4He/3He dispersion and mantle convection. Geophysical Research Letters 22, 2325-2328.

Amore, C., Carveni, P., Scribano, V., Sturiale, C., 1988. Facies ed età del vulcanismo nella fascia sudorientale della Sicilia (Pachino-Capo Passero). Bollettino della Società Geologica Italiana 107, 3-4.

Anders, E., Grevesse, N.,1989. Abundances of the elements: Meteoritic and solar. Geochimica and Cosmochimica Acta 53, 197-214.

Anderson, L., 2007. New theory of the Earth. California Institute of Technology.

Arevalo, Jr. R.., McDonough W. F., 2010.Chemical variations and regional diversity observed in MORB. Chemical Geology 271, 70-85.

Armienti, P., Innocenti, F., Petrini, R., Pompilio, M., Villari, L., 1988. Sub-aphyric alkali basalt from Mt Etna: inferences on the depth and composition of the source magma. Rendiconti della Società Italiana di Mineralogia e Petrologia 43, 877-891.

Armienti, P., Innocenti, F., Petrini, R., Pompilio, M., Villari, L., 1989. Petrology and Sr-Nd isotope geochemistry of recent lavas from Mt Etna: bearing on the volcano feeding system. Journal of Volcanology and Geothermal Research 39, 315-327.

Armienti, P., Tonarini, S., D'Orazio, M., Innocenti F., 2004. Genesis and Evolution of Mt Etna alkaline lavas: petrological and Sr-Nd-B isotope costraints 73, 29-52.

Armienti, P., Tonarini, S., Innocenti, F., D'Orazio, M., 2007. Mount Etna pyroxene as tracerof petrogenetic processes and dynamics of the feeling system. Geol. Soc. Am. Special Paper 418, 265–275.

Atzori, P., Mazzoleni, P., Punturo, R., Scribano, V. 1999. Garnet-spinel pyroxenite xenoliths from Hyblean plateau (South-eastern Sicily, Italy). Mineralogy and Petrology 66, 215–226.

Azzaro, R., 1999. Earthquake surface faulting at Mount Etna volcano (Sicily) and implication for active tectonics. Journal of Geodynamics 29, 193-213.

Ballentine, C.J., Barfod, D.N., 2000. The origin of air-like noble gases in MORB and OIB. Earth and Planetary Science Letters 180, 39–48.

Barberi, F., Civetta, L., Gasparini, P., Innocenti, F., Scandone, R., Villari, L., 1974. Evolution of a section of the Africa-Europe plate boundary: paleomagnetic and volcanological evidence from Sicily. Earth and Planetary Science Letters 22, 123-132.

Beccaluva, L., Siena, F., Coltorti, M., Digrande, A., Lo Giudice, A., Macciotta, G., Tassinari, R., Vaccaro, C., 1998. Nephelinitic to tholeiitic magma generation in a transtensional tectonic setting: an integrated model for the Iblean vulcanism, Sicily. Journal of Petrology 39, 1547-1576.

Beccaluva, L., Azzouni-Sekkal, A., Benhallou, A., Bianchini, G., Ellam, R.M., Marzola, M., Siena, F., Stuart, F.M., 2007. Intracratonic asthenosphere upwelling and lithosphere rejuvenation beneath the Hoggar swell (Algeria): evidence from HIMU metasomatised lherzolite mantle xenoliths. Earth and Planetary Science Letters 260, 482–494.

Beccaluva, L., Bianchini, G., Ellam, R.M., Marzola, M., Oun, K.M., Siena, F., Stuart, F.M., 2008. The role of HIMU metasomatic components in the African lithospheric mantle: petrological evidence from the Gharyan peridotite xenoliths, NW Libya. In: Coltorti, M., Gregoire, M. (Eds.), Mantle metasomatism in intra-plate and supra subduction settings. London Geological Society, Special Publication, 293, pp. 253–277.

Ben-Avraham, Z., Grasso, M., 1990. Collisional zone segmentation in Sicily and surrounding areas in the Central Mediterranean. Special issue 4, 131-139.

Bianchini, G., Clocchiatti, R., Coltorti, M., Ioron, J.L., Vaccaro, C., 1998. Petrogenesis of mafic lavas from the northernmost sector of the Hyblean district (Sicily). Eur J Mineral 10, 301-315.

Bianchini, G., Bell, K., Vaccaro, C., 1999. Mantle sources of the Cenozoic Iblean volcanism (SE Sicily-Italy): Sr-Nd-Pb isotopic constraints. Mineralogy and Petrology 67, 213-221.

Bianchini, G., Yoshikawa, M., Sapienza, G.T., 2010. Comparative study of ultramafic xenoliths and associated lavas from South-Eastern Sicily: nature of the lithospheric mantle and insights on magma genesis. Mineralogy and Petrology 98, 111-121.

Bodinier, J.L., Godard, M., 2003. Orogenic, ophiolitic, and abyssal peridotites. Treatise on Geochemistry, Part 2, Elsevier Ltd., pp 103–170

Bottari, A., Lo Giudice, E., Patane, G. Romano, R., Sturiale C., 1975. L'eruzione etnea del Gennaio-Marzo 1974, Riv. Miner. Siciliana, 154– 156, 175– 199.

Bousquet, J.C., Lanzafame, G., 2004. The Tectonics and Geodynamics of Mt Etna: Synthesis and Interpretation of Geological and Geophysical Data. Mt Etna: Volcano Laboratory. Geophysical Monograph Series 143, 29-47.

Branca, S., Del Carlo, P., 2004. Eruption of Mount Etna during the past 3.200 years: A revised compilation integrating the historical and stratigraphic records. In Bonaccorso, A., Calvari, S., Coltelli, M., Del Negro, C., Falsaperla, S. Mt Etna: Volcano Laboratory. Geophysical Monograph Series 143, 1-29.

Burnard, P., 2004. Diffusive fractionation of noble gases and helium isotopes during mantle melting. Earth and Planetary Science Letters 220, 287-295.

Burollet, F.P., Mugniot, J.M., Sweeney, P., 1978. The geology of the Pelagian Block: the margins and basins of Southern Tunisia and Tripolania. In: Nairm, A.E.M., Kanes, W.H., Stehli, F.G. (Eds.), The Ocean Basins and Margins, The Western Mediterranean vol. 4b. Plenum Press, NY, pp. 331-359.

Cadoux, A., Blichert-Toft J., Pinti D.L., Albarède F., 2007. A unique lower mantle source for Southern Italy volcanics. Earth and Planetary Science Letters 259, 227-238.

Calvari, S., Tanner, L.H., Groppelli, G., Norini, G. (2004). A comprehensive model for the opening of the Valle del Bove depression and hazard evaluation for the eastern flank of Etna volcano. In Mt Etna: Volcano Laboratory. Geophysical Monograph Series 143, 65-75.

Caracausi, A., Italiano, F., Paonita, A., Rizzo, A., Nuccio, P.M., 2003. Evidence of deep magma degassing and ascent by geochemistry of peripheral gas emissions at Mount Etna (Italy): Assessment of the magmatic reservoir pressure. J. Geophys. Res. 108, 2463.

Carter, S.R., Civetta L., 1977. Genetic implications of the isotope and trace element variations in the easter Sicilian volcanics. Earth and Planetary Science Letters 36, 168-180.

Carter, S.R., Evensen N.M., Hamilton P.J., O'Nions R.K., 1978. Neodymium and strontium isotope evidences for crustal contamination of continental volcanics. Science 202, 743-747.

Carveni, P., Grasso, M.F., Romano, R., Tricomi, S., 1991(a). Vulcanismo del margine settentrionale Ibleo. Mem Soc Geol It 47, 417-429.

Carveni, P., Romano, R., Capodicasa, A., Tricomi, S., 1991(b). Geologia dell'area vulcanica di Capo Passero (Sicilia Sud-orientale). Mem Soc Geol It 47, 431-447.

Catalano, S., Torrisi, S., Ferlito, C., 2004. The relationship between Late Quaternary deformation and volcanism of Mt Etna (eastern Sicily): new evidence from the sedimentary substratum in the Catania region. Journal of Volcanology and Geothermal Research 132, 311-334.

Cebria, J.M., Wilson, M., 1995. Cenozoic mafic magmatism in Western/Central Europe: a common European asthenospheric reservoir. Terra Nova 7, 162.

Chauvel, C., Hofmann, A. W., Vidal. Ph., 1992. HIMU-EM, the French Polynesian Connection. Earth and Planetary Science Letters 110, 99-119.

Chester, D.K., Dunkam, A.M. 1979. Interrelationships between volcanic and alluvial sequences in the evolution of the Simeto river valley, Mount Etna Sicily. Catena 6, 293-315.

Chester, D.K., Dunkam, A.M., Guest, J.E., Kilburn, C.R.J., 1985. Mount Etna: the anatomy of a volcano. Chapman and Hall, London 404 pp.

Clocchiatti, R., Joron, J.L., Treuil, M., 1988. The role of selective alkali contamination in the evolutionof recent historic lavas of Mt. Etna. Journal of Volcanology and Geothermal Research, 34, 241-249.

Clocchiatti, R., Schiano, P., Ottolini, L., Bottazzi, P., 1998. Earlier alkaline and transitional magmatic pulsation of Mt Etna volcano. Earth and Planetary Science Letters 163, 399-407.

Clocchiatti, R., Condomines, M., Guénot, N., Tanguy, J.C., 2004. Magma changes at Mount Etna: the 2001 and 2002–2003 eruptions. Earth Planet. Sci. Lett. 226, 397–414.

Cocina, O., Neri, G., Privitera, E., Spampinato, S., 1997. Stress tensor computations in the Mount Etna area (Southern Italy) and tectonic implications. Journal Geodynamics 23, 109-127.

Cocina, O., Neri, G., Privitera, E., Spampinato, S., 1998. Seismogenic stress field beneath mt Etna (South Italy) and possible relationships with the volcano-tectonic features. Journal of Volcanology and Geothermal Research 83, 335-348.

Coltelli, M., Del Carlo, P., Pompilio, M., Vezzoli, L., 1998. Discovery of a Plinian basaltic eruption of Roman age at Etna volcano, Italy. Geology 26, 1095-1098.

Coltelli, M., Del Carlo, P., Pompilio, M., Vezzoli, L., 2005. Explosive eruptions of a picrite: The 3930 BP subplinian eruption of Etna volcano (Italy). Geophysical Research Letter 32, L23307, doi:10.1029/2005GL024271.

Condomines, M., Tanguy, J.C., Kieffer, G., Allegre, C.J., 1982. Magmatic evolution of a volcano studied by 230Th–238U disequilibrium and trace element systematics: the Etna case. Geochim. Cosmochim. Acta 46, 1397–1416.

Condomines,M., Bouchez, R.,Ma, J.L., Tanguy, J.C., Amosse, J., Piboule,M.,1987. Short-lived radiactive disequilibria and magma dynamics in Etna volcano. Nature 325, 607–609.

Continisio, R., Ferrucci, F., Gaudiosi,G., Lo Bascio, D., Ventura, G., 1997. Malta Escarpment Mt Etna: early stages of an asymmetric rifting process? Evidences from geophysical and geological data. Acta Vulcanologica 9, 45-53.

Corsaro, R.A., Cristofolini, R., 1997. Geology, geochemistry and mineral chemistry of tholeiitic to transitional Etnean magmas. Acta Vulcanologica 9, 55-66.

Corsaro, R.A., Cristofolini, R., 2000. Subacqueous volcanism in the Etnean area: evidence for hydromagmatic activity and regional uplift inferred from the Caste Rock of Acicastello. Journal of Volcanology and Geothermal Research 95, 209-225.

Corsaro, R.A., Neri, M., Pompilio, M., 2002. Paleo-environmental and volcano-tectonic evolution of the southern flank of Mt Etna during the last 225 ka inferred from the volcanic succession of the "Timpe", Acireale, Sicily. Journal of Volcanology and Geothermal Research 113, 289-306.

Corsaro, R.A., Pompilio, M., 2004. Dynamics of magmas at Mount Etna. In: Mount Etna: Volcano Laboratory. Geophysical Monograph Series 143, 91-110.

Corsaro, R.A., Miraglia, L., Pompilio, M., 2006. Petrologic evidence of a complexplumbing system feeding the July–August 2001 eruption of Mt. Etna, Sicily, Italy. Bull. Volcanol. 69, 401–421.

Corsaro, R.A., Métrich, N., Allard, P., Andronico, D., Miraglia, L., Fourmentraux, C., 2009. The 1974 flank eruption of Mount Etna: An archetype for deep dike-fed eruptions at basaltic volcanoes and a milestone in Etna's recent history. Journal of Geophysical Research 114, B07204, doi:10.1029/2008JB006013.

Craig, H., Lupton, J.E., 1976. Primordial neon, helium and hydrogen in oceanic basalts.Earth Planet. Sci. Lett. 31, 369–385.

Del Carlo, P., Vezzoli, L., Coltelli, M., 2004. Last 100 ka Tephrostratigraphic Record of Mount Etna. In Mt Etna: Volcano Laboratory. Geophysical Monograph Series 143, 77-89.

De Rita, D., Frazzetta, G., Romano, R., 1991. The Biancavilla-Montalto ignimbrite (Etna, Sicily). Bull.Volc. 53, 121-131.

Di Carlo, I., Pichavant, M., Rotolo, S. G., Scaillet, B., 2006. Experimental crystallization of a high-K arc basalt: the golden pumice, Stromboli volcano (Italy). Journal of Petrology 47, 1317-1343.

Doglioni, C., Innocenti, F., Mariotti, G., 2001. Why Mt Etna? Terranova 13, 25-31.

Downes, H, 2007. Origin and significance of spinel and garnet pyroxenites in the shallow lithospheric mantle: Ultramafic massifs in orogenic belts in Western Europe and NW Africa. Lithos 99, 1–24.

Dunai, T. J. and Baur, H., 1995. Helium, neon, and argon systematics of the European subcontinental mantle: Implications for its geochemical evolution. Geochimica and Cosmochima Acta 59, 2767-2783.

Eggins, S.M., Rudnick, R.L., McDonough, W.F., 1998. The composition of peridotites and their minerals: a laser-ablation ICP-MS study. Earth and Planetary Science Letters 154, 53–71.

Finetti, I., Lentini, F., Carbone, S., Catalano, S., Del Ben, A., 1996. Il sistema Appennino meridionale-Arco Calabro-Sicilia nel Mediterraneo centrale: studio geologico-geofisico. Bollettino della Società Geologica Italiana 115, 529-559.

Gautheron, C., Moreira, M., Allègre, C., 2005. He, Ne and Ar composition of the European lithospheric mantle. Chemical Geology 217, 97–112.

Giggenbach, W.F., Sano, Y., Wakita, H., 1993. Isotopic composition of helium, and CO2 and CH4 contents in gas produced along the New Zealand part of a convergent plate boundary. Geochimica et Cosmochimica Acta 57, 3427–3455.

Graham, D.W., 2002. Noble gas isotope geochemistry of mid-ocean ridge and ocean island basalts: characterization of mantle source reservoir. In: Porcelli D.P., Ballentine C.J., Wieler, R., (Eds), Noble Gases in Geochemistry and Cosmochemistry, Rev. Mineral. Geochem., vol. 47, Washington, D. C., pp. 247–317.

Gurenko, A.A., Sobolev, A.V., Hoernle, K., Hauff, F., Schmincke, H.U., 2009. Enriched, HIMU-type peridotite and depleted recycled pyroxenite in the Canary plume: a mixed-up mantle. Earth Planetary Science Letters 277, 514–524.

Gvirtzman, Z., Nur, A., 1999. The formation of Mount Etna as the consequence of the slab rollback. Nature 401, 782-785.

Harrison, D., Barry, T., Turner, G., 2004. Possible diffusive fractionation of helium isotopes in olivine and clinopyroxene phenocrysts. Eur. J. Mineral. 16, 213–220.

Hanyu, T., Kaneoka, I., 1998. Open system behavior of helium in case of the HIMU source area. Geophysical Research Letters 25, 687–690

Heber, S.V., Brooker R.A., Kelley P.S., Wood J.B., 2007. Crystal–melt partitioning of noble gases (helium, neon, argon, krypton, and xenon) for olivine and clinopyroxene. Geochimica et Cosmochimica Acta 71,1041–1061.

Hilton, D.R., Barling, J., Wheller, G.E., 1995. Effect of shallow level contamination on the helium isotope systematics of ocean-island-lavas. Nature 373, 330-333.

Hoernle, K., Zhang, Y.S., Graham, D., 1995. Seismic and geochemical evidence for large scale mantle upwelling beneath the eastern Atlantic and western and central Europe. Nature 374, 34–39.

Hofmann, A.W., 1988. Chemical differentiation of the earth: The relationship between mantle, continental crust, and oceanic crust. Earth and Planetary Science Letters 90, 297- 314.

Iacono-Marziano, G., Paonita, A., Rizzo, A., Scaillet, B., Gaillard, F., 2010. Noble gas solubilities in silicate melts: New experimental results and a comprehensive model of the effects of liquid composition, temperature and pressure. Chemical Geology 279, 145–157.

Kamenetsky, V.S., Clocchiatti R., 1996. Primitive magmatism of Mt. Etna: insights from mineralogy and melt inclusions. Earth and Planetary Science Letters 142, 553-572.

Kamenetsky, V.S., Pompilio, M., Métrich, N., Sobolev, A., Kuzmin, D.V., Thomas, R., 2007. Arrival of extremely volatile-rich high-Mg magmas changes explosivity of Mount Etna. Geological Society of America 35, 255-258.

Lanzafame, G., Bousquet, J.C., 1997. The Maltese escarpment and its extension from the Mt Etna to the Aeolian islands (Sicily): importance and evolution of a lithosphere discontinuity. Acta Vulcanologica 9, 113-120.

Lanzafame, G., Neri, M., Coltelli, M., Lodato, L., Rust, D., 1997. North-south compression in the Mt Etna region (Sicily): spatial and temporal distribution. Acta Vulcanologica 9, 121-133.

Le Bas, M.J., Le Maitre, E.W., Streckeisen, A., Zanettin, B., 1986. A chemical classification of volcanic rocks based on the total alkali-silica diagram. Journal of Petrology 27, 745-750.

Lentini, F., Carbone, S., Catalano, S., Grasso, M., 1996. Elementi per la ricostruzione del quadro strutturale della Sicilia orientale. Memorie Società Geologica Italiana 51, 179–195.

Longaretti, G., Rocchi, S., 1990. Il magmatismo dell'avampaese ibleo (Sicilia orientale) tra il Trias e il Quaternario: dati stra-tigrafici e petrologici del sottosuolo. Memorie Società Geologica Italiana 45, 911-925.

Lustrino, M., Wilson, M., 2007. The circum-Mediterranean anorogenic Cenozoic igneous province.Earth-Science Review 81, 1-65.

Lux, G., 1987. The behavior of noble gases in silicate liquids: solution, diffusion, bubbles and surface effects, with applications to natural samples. Geochim. Cosmochim. Acta 51, 1549–1560.

Macera, P., Gasperini, D., Piromallo, C., Blichert-Toft, J., Bosch, D., Del Moro, A., Martin, S., 2003. Geodynamic implications of deep mantle upwelling in the source of Tertiary volcanics from the Veneto region (South-Eastern Alps). Journal of Geodynamics 36, 563–590.

Mamyrin, B.A., Tolstikhin, I.N., 1984. Helium Isotopes in Nature. Elsevier, Amsterdam. 273.

Martelli, M., Nuccio, P.M., Stuart, F.M., Burgess, R., Ellam, R.M., Italiano, F., 2004. Helium strontium isotope constraints on mantle evolution beneath the Roman Comagmatic Province, Italy. Earth and Planetary Science Letters 224, 295-308.

Martelli, M., Nuccio, P.M., Stuart, F.M., Di Liberto, V., Ellam, R.M., 2008. Constraints on mantle source and interactions from He-Sr isotope variation in Italian Plio-Quaternary volcanism. Geochemistry, Geophysics, Geosystems doi:10.1029/2007GC001730.

Martelli, M., Bianchini, G., Beccaluva, L., Rizzo, A., 2011. Helium and argon isotopic compositions of mantle xenoliths from Tallante and Calatrava, Spain. Journal of Volcanology and Geothermal Research 185, 172-180.

Marty, B., Zashu, S., Ozima, M., 1983. Two noble gas components in a Mid-Atlantic Ridge basalt. Nature 302, 238-240.

Marty, B., Trull, T., Lussiez, P., Basile, I.,Tanguy, J.C., 1994. He, Ar, O, Sr and Nd isotope constraints on the origin and evolution of Mount Etna magmatism. Earth and Planetary Science Letters 126, 23-39.

Mc Guire, W.J., Stewart, I.S., Saunders S.J., 1997. Intra-volcanic rifting at Mount Etna in the context of regional tectonics. Acta Volcanologica 9, 147-156.

Meibom, A., Anderson, D.L., 2004. The statistical upper mantle assemblage. Earth and Planetary Science Letters 217, 123–139.

Métrich, N., Allard, P., Spilliaert, N., Andronico, D., Burton, M. 2004. 2001 flank eruption of the alkali and volatile-rich primitive basalt responsible for Mount Etna's evolution in the last three decades, Earth and Planetary Science Letters 228, 1 –17.

Michard A., Albarède, F., 1985. Hydrothermal uranium uptake at ridge crests. Nature 317, 244–246.

Miraglia, L. 2002. Evidence for heterogeneous magmas in the feeding system of the 1763 ''La Montagnola'' eruption at Mount Etna. Plinius 27, 108– 112.

Morbidelli, L., 2003. Le rocce e i loro costituenti. Bardi Editore, Roma.

Moreira, M., Sarda, P., 2000. Noble gas constraints on degassing processes. Earth and Planetary Science Letters 176, 375– 386.

Moreira, M., Kurz, M.D., 2001. Subducted oceanic lithosphere and the origin of the 'high μ' basalt helium isotopic signature. Earth and Planetary Science Letters 189, 49-57.

Nakai, S., Wakita, H., Nuccio, P.M., Italiano, F., 1997. MORB type neon in an enriched mantle beneath Etna, Sicily. Earth and Planetary Science Letters 153, 57-66.

Nimis, P., 1998. Clinopyroxene geobarometrv of pyroxenitic xenoliths from Hyblean plateau (SE Sicity, Itaty). European Journal of Mineralogy 10, 521–533.

Nuccio, P.M.. and Paonita, A., 2000. Investigation of the noble gas solubility in H2O–CO2 bearing silicate liquids at moderate pressure II: the extended ionic porosity (EIP) model. Earth and Planetary Science Letters 183, 499-512.

Nuccio, P.M., Paonita, A., Rizzo A., Rosciglione, A., 2008. Elemental and isotope covariation of noble gases in mineral phases from Etnean volcanics erupted during 2001-2005, and genetic relation with peripheral gas discharges. Earth and Planetary Science Letters 272, 683-690.

Ozima, M., Podosek, F.A., 1983. Noble Gas Geochemistry. In: Cambridge University Press, New York.

Paonita, A., Martelli, M., 2006. Magma dynamics at mid-ocean ridges by noble gas kinetic fractionation: assessment of magmatic ascent rates. Earth and Planetary Science Letters 241, 138-158.

Paonita, A., Martelli, M., 2007. A new view of the He-Ar-CO2 degassing at mid-ocean ridges: Homogeneous composition of magmas from the upper mantle. Geochimica et Cosmochimica Acta 71, 1747-1763.

Parello, F., Allard, P., D'Alessandro, W., Federico, C., Jean-Baptiste, P., Catani, O., 2000. Isotope geochemistry of Pantelleria volcanic fluids, Sicily Channel rift: a mantle volatile endmember for volcanism in southern Europe. Earth and Planetary Science Letters 180, 325–339.

Patacca, E., Scandone, P., Giunta, G., Liguori, V., 1979. Mesozoic palaeotectonic evolution of the Ragusa Zone (Southern Sicily).Geologica Romana 18, 331-369.

Patterson, D.B., Farley, K.A., Mcinnes, B.I.A, 1197. Helium isotopic composition of the Tabar-Lihir-Tanga-Feni island arc, Papua New Guinea. Geochemical and Cosmochimica Acta 61, 2485-2496.

Pearce, J. A., 1983. Role of the cub-continental lithosphere in magma genesis at active continental margines. *In* Hawkesworth, C. J. and Norry, M. J. eds., *Continental basalts and mantle Xenoliths*, 230-250, Shiva, Nantwich, Cheshire, U.K.

Perinelli, C., Sapienza, G.T., Armienti, P., Morten, L., 2008. Metasomatism of the upper mantle beneath the Hyblean Plateau (Sicily): evidence from pyroxenes and glass in peridotite xenoliths. London Geological Society, Special Publication 293, 197-221.

Piromallo, C., Gasperini, D., Macera, P., Faccenna, C., 2008. A late Cretaceous contamination episode of the European–Mediterranean mantle. Earth and Planetary Science Letters 268, 15–27.

Platania, G., 1905. Origine delle Timpa della scala. Contributo allo studio dei burroni vulcanici. Bollettino della Società Geologica Italiana 24, 451-460.

Porcelli, D.R., O'Nions, R.K., O'Reilly, S.Y., 1986. Helium and strontium isotopes in ultramafic xenoliths. Chemical Geology 54, 237-249.

Porcelli, D., Ballentine, C., 2002. Models for the distribution of terrestrial noble gases and evolution of the atmosphere. In: Porcelli D.P., Ballentine C.J., Wieler, R., (Eds), Noble Gases in Geochemistry and Cosmochemistry, Rev. Mineral. Geochem., vol. 47, Washington, D. C., pp. 411–480.

Punturo R., Scribano V., 1997. Dati geochimici e petrologici preliminari su xenoliti di clinopirossenite a grana ultragrossa e websteriti nelle vulcanoclastiti mioceniche dell'alta Valle Guffari (Monti Iblei, Sicilia). Mineralogica et Petrographica Acta, 40: 95-116.

Rittman, A., 1965. Notizie sull'Etna. Suppl. Nuovo Cimento, 3(I), 1117-1123.

Roeder, P.L., Emslie, R.F., 1970. Olivine- liquid equilibrium. Contributions to Mineralogy and Petrology 29, 275-289.

Rocchi, S., Longaretti, G., Ferrari, L., 1995. Evoluzione del magmatismo nel sottosuolo della Sicilia Sudorientale. In: Ferrucci, F., Innocenti., F., Progetto Etna 1993-1995, pp. 151-157.

Rotolo, S.G., Castorina, F., Cellura, D., Pompilio, M., 2006. Petrology and geochemistry of submarine volcanism in the Sicily Channel Rift: Journal of Geology 114, 355-365.

Sapienza, G., Scribano, V., 2000. Distribution and representative whole rock chemistry of deep-seated xenoliths from the Iblean Plateau, South-Eastern Sicily, Italy. Periodico di Mineralogia 69, 185–204.

Sapienza, G., Hilton, D.R., Scribano, V., 2005. Helium isotopes in peridotite mineral phases from Hyblean Plateau xenoliths (southeastern Sicily, Italy). Chemical Geology 219, 115–129.

Sarda, P., 2004. Surface noble gas recycling to the terrestrial mantle. Earth and Planetary Science Letters 228, 49–63.

Schiano, P., Crocchiati, R., Ottolini, L., Busà, T., 2001. Transition of Mount Etna lavas from a mantle-plume to an island-arc magmatic source. Nature 412, 900-904.

Scribano, V., Viccaro, M., Cristofolini, R., Ottolini, L., 2008. Metasomatic events recorded in ultramafic xenoliths from the Hyblean area (Southeastern Sicily, Italy). Mineralogy and Petrology 95, 232-250.

Shaw, A.M., Hilton, D.R., Fisher, T.P., Walker, J.A., De Leeuw, G.A.M., 2006. Helium isotope variations in mineral separates from Costa Rica and Nicaragua. Assessing crustal contribution, timescale variations and diffusion related mechanism. Chemical Geology 230, 124-139.

Sobolev, A.V., Hofmann, A.W., Brügmann, B., Batanova, V.G., Kuzmin, D.V., 2008. A quantitative link between recycling and osmium isotopes. Science 321, 536.

Spilliaert, N., Allard, P., Me´trich, N., Sobolev, A. V., 2006. Melt inclusion record of the conditions of ascent, degassing, and extrusion of volatile-rich alkali basalt during the powerful 2002

flank eruption of Mount Etna (Italy), J. Geophys. Res., 111, B04203, doi:10.1029/2005JB003934.

Sturiale, C. 1970. La singolare eruzione dell'Etna del 1763 ''La Montagnola''. Bull. Mineral. Rend. Soc. Ital. Mineral. Petrol., 26, 314– 351.

Sun, S.-s., McDonough, W.F., 1989. Chemical and isotopic systematics of oceanic basalts: implications for mantle composition and processes. In: Saunders,A.D.,Norry,M.J. (Eds.), Magmatism in the Ocean Basins. Geological Society Special Publication, pp. 313–345.

Tanguy, J. C., Kieffer, G., 1977. The 1974 eruption of Mount Etna, Bullettin of Volcanology 40, 239– 252.

Tanguy, J.C., 1978. Tholeitic basalt magmatism of Mount Etna and its relations with the alkaline series. Contributions to Mineralogy and Petrology 66, 51-67.

Tanguy, J.C., Condomines, M., Kieffer, G., 1997. Evolution of Mount Etna magma: Constraints on the present feeding system and eruptive mechanism. Journal of Volcanology and Geothermal Research 75, 221-250.

Tonarini, S., D'orazio, M., Armienti, P., Innocenti, F., Scribano, V., 1996. Geochemical features of Eastern Sicily lithosphere as probed by Hyblean xenoliths and lavas. European Journal of Mineralogy 5, 1153–1174.

Tonarini, S., Armienti, P., D'Orazio, M., Innocenti, F., 2001. Subduction-like fluids in the genesis of the Mt Etna magmas: evidence from boron isotopes and fluid mobile elements. Earth and Planetary Science Letters 5989, 1-13.

Torelli, L., Grasso, M., Mazzoldi, G., Peis, D., 1998. Plio-Quaternary tectonic evolution and structure of the Catania foredeep, the northern Hyblean Plateau and the Ionian shelf (SE Sicily). Tectonophysics 298, 209-221.

Trua T., Esperanca S., Mazzuoli R., 1998. The evolution of the lithospheric mantle along the N.African Plate: geochemical and isotopic evidence from tholeitiic and alkaline volcanic rocks of the Hyblean plateau, Italy. Contribution of Mineralogy and Petrology 131, 307-322.

Viccaro, M., Ferlito, C., Cortesogno, L., Cristofolini, R., Gaggero, L., 2006. Magma mixing during the 2001 event at Mount Etna (Italy): effect on the eruptive dynamics. Journal of Volcanology and Geothermal Research 149, 139-159.

Viccaro, M., Cristofolini, R., 2008. Nature of mantle heterogeneity and its role in the short-term geochemical and volcanological evolution of Mt Etna (Italy). Lithos 105, 272-288.

Wadge, G., 1980. Output rate of magma from active central volcanoes. Nature 288, 253-255.

White, W.M., 2007. Geochemistry. John-Hopkins Univeristy Press.

Wilson, M., Downes, H., 1992. Mafic alkaline magmatism associated with the European Cenozoic Rift system. Tectonophysics 208, 173–182.

Wilson, M., Bianchini, G., 1999. Tertiary–Quaternary magmatism within the Mediterranean and surrounding regions. In: Durand, Jolivet, Horvath, Seranne (Eds.), The Mediterranean Basins: Tertiary extension within the Alpine orogen. Geological Society, London, vol. 156, pp. 141–168.

Yamamoto, J., Nishimura, K., Takeshi, S., Keiji, T., Naoto, T., Yuji, S., 2009. Diffusive fractionation of noble gases in mantle whit magma channels: Origin of low He/Ar in mantle-derived rocks. Earth and Planetary Science Letters 280, 167-174.

Zindler, A., Hart S.R., 1986. Chemical Geodynamics. Earth and Planetary Science Letters 14, 493-571.

APPENDIX

ANALYTICAL METHODS

MINERAL ANALYSIS

Major elements

Mineral compositions of both Etnean and Hyblean samples were determined at DISTeM, (University of Palermo) using a LEO440 scanning electron microprobe (SEM), coupled to an Oxford EDS system, Link ISIS 300 software and Pentafet Si(Li) detector. Analytical conditions: 20kv accelerating voltage, 600 pA probe current. Quantitative analyses were calibrated with natural mineral standards and synthetic glasses. The analyses were carried out on samples incorporated into an epoxy-resin or on polished thin sections.

Fig A1– SEM-EDS at Palermo University (Dip DiSTeM).

Trace elements

Trace-element analyses of Hyblean olivine and pyroxene phenocrysts were performed using the laser ablation ICP-MS technique at Istituto Nazionale di Geofisica e Vulcanologia (INGV), Sezione di Palermo. Selected samples were incorporated into an epoxy-resin puck that was polished before analysis. The analytical system consisted of an Agilent-7500 CX quadrupole mass spectrometer coupled with an ArF excimer laser ablation system (GeoLas Pro). During analysis, samples were maintained in a He atmosphere, with a laser output energy of 10 J/cm^2, a repetition rate of 10 Hz, and a 130-µm-diameter circular spot. We used Ca, Si, and Fe as internal standards and NIST 612 as an external standard. The NIST 612 analyses were carried out at the start, middle, and end of each analytical session. The precision was determined during each analysis session from the variance of ~15 NIST 612 measurements, which gave a relative standard deviation of <5%. The accuracy, calculated using the BCR-2 international standard, was <10% for most of the elements.

Fig A2 – LA-ICP-MS at INGV-Palermo.

NOBLE GAS ANALYSIS IN FLUID INCLUSIONS

Samples preparation

In order to collect the necessary amount of phenocrysts for noble gases analyses in fluid inclusions, xenolith and lava samples were broken by mechanical disintegration through a jaw crusher (Retsch BB200). Subsequently, the fractions corresponding to sizes of 1 and 0.5 mm were separated through appropriate sieves. Olivine and pyroxene phenocrysts were handpicked under binocular microscope from each granulometric fraction, avoiding crystals with small amount of lava on the surface and/or those altered. Separated mineral were ultrasonically cleaned, with three cycles of 10 minutes, in 5% HNO_3 , distilled water and finally in high-purity acetone.

Fig A3 –Shaker for sieves

Fig A3–Binocular microscope for manual picking.

Crushing procedure

Crushing extraction was carried out on selected minerals in order to perform chemical and isotopic analyses of noble gases entrapped into fluid inclusions. The crushing device consists of a piston/cylinder operated by an hydraulic press (~200 bar) and a crusher chamber where the minerals are mechanically broken. A pressure control system allows to regulate the crushing pressure on the sample. The quantity of loaded sample is established considering the expected amount of noble gases released by crushing. We loaded ≤ 1 g of sample for the Hyblean xenoliths phenocrysts and 1-2 g for the Etnean minerals as poorest in gases and characterized by a minor pressure of trapping

with respect to xenoliths. Before each analytical session, the crusher chamber and all extraction lines are pumped in ultra high vacuum, overnight baking at 130°C in order to degas the volatiles adsorbed in the surfaces of crystals and of the crusher/extraction line. Gases were extracted by single-step crushing at about 200 bar pressure, so to avoid the release of noble gases contained in the crystal lattice sites. Gases liberated by sample are expanded into the 976 cm^3 preparation line, where He, Ne and Ar are purged of reactive species by adsorbtion in Zr-Al getter traps and then separated in two fractions (respectively He+Ne and Ar), by charcoal trap cooled at 77 K by liquid nitrogen. The He+Ne mixture is adsorbed and concentrated in another charcoal trap cooled down at 12 K by a cold-head. The concentration of the sample in a small volume (about few tens of cm^3), before expansion in the mass spectrometer, aims to reduce the analytical error during analysis. The He and Ne are separated by progressive temperature increase (the release of He occurs at 40 K while that of Ne at 85 K) and then are separately admitted in a split flight tube mass spectrometer (Helix SFT) for isotope analyses. Ar previously entrapped into charcoal trap is released by heating the trap to room temperature and then analysed by a multi-collector mass spectrometer (Argus).

The analytical error in air standard estimated for isotopic analyses is below 0.2 % for He and below 0.4% for the Ar. The He, Ne and Ar blanks, measured each day before the analyses, were negligible. The uncertainties in the noble-gas abundances were less than 10%.

Fig A4 – **a)** Crusher system at INGV-Palermo **b)** Steel container of minerals used during crusher procedure.

Sr-Nd ISOTOPIC ANALYSIS

Sr and Nd isotopic compositions were determined on Hyblean clinopyroxenes of peridotitic and pyroxenitic nodules (between 0.3 and 0.5 g).

Mineral powders were leached with cold 2.5 N HCl for 10 min and with warm 2.5 N HCl for 10 min, then rinsed several times in pure sub-boiling distilled water, and finally dissolved with high-purity HF-HNO3-HCl mixtures. Sr and Nd were separated using standard cation-exchange methods.

Sr and Nd isotope ratios were measured statically by thermal ionization mass-spectrometry (TIMS, ThermoFinnigan Triton TI) at the Istituto Nazionale di Geofisica e Vulcanologia, sezione di Napoli Osservatorio Vesuviano. Sr and Nd isotope ratios were corrected for mass fractionation using $^{86}Sr/^{88}Sr=0.1194$ and $^{146}Nd/^{144}Nd=0.7219$.

Replicate analysis of NIST NBS 987 and La Jolla Reference Standard gave average values of 0.710240 ± 0.000012 (2σ, n=25) and 0.511846 ± 0.000015 (2σ, n=23), respectively.

The external reproducibility 2σ during the period of measurements is calculated according to Goldstein et al. (2003). Sr blank was of the order of 0.5 ng during the period of chemical processing.

T (°C)	Pressure (bar)	F (melt fraction)	SiO_2 (wt%)	TiO_2	Al_2O_3	Fe_2O_3	FeO	MgO	CaO	Na_2O
1310	10000	0,003	50,18	0,82	15,71	1,06	8,09	10,97	8,32	4,84
1320	10000	0,008	49,54	0,87	15,25	1,11	8,64	11,53	8,98	4,09
1330	10000	0,014	48,98	0,90	14,75	1,15	9,14	12,06	9,62	3,40
1340	10000	0,023	48,57	0,92	14,19	1,18	9,57	12,56	10,20	2,81
1350	10000	0,033	48,36	0,93	13,59	1,21	9,85	13,04	10,70	2,34
1360	10000	0,046	48,27	0,89	12,92	1,24	10,13	13,50	11,11	1,94
1370	10000	0,061	48,28	0,84	12,18	1,26	10,40	13,97	11,45	1,62
1380	10000	0,080	48,38	0,76	11,37	1,29	10,65	14,45	11,73	1,36
1390	10000	0,101	48,55	0,68	10,51	1,32	10,86	14,96	11,97	1,14
1400	10000	0,126	48,79	0,60	9,58	1,35	11,04	15,51	12,17	0,96

Table A1- Simulation of a isobaric melting process starting from a lherzolitic composition.

T (°C)	Pressure (bar)	F (melt fraction)	SiO_2 (wt%)	TiO_2	Al_2O_3	Fe_2O_3	FeO	MgO	CaO	Na_2O
1250	7400	0,000								
1250	7300	0,001	54,51	0,72	17,30	0,80	5,31	8,69	7,50	5,16
1250	7200	0,002	54,48	0,73	17,26	0,81	5,35	8,72	7,64	5,00
1250	7100	0,003	54,45	0,74	17,22	0,81	5,39	8,76	7,78	4,84
1250	7000	0,004	54,42	0,74	17,17	0,82	5,43	8,80	7,92	4,69
1250	6900	0,005	54,40	0,75	17,12	0,83	5,47	8,84	8,06	4,54
1250	6800	0,006	54,37	0,75	17,07	0,83	5,51	8,87	8,21	4,39
1250	6700	0,007	54,34	0,76	17,01	0,84	5,55	8,91	8,35	4,24
1250	6600	0,009	54,32	0,77	16,96	0,84	5,59	8,94	8,49	4,09
1250	6500	0,010	54,29	0,77	16,89	0,85	5,63	8,98	8,64	3,95
1250	6400	0,011	54,27	0,78	16,83	0,86	5,67	9,01	8,78	3,81
1250	6300	0,013	54,26	0,78	16,76	0,86	5,71	9,04	8,92	3,67
1250	6200	0,015	54,25	0,79	16,69	0,87	5,74	9,07	9,06	3,53
1250	6100	0,016	54,24	0,79	16,61	0,88	5,78	9,10	9,20	3,40
1250	6000	0,018	54,23	0,80	16,53	0,88	5,81	9,13	9,34	3,27
1250	5900	0,020	54,23	0,81	16,45	0,89	5,85	9,15	9,47	3,15
1250	5800	0,022	54,24	0,81	16,36	0,90	5,88	9,18	9,60	3,03
1250	5700	0,024	54,25	0,81	16,27	0,91	5,91	9,20	9,73	2,91
1250	5600	0,026	54,27	0,82	16,18	0,91	5,94	9,23	9,86	2,80
1250	5500	0,028	54,29	0,82	16,08	0,92	5,96	9,25	9,99	2,69
1250	5400	0,031	54,33	0,82	15,98	0,93	5,99	9,27	10,11	2,59
1250	5300	0,033	54,36	0,83	15,87	0,93	6,01	9,28	10,22	2,49
1250	5200	0,035	54,41	0,83	15,76	0,94	6,03	9,30	10,33	2,40
1250	5100	0,038	54,46	0,83	15,65	0,95	6,05	9,32	10,44	2,31
1250	5000	0,041	54,52	0,83	15,53	0,95	6,07	9,33	10,55	2,22
1250	4900	0,043	54,59	0,83	15,41	0,96	6,08	9,35	10,65	2,14
1250	4800	0,049	53,75	0,79	15,32	1,05	6,65	9,30	11,09	2,04

1250	4700	0,052	53,84	0,79	15,19	1,06	6,65	9,31	11,19	1,97
1250	4600	0,054	53,93	0,79	15,07	1,06	6,65	9,32	11,28	1,90
1250	4500	0,057	54,03	0,79	14,94	1,07	6,65	9,33	11,36	1,83
1250	4400	0,060	54,13	0,79	14,80	1,07	6,65	9,34	11,44	1,77
1250	4300	0,063	54,24	0,79	14,66	1,08	6,65	9,35	11,52	1,72
1250	4200	0,066	54,35	0,78	14,52	1,09	6,64	9,36	11,59	1,66
1250	4100	0,069	54,47	0,78	14,38	1,09	6,64	9,37	11,66	1,61
1250	4000	0,072	54,59	0,78	14,24	1,10	6,63	9,38	11,72	1,56
1250	3900	0,075	54,71	0,77	14,09	1,10	6,63	9,39	11,79	1,52
1250	3800	0,078	54,84	0,77	13,94	1,11	6,62	9,41	11,85	1,47
1250	3700	0,081	54,98	0,76	13,79	1,11	6,62	9,42	11,90	1,43
1250	3600	0,084	55,11	0,75	13,63	1,12	6,61	9,43	11,96	1,39
1250	3500	0,087	55,25	0,74	13,48	1,12	6,60	9,44	12,01	1,35
1250	3400	0,090	55,39	0,74	13,32	1,13	6,60	9,46	12,06	1,32
1250	3300	0,093	55,54	0,73	13,16	1,13	6,59	9,47	12,10	1,28
1250	3200	0,096	55,68	0,72	12,99	1,14	6,58	9,49	12,15	1,25
1250	3100	0,099	55,83	0,71	12,83	1,14	6,57	9,50	12,19	1,22
1250	3000	0,102	55,98	0,70	12,66	1,15	6,57	9,52	12,23	1,19
1250	2900	0,105	56,14	0,69	12,49	1,16	6,56	9,54	12,27	1,16
1250	2800	0,109	56,29	0,68	12,32	1,16	6,56	9,56	12,30	1,13
1250	2700	0,112	56,45	0,67	12,14	1,17	6,55	9,58	12,34	1,10
1250	2600	0,115	56,61	0,66	11,96	1,17	6,55	9,61	12,37	1,07
1250	2500	0,119	56,76	0,65	11,78	1,18	6,54	9,63	12,40	1,05
1250	2400	0,122	56,93	0,64	11,60	1,19	6,54	9,66	12,43	1,02
1250	2300	0,125	57,09	0,63	11,42	1,19	6,53	9,69	12,46	1,00
1250	2200	0,129	57,25	0,62	11,23	1,20	6,53	9,72	12,48	0,97
1250	2100	0,133	57,42	0,61	11,04	1,21	6,53	9,75	12,51	0,95
1250	2000	0,136	57,58	0,59	10,85	1,21	6,52	9,79	12,53	0,93

Table A2- Simulation of a isothermal decompression melting process starting from a lherzolitic composition.

T (°C)	Pressure (bar)	F (melt fraction)	Solid composition								Solid phase percentage	
			SiO_2 (wt%)	TiO_2	Al_2O_3	Fe_2O_3	FeO	MgO	CaO	Na_2O	H2O	olivine	clinopyroxene
1230	4000	1,000	47,36	0,87	14,25	2,28	8,09	11,66	9,29	3,29	2,90	0	
1220	4000	0,991	47,42	0,88	14,38	2,29	8,09	11,34	9,37	3,32	2,93	0,85	
1210	4000	0,977	47,52	0,89	14,59	2,30	8,07	10,77	9,51	3,37	2,97	2,34	
1200	4000	0,963	47,62	0,90	14,81	2,32	8,05	10,23	9,64	3,42	3,01	3,75	
1190	4000	0,949	47,72	0,92	15,02	2,33	8,02	9,70	9,77	3,46	3,06	5,08	
1180	4000	0,937	47,83	0,93	15,22	2,34	7,98	9,20	9,90	3,51	3,10	6,35	
1170	4000	0,925	47,93	0,94	15,42	2,34	7,93	8,72	10,03	3,56	3,14	7,55	
1160	4000	0,913	48,03	0,95	15,61	2,35	7,87	8,26	10,15	3,60	3,18	8,70	
1150	4000	0,902	48,13	0,96	15,80	2,35	7,81	7,82	10,27	3,64	3,22	9,78	
1140	4000	0,892	48,23	0,98	15,98	2,35	7,73	7,40	10,38	3,69	3,25	10,82	
1130	4000	0,882	48,33	0,99	16,17	2,35	7,65	7,00	10,50	3,73	3,29	11,82	
1120	4000	0,872	48,43	1,00	16,34	2,35	7,56	6,62	10,61	3,77	3,33	12,77	
1110	4000	0,863	48,53	1,01	16,51	2,34	7,46	6,26	10,72	3,81	3,36	13,68	
1100	4000	0,855	48,63	1,02	16,68	2,33	7,35	5,91	10,83	3,85	3,40	14,55	0
1090	4000	0,835	48,70	1,01	16,96	2,32	7,30	5,62	10,68	3,93	3,48	15,00	1,52
1080	4000	0,801	48,77	0,95	17,40	2,31	7,32	5,38	10,19	4,08	3,62	14,93	5,01
1070	4000	0,769	48,87	0,89	17,82	2,29	7,30	5,13	9,70	4,22	3,78	14,93	8,23
1060	4000	0,738	49,00	0,82	18,24	2,26	7,26	4,89	9,23	4,37	3,93	14,97	11,21
1050	4000	0,710	49,15	0,75	18,65	2,23	7,20	4,66	8,77	4,51	4,08	15,06	13,93

Table A3- Simulation of a crystallizzation process. Starting composition is a melt from 1 % melting of a lherzolite.

T (°C)	Pressure (bar)	F (melt fraction)	Solid composition									Solid phase percentage	
			SiO_2 (wt%)	TiO_2	Al_2O_3	Fe_2O_3	FeO	MgO	CaO	Na_2O	H2O	olivine	clinopyroxene
1240	4000	1,000	47,11	0,89	13,76	2,30	8,25	12,18	9,88	2,72	2,91	0	
1230	4000	0,993	47,15	0,90	13,86	2,31	8,25	11,92	9,95	2,74	2,93	0,71	
1220	4000	0,977	47,25	0,91	14,09	2,32	8,24	11,33	10,11	2,78	2,98	2,28	
1210	4000	0,963	47,35	0,93	14,30	2,34	8,22	10,76	10,26	2,82	3,02	3,75	
1200	4000	0,949	47,45	0,94	14,51	2,35	8,20	10,21	10,40	2,86	3,07	5,15	
1190	4000	0,935	47,56	0,95	14,72	2,36	8,16	9,69	10,55	2,90	3,11	6,47	
1180	4000	0,923	47,66	0,97	14,92	2,37	8,12	9,19	10,69	2,94	3,15	7,73	
1170	4000	0,911	47,76	0,98	15,11	2,37	8,07	8,71	10,82	2,98	3,20	8,93	
1160	4000	0,899	47,86	0,99	15,31	2,38	8,00	8,25	10,95	3,02	3,24	10,06	
1150	4000	0,889	47,96	1,00	15,49	2,38	7,93	7,82	11,08	3,06	3,28	11,15	
1140	4000	0,878	48,06	1,02	15,68	2,38	7,85	7,40	11,21	3,09	3,31	12,18	
1130	4000	0,868	48,16	1,03	15,85	2,38	7,77	7,00	11,34	3,13	3,35	13,17	
1120	4000	0,859	48,26	1,04	16,03	2,37	7,67	6,62	11,46	3,16	3,39	14,12	
1110	4000	0,850	48,36	1,05	16,20	2,37	7,57	6,25	11,58	3,20	3,43	15,03	0,00
1100	4000	0,838	48,45	1,06	16,40	2,36	7,47	5,92	11,64	3,24	3,47	15,80	0,37
1090	4000	0,803	48,48	1,01	16,84	2,35	7,51	5,67	11,15	3,36	3,62	15,69	4,03
1080	4000	0,769	48,55	0,95	17,27	2,33	7,53	5,43	10,67	3,49	3,78	15,64	7,45
1070	4000	0,738	48,67	0,88	17,70	2,31	7,51	5,19	10,19	3,62	3,95	15,65	10,61
1060	4000	0,708	48,80	0,80	18,12	2,28	7,47	4,95	9,73	3,74	4,11	15,71	13,52
1050	4000	0,680	48,96	0,73	18,53	2,25	7,40	4,71	9,28	3,87	4,28	15,81	16,20

Table A4- Simulation of a crystallizzation process. Starting composition is a melt from 2 % melting of a lherzolite.

T (°C)	Pressure (bar)	F (melt fraction)	Solid composition									Solid phase percentage	
			SiO_2 (wt%)	TiO_2	Al_2O_3	Fe_2O_3	FeO	MgO	CaO	Na_2O	H2O	olivine	clinopyroxene
1250	4000	1,000	46,90	0,89	13,17	2,34	8,49	12,65	10,37	2,26	2,91	0	
1240	4000	0,996	46,93	0,90	13,23	2,35	8,49	12,49	10,41	2,27	2,92	0,44	
1230	4000	0,979	47,03	0,91	13,45	2,37	8,49	11,87	10,58	2,31	2,97	2,08	
1220	4000	0,964	47,14	0,93	13,67	2,39	8,48	11,28	10,75	2,35	3,02	3,63	
1210	4000	0,949	47,24	0,94	13,88	2,40	8,47	10,72	10,91	2,38	3,07	5,10	
1200	4000	0,935	47,34	0,95	14,09	2,41	8,44	10,17	11,07	2,42	3,11	6,49	
1190	4000	0,922	47,44	0,97	14,29	2,42	8,40	9,65	11,22	2,45	3,16	7,81	
1180	4000	0,909	47,54	0,98	14,49	2,43	8,35	9,15	11,37	2,49	3,20	9,06	
1170	4000	0,898	47,65	0,99	14,68	2,44	8,29	8,67	11,52	2,52	3,24	10,25	
1160	4000	0,886	47,75	1,01	14,87	2,44	8,23	8,22	11,66	2,55	3,28	11,39	
1150	4000	0,875	47,85	1,02	15,05	2,44	8,15	7,78	11,80	2,58	3,33	12,47	
1140	4000	0,865	47,95	1,03	15,23	2,44	8,07	7,36	11,94	2,61	3,36	13,50	
1130	4000	0,855	48,06	1,04	15,41	2,44	7,97	6,96	12,07	2,64	3,40	14,49	
1120	4000	0,846	48,16	1,06	15,58	2,43	7,87	6,58	12,21	2,67	3,44	15,44	
1110	4000	0,837	48,26	1,07	15,75	2,42	7,76	6,22	12,34	2,70	3,48	16,35	0
1100	4000	0,808	48,28	1,05	16,12	2,42	7,78	5,95	12,02	2,79	3,60	16,47	2,76
1090	4000	0,773	48,31	1,00	16,56	2,41	7,82	5,70	11,55	2,89	3,77	16,39	6,32
1080	4000	0,740	48,39	0,93	16,99	2,39	7,83	5,46	11,08	3,00	3,93	16,36	9,65
1070	4000	0,709	48,50	0,86	17,41	2,36	7,81	5,22	10,61	3,11	4,11	16,39	12,74
1060	4000	0,680	48,64	0,79	17,83	2,33	7,76	4,98	10,16	3,22	4,28	16,46	15,58
1050	4000	0,653	48,80	0,71	18,24	2,30	7,69	4,74	9,72	3,33	4,46	16,57	18,19

Table A5- Simulation of a crystallizzation process. Starting composition is a melt from 3 % melting of a lherzolite.

T (°C)	Pressure (bar)	F (melt fraction)	Solid composition								Solid phase percentage	
			SiO_2 (wt%)	TiO_2	Al_2O_3	Fe_2O_3	FeO	MgO	CaO	Na_2O	H2O	olivine	clinopyroxene
1260	4000	1,000	46,82	0,86	12,52	2,40	8,74	13,09	10,78	1,88	2,91		
1250	4000	0,999	46,82	0,86	12,53	2,40	8,74	13,06	10,79	1,88	2,91	0,10	
1240	4000	0,982	46,93	0,88	12,75	2,42	8,75	12,42	10,97	1,92	2,96	1,83	
1230	4000	0,965	47,03	0,89	12,97	2,44	8,75	11,80	11,15	1,95	3,01	3,46	
1220	4000	0,950	47,14	0,91	13,18	2,46	8,73	11,21	11,32	1,98	3,06	5,01	
1210	4000	0,935	47,24	0,92	13,39	2,47	8,71	10,65	11,50	2,01	3,11	6,47	
1200	4000	0,922	47,35	0,94	13,59	2,48	8,68	10,11	11,66	2,04	3,16	7,85	
1190	4000	0,908	47,45	0,95	13,78	2,49	8,64	9,58	11,83	2,07	3,20	9,16	
1180	4000	0,896	47,56	0,96	13,98	2,50	8,58	9,09	11,99	2,10	3,25	10,41	
1170	4000	0,884	47,66	0,98	14,16	2,51	8,52	8,61	12,14	2,13	3,29	11,60	
1160	4000	0,873	47,77	0,99	14,35	2,51	8,45	8,15	12,30	2,16	3,33	12,73	
1150	4000	0,862	47,87	1,00	14,53	2,51	8,37	7,72	12,45	2,18	3,38	13,81	
1140	4000	0,852	47,98	1,01	14,71	2,51	8,27	7,30	12,59	2,21	3,42	14,84	
1130	4000	0,842	48,09	1,03	14,88	2,50	8,17	6,90	12,74	2,24	3,46	15,83	
1120	4000	0,832	48,19	1,04	15,05	2,50	8,06	6,52	12,88	2,26	3,50	16,78	
1110	4000	0,813	48,24	1,04	15,32	2,49	8,02	6,20	12,80	2,31	3,58	17,30	1,41
1100	4000	0,778	48,23	1,01	15,75	2,48	8,08	5,96	12,35	2,40	3,74	17,17	5,05
1090	4000	0,744	48,26	0,96	16,18	2,47	8,12	5,71	11,89	2,49	3,91	17,11	8,48
1080	4000	0,712	48,34	0,90	16,61	2,45	8,13	5,47	11,44	2,59	4,09	17,11	11,69
1070	4000	0,682	48,45	0,83	17,03	2,42	8,10	5,23	10,99	2,68	4,27	17,15	14,68
1060	4000	0,654	48,59	0,76	17,45	2,39	8,05	4,99	10,54	2,78	4,45	17,23	17,44
1050	4000	0,627	48,75	0,69	17,86	2,35	7,97	4,75	10,11	2,87	4,64	17,34	19,99

Table A6- Simulation of a crystallizzation process. Starting composition is a melt from 4 % melting of a lherzolite.

T (°C)	Pressure (bar)	F (melt fraction)	Solid composition									Solid phase percentage	
			SiO_2 (wt%)	TiO_2	Al_2O_3	Fe_2O_3	FeO	MgO	CaO	Na_2O	H2O	olivine	clinopyroxene
1260	4000	1,000	46,81	0,81	11,81	2,46	8,97	13,55	11,10	1,57	2,91	0	
1250	4000	0,984	46,91	0,83	12,00	2,48	8,99	12,97	11,28	1,60	2,96	1,58	
1240	4000	0,967	47,01	0,84	12,21	2,50	8,99	12,33	11,47	1,62	3,01	3,30	
1230	4000	0,951	47,12	0,86	12,42	2,52	8,99	11,72	11,66	1,65	3,06	4,92	
1220	4000	0,936	47,23	0,87	12,63	2,53	8,97	11,13	11,84	1,68	3,11	6,45	
1210	4000	0,921	47,34	0,88	12,83	2,55	8,95	10,57	12,02	1,71	3,16	7,90	
1200	4000	0,907	47,45	0,90	13,02	2,56	8,91	10,02	12,20	1,73	3,21	9,28	
1190	4000	0,894	47,56	0,91	13,21	2,57	8,86	9,50	12,38	1,76	3,25	10,59	
1180	4000	0,882	47,67	0,92	13,40	2,57	8,80	9,01	12,55	1,78	3,30	11,83	
1170	4000	0,870	47,78	0,94	13,58	2,58	8,73	8,53	12,71	1,81	3,35	13,02	
1160	4000	0,859	47,89	0,95	13,76	2,58	8,65	8,07	12,88	1,83	3,39	14,15	
1150	4000	0,848	48,00	0,96	13,94	2,58	8,56	7,64	13,04	1,85	3,43	15,23	
1140	4000	0,837	48,12	0,97	14,11	2,58	8,46	7,22	13,19	1,88	3,47	16,27	
1130	4000	0,828	48,23	0,98	14,28	2,57	8,35	6,82	13,35	1,90	3,52	17,26	
1120	4000	0,818	48,34	1,00	14,44	2,56	8,23	6,44	13,50	1,92	3,56	18,21	0
1110	4000	0,782	48,28	0,98	14,88	2,56	8,32	6,20	13,06	2,00	3,72	18,04	3,75
1100	4000	0,748	48,27	0,95	15,30	2,55	8,38	5,95	12,62	2,08	3,89	17,95	7,23
1090	4000	0,716	48,31	0,91	15,73	2,54	8,41	5,71	12,19	2,16	4,06	17,92	10,52
1080	4000	0,685	48,38	0,85	16,15	2,51	8,41	5,46	11,75	2,24	4,25	17,93	13,60
1070	4000	0,656	48,49	0,79	16,56	2,48	8,39	5,22	11,31	2,32	4,44	17,98	16,48
1060	4000	0,628	48,63	0,73	16,98	2,45	8,33	4,98	10,88	2,40	4,63	18,07	19,15
1050	4000	0,602	48,78	0,66	17,39	2,41	8,24	4,74	10,46	2,48	4,83	18,19	21,62

Table A7- Simulation of a crystallizzation process. Starting composition is a melt from 5 % melting of a lherzolite.

T (°C)	Pressure (bar)	F (melt fraction)	Solid composition									Solid phase percentage	
			SiO_2 (wt%)	TiO_2	Al_2O_3	Fe_2O_3	FeO	MgO	CaO	Na_2O	H2O	olivine	clinopyroxene
1280	4000	1,000	47,08	0,66	10,18	2,56	9,38	14,51	11,61	1,11	2,91	0	
1270	4000	0,989	47,15	0,67	10,30	2,58	9,39	14,12	11,73	1,12	2,94	1,09	
1260	4000	0,970	47,28	0,68	10,50	2,61	9,41	13,43	11,95	1,14	3,00	3,00	
1250	4000	0,952	47,40	0,69	10,70	2,63	9,42	12,77	12,17	1,16	3,06	4,80	
1240	4000	0,935	47,53	0,71	10,89	2,65	9,42	12,13	12,39	1,18	3,11	6,49	
1230	4000	0,919	47,65	0,72	11,08	2,67	9,41	11,51	12,60	1,20	3,17	8,10	
1220	4000	0,904	47,77	0,73	11,27	2,68	9,38	10,92	12,80	1,22	3,22	9,61	
1210	4000	0,890	47,90	0,74	11,45	2,70	9,34	10,36	13,00	1,24	3,27	11,05	
1200	4000	0,876	48,03	0,75	11,63	2,71	9,29	9,82	13,20	1,26	3,32	12,42	
1190	4000	0,863	48,15	0,76	11,80	2,72	9,22	9,30	13,39	1,28	3,37	13,72	
1180	4000	0,851	48,28	0,78	11,98	2,72	9,15	8,80	13,58	1,30	3,42	14,96	
1170	4000	0,839	48,41	0,79	12,14	2,72	9,06	8,32	13,77	1,32	3,47	16,14	
1160	4000	0,827	48,53	0,80	12,31	2,72	8,96	7,87	13,95	1,34	3,52	17,27	
1150	4000	0,817	48,66	0,81	12,47	2,72	8,85	7,43	14,13	1,35	3,56	18,35	
1140	4000	0,806	48,79	0,82	12,63	2,71	8,73	7,02	14,31	1,37	3,61	19,39	0
1130	4000	0,783	48,81	0,83	12,92	2,71	8,73	6,69	14,20	1,41	3,72	19,80	1,90
1120	4000	0,750	48,74	0,82	13,33	2,71	8,82	6,42	13,81	1,46	3,88	19,71	5,36
1110	4000	0,717	48,71	0,81	13,73	2,70	8,88	6,17	13,42	1,52	4,06	19,65	8,66
1100	4000	0,686	48,71	0,79	14,13	2,69	8,92	5,91	13,02	1,58	4,24	19,63	11,79
1090	4000	0,656	48,75	0,76	14,54	2,67	8,94	5,66	12,62	1,64	4,43	19,64	14,75
1080	4000	0,628	48,82	0,72	14,94	2,64	8,92	5,41	12,22	1,70	4,63	19,69	17,54
1070	4000	0,601	48,93	0,67	15,34	2,61	8,87	5,17	11,81	1,76	4,84	19,77	20,15
1060	4000	0,576	49,06	0,62	15,74	2,57	8,80	4,93	11,41	1,83	5,06	19,88	22,59
1050	4000	0,552	49,21	0,57	16,14	2,52	8,69	4,69	11,01	1,89	5,27	20,01	24,86

Table A8- Simulation of a crystallizzation process. Starting composition is a melt from 10 % melting of a lherzolite.